Reconstruction of the Permafrost Extent in Western Europe during the Last Glacial Maximum based on Regional Climate Model Simulations

Master Thesis in Meteorology
by

Kim Helen Albers

November 2020

INSTITUTE FOR METEOROLOGY AND CLIMATE RESEARCH
KARLSRUHER INSTITUTE OF TECHNOLOGY (KIT)

Supervisor:	Prof. Dr. Joaquim Pinto
2nd Supervisor:	Dr. Aiko Voigt
Advisor:	Dr. Patrick Ludwig

Abstract

During the Last Glacial Maximum (LGM), a very cold and dry period around 26.5 to 19 thousand years ago, permafrost was widespread in Europe. Periglacial features such as pingos, ice-wedge pseudomorphs, and sand wedges are found in Europe and serve as a proof for the occurence of permafrost at that time. These are thus seen as a proxy for permafrost. In global climate model simulations, the permaforst distribution during the LGM is poorly represented. In this work the potential of regional climate model simulations to improve the reconstruction of the permafrost distribution in Western Europe during the LGM is evaluated. For the first time, criteria for possible thermal contraction cracking of the ground are applied to the climate model data. These criteria were derived from fieldwork and serve as a precondition for the development of proxies of permafrost. Simulations with prevailing westerly winds transporting heat and moisture from the North Atlantic are not able to represent the permafrost and ground cracking distribution in Europe during the LGM. With a large-scale circulation that promotes easterly winds, a colder version of the LGM is realized. Whereas the permafrost extent and ground cracking regions in the global climate model simulation still deviate from proxy evidence, they agree in the regional counterpart. With an appropriate forcing, an added value of the regional climate model simulation to the global climate model simulation can thus be achieved. Furthermore, the model data support that the proxies indicate rather seasonal frozen ground than continuous permafrost in France.

Kurzfassung

Während des Letzten Glazialen Maximums (LGM), einer sehr kalten und trockenen Zeitperiode vor etwa 26.5 bis 19 tausend Jahren, war Permafrost weit verbreitet. Dies lässt sich anhand von periglazialen Relikten, wie z.B. Pingos, Eis- und Sandkeilen, ableiten. Sie werden daher als Proxies für Permafrost angesehen. Globale Klimamodellsimulationen repräsentieren die Permafrostverteilung während des LGMs nur unzureichend. In der vorliegenden Arbeit wird untersucht, inwieweit die Rekonstruktion der Permafrostverteilung mit Hilfe regionaler Klimamodellsimulationen optimiert werden kann. Erstmalig werden hierbei Klimamodelldaten auf Kriterien für mögliche Rissbildung im Boden durch thermische Kontraktion, welche in Feldstudien deduziert wurden, untersucht. Die dargelegten Kriterien für die Rissbildung im Boden stellen eine Vorbedingung für Entstehung der genannten Proxies für Permafrost dar. In Simulationen des LGMs mit vorherrschenden Westwinden, welche Wärme und Feuchte vom Nordatlantik nach Europa transportieren, wird weder die korrekte Permafrostverteilung, noch die Ausdehnung der Gebiete, in denen ein Aufreißen des Bodens theoretisch möglich ist, korrekt wiedergegeben. Mit einer großskaligen Zirkulation, die eine Anströmung von Osten begünstigt, können die Ergebnisse der globalen Klimasimulationen leicht verbessert werden. Erst die entsprechend angetriebenen regionalen Klimamodellsimulationen stimmen mit den proxybasierten Verteilungen überein. Die Modelldaten bestätigen daher, dass die Proxies eher auf saisonalen Bodenfrost und nicht auf kontinuierlichen Permafrost in Frankreich hindeuten.

Contents

1 Introduction

Up to one fifth of the Northern Hemisphere's land surface is underlain by perennially frozen ground that is thus classified as permafrost. In the Southern Hemisphere, permafrost underlies an area that is three magnitudes smaller (Intergovernmental Panel on Climate Change (IPCC) 2019). Permafrost is a major element of the Earth's cryosphere (Harris et al. 2009). The formal definition of permafrost is: "ground that remains at or below 0 °C for at least two consecutive years" (van Everdingen 2005). The distribution not only of permafrost but of all components of the cryosphere is depicted in Fig. 1.1 for the Northern Hemisphere, with data from 2012. Permafrost is separated in continuous and discontinuous permafrost. Differences between these two

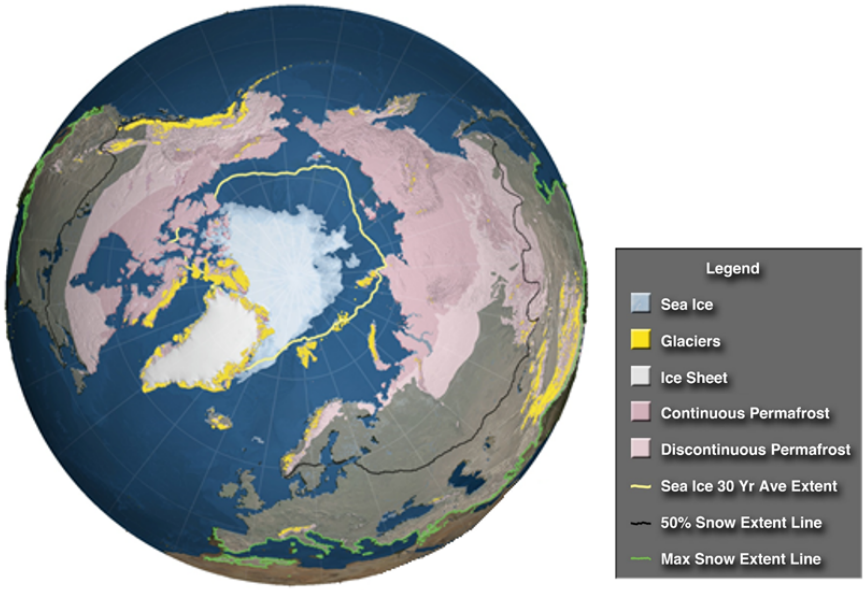

Figure 1.1: The cryosphere of the Northern Hemisphere: Shaded areas indicate the minimum summer sea ice extent in 2012 (light blue), the location of the glaciers (yellow) and the Greeland Ice Sheet (white), and the permafrost distribution (continuous permafrost: dark pink; discontinuous permafrost: light pink). The yellow line marks the 30-year average extent for yearly sea ice minima from 1979 to 2012. The black and green lines farther south represent the 50 % snow extent and the maximum snow extent, respectively (adapted after IPCC 2013; Fig. 4.1).

forms of permafrost will be addressed in Chap. 2. The spatial dominance of permafrost becomes obvious from Fig. 1.1.

Permafrost soils influence the surface energy balance, the hydrological cycle, the vegetation cover and, most importantly, they serve as a carbon reservoir (c.f. Liu and Jiang 2016b; Vandenberghe et al. 2014). Through peat development or dust deposition, for example, organic carbon is accumulated in the frozen ground over thousands of years and can be trapped over times of several years to millenia (c.f. Liu and Jiang 2016b; Schuur et al. 2015). Permafrost currently contains the

largest amounts of organic carbon in global terrestrial systems and twice as much as the atmosphere (c.f. United Nations Environment Programme (UNEP) 2019 and references therein). Yet, this reservoir is climate sensitive (Harris et al. 2009; IPCC 2013; IPCC 2019). As long as ground temperatures remain constantly far below 0 °C and the permafrost is therefore stable, the carbon is permanently stored. Developments of recent years, however, already show a rapid permafrost degradation, that is in conformity with the temperature raise of climate change (c.f. e.g. IPCC 2013; Liu and Jiang 2016b; Vandenberghe et al. 2014) Permafrost soils become warmer until they reach the 0 °C mark and then start to thaw. The southern limit of permafrost is observed to shift northwards (c.f. Osterkamp and Burn 2003). This shift is quantified to 30 to 80 km in the last decades, which is associated with a large reduction of the permafrost areas, yielding vast consequences for the environment and the climate (UNEP 2019).

While permafrost thaws, decomposition of organic carbon by soil microbes is initialised (Liu and Jiang 2016b). Gaseous carbon dioxide (CO_2) and methane (CH_4) is formed and then released into the atmosphere. These are potent greenhouse gases (c.f. e.g. Liu and Jiang 2016b; Osterkamp and Burn 2003). The United Nations Environment Programme (UNEP) states the thaw of permafrost to be "one of the most important 'tipping elements' that could release significant amounts of methane [...] into the environment" (UNEP 2019). The emission of CO_2 and CH_4 intensifies the greenhouse effect, leading to stronger reflections of longwave radiation back to the Earth and accelerates thereby the climate change (Liu and Jiang 2016b; Schuur et al. 2015; IPCC 2019). In that way, permafrost thaw is part of a positive feedback mechanism induced by global warming (Vandenberghe et al. 2014; IPCC 2019). Because of this feedback process, permafrost will likely be important for the response of the climate system to global changes (c.f. Levavasseur et al. 2011). Climate and Earth System Models have been developed to simulate the behaviour of the Earth's climate and to understand the complex interactions between its different components. With increased computational capacity, the models became more sophisticated and it was possible to incorporate more and more processes explicitely (IPCC 2013). This improvement is ongoing. Several of these models implemented global permafrost carbon dynamics (Schuur et al. 2015). Future projections indicate a widespread disappearance of permafrost by the end of this century

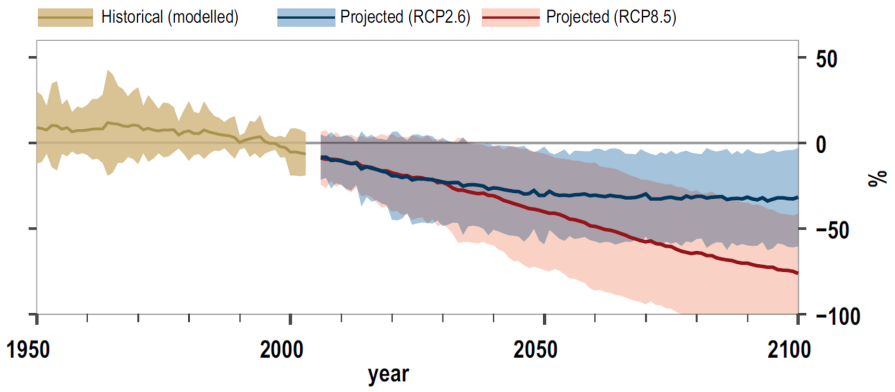

Figure 1.2: Modelled near-surface permafrost area in percent compared against the mean of the reference period 1979 to 2005. The modelled historical changes are indicated in brown. In blue and red, the projected future changes under low (RCP2.6, blue) and high (RCP8.5, red) greenhouse gas emission scenarios are depicted. The lines represent the ensemble mean, shaded areas the very likely range, i.e. 5-95 % model range (adapted after IPCC 2019; Fig. 1.5 l).

with very high confidence (IPCC 2019). Fig. 1.2 shows the near-surface (within 3-4 m) permafrost area of the Northern Hemisphere relative to the mean area of 1986 to 2005 over time, starting from 1950. According to the projections, the near-surface permafrost will retreat by 24 $\pm$ 16 % in RCP2.6 and by 69 $\pm$ 20 % in RCP8.5 (both the likely range) until the end of the century. This is associated with a release of carbon on the order of ten to 100 billion tons (Gt C) and will thus potentially accelerate climate change. Although methane will be significantly less emitted, it might contribute 40-70 % of the total radiative forcing exerted concomitant to permafrost thaw (c.f. IPCC 2019; Schuur et al. 2015). The large ranges of estimates for both degraded permafrost area and associated greenhouse gas emissions illustrate the related uncertainty of these projections that go in line with a high variability in the resulting climate warming. Schuur et al. (2015) conclude that "the magnitude and timing of greenhouse gas emissions [...] and their impact on climate change remain uncertain".

Constraints of the projections remain not only due to a lack of knowledge and the internal variability of the climate system, but also because of model uncertainty. Models that are well tested under present-day conditions, simulate very different responses to the same forcing scenarios of the current century. Apparently, is it not sufficient to evaluate the climate models exclusively with respect to today's observations, since the latter only provide a small range of climate variability and the evaluations remain within the calibration range of the parametrizations (c.f Braconnot et al. 2012; Cleator et al. 2020). Hence, reconstructions from paleoclimate archives can be used to broaden this range and to get a robust assessment for the model's capability of simulating climate changes (c.f. Cleator et al. 2020; IPCC 2013). Besides ice cores and tree rings as common natural climate archives, numerous other features provide evidence on past climatic states (c.f. IPCC 2013; Ludwig et al. 2019). To understand the sensitivity of permafrost to (future) climate change, it is therefore essential to study the behaviour of the permafrost extent under different climatic conditions in the past (c.f. Saito et al. 2013; UNEP 2019; Vandenberghe et al. 2014).

Since permafrost was widespread in colder periods, it is logical to focus on the Last Glacial Maximum (LGM) in this study. The LGM is the "most recent interval when global ice sheets reached their maximum integrated ice volume during the last glaciation"(Mix et al. 2001) and occurred from around 26.5 to 19 thousand years before present (ka BP) (Clark et al. 2009). This period is particularly interesting, because the boundary conditions were vastly different than today (c.f. Kageyama et al. 2020). Large parts of the Northern Hemisphere were covered by ice sheets and greenhouse gas concentrations in the atmosphere were at a historical minimum, resulting in surface air temperatures of around 4 °C colder than today in annual and global mean. In the tropics, differences were smaller (< 3 °C), while they were largest near the Northern Hemispheric ice sheets (> 8 °C, both in annual mean). In Central Europe, they even amount to 14 °C (c.f. Annan and Hargreaves 2013; Bartlein et al. 2011; Clark et al. 2009).

Several climate model studies for the LGM revealed the general capability of global climate models to simulate a reasonable LGM climate (c.f. Harrison et al. 2015; Levavasseur et al. 2011; Ludwig et al. 2016; Saito et al. 2013). Due to their relatively coarse resolution, however, the magnitude of regional scale changes may not be displayed correctly (Harrison et al. 2015; Ludwig et al. 2016). Saito et al. (2013) investigated the permafrost extent in the LGM experiments of the Paleoclimate Modelling Intercomparison Project (PMIP) - Project Phase 2 and 3. The simulations conducted within PMIP2 showed "mixed results"(Saito et al. 2013) in comparison with

evidence from the fields, but improvement was found for the recent phase. Nevertheless, there is a large range of modelled permafrost distributions under LGM conditions (Vandenberghe et al. 2014) and some studies have to conclude that the used model fail to reproduce the permafrost distribution over Central and Western Europe during the LGM (c.f. Kitover et al. 2013; Kitover et al. 2016; Levavasseur et al. 2011; Ludwig et al. 2017). The differences between the modelled permafrost distribution and proxy-based reconstructions are partly attributed to the coarse horizontal resolution of the global climate models (c.f. Kitover et al. 2016; Ludwig et al. 2017; Saito et al. 2013). These inaccuracies are also found for other climate variables, such as temperature and precipitation, where the sign of the large-scale climate changes are correctly reproduced, but not the regional patterns nor the magnitude of changes (c.f. e.g. Cleator et al. 2020; Ludwig et al. 2019). Therefore, Ludwig et al. (2019) point out, that "regional climate modeling bridges the gap between the coarse resolution of current climate models and the regional-to-local scales, where the impact of climate changes are of primary interest".

Regional Climate Models (RCMs) are based on the approach of dynamical downscaling. For a subdomain of a global climate model simulation, they use this coarse data as initial and boundary conditions and increase then the horizontal and vertical resolution by explicitely resolving the physical processes relevant on regional scales (c.f. Ludwig et al. 2017; Ludwig et al. 2019). This model type is often used for present-day and future climate analyses while paleoclimate and especially LGM applications are limited (Ludwig et al. 2019). However, it was shown that RCMs can add value to the global climate simulations and thus worth the additional computational costs in many cases (c.f. Ludwig et al. 2019 and references therein). Regional climate modeling in the context of the LGM can improve the distribution of not only temperature and precipitation, but also of permafrost (Ludwig et al. 2017; Ludwig et al. 2019). The present study aims to analyse this further and in more detail.

The overall goal of this thesis is to reconstruct the permafrost distribution in Western Europe during the LGM based on regional climate model simulations. A range of southern boundaries for the permafrost extent will be defined and compared against the proxy-based distribution.

Therefore, literature research on the boundary conditions of the LGM and the resulting climate will be conducted as a first step as well as on permafrost. The definition of permafrost will be put into context and the proxies for past permafrost will be investigated. As a second step, the LGM permafrost distribution in Europe based on these proxies will be derived. After this, methods to extract permafrost occurence from climate model data will be addressed. The literature research will be presented in Chap. 2. The subsequent Chap. 3 introduces the climate models used for this study. These are the global climate models MPI-ESM-P and ECHAM6-FESOM. Both are used to drive the regional climate model simulations that are conducted with the Weather Resarch and Forecast (WRF) model. The main part of this thesis will focus on the presentation of the results (c.f. Chap. 4). It starts with the analysis of the climate of the global driving simulations in Europe and the North Atlantic. Afterwards, the climatic mean state as simulated with the WRF model will be investigated and then the permafrost extent of these simulations will be explored. The last part includes the application of different methods presented in the following chapters and the comparison against the proxy-based permafrost distribution. The results will be discussed in Chap. 5. A conclusion and summary (c.f. Chap. 6) will complete the thesis.

2 Theoretical Background

The theoretical background of this study will be addressed in this chapter. It consists of two parts. First, the LGM will be introduced. Timing and boundary conditions of the LGM will be discussed including the resulting climate.
In the second part, permafrost will be explored. Its definition and structure will be presented, as well as methods to identify locations with former existence of permafrost. At last, both topics will be brought together discussing the permafrost distribution during the LGM.

2.1 The Last Glacial Maximum

During the last three million years, the Earth's climate underwent several substantial reorganisations. The climate altered from warm to cold, and from arid to humid conditions with a mutual interaction of all components of the Earth, namely the atmosphere, lithosphere, hydrosphere, biosphere, and cryosphere (c.f. Kohfeld and Harrison 2000; Löfverström et al. 2014).
Fig. 2.1 shows the evolution of important external forcings for these variations for the last 800 thousand years with present at zero ka. On the one hand, these are the orbital parameters with the Eccentricity, Obliquity, and Precession that are summarized in the Milanković cycles. They describe how the Earth moves in space and have thus implications for the incoming solar radiation and the energy budget on Earth. Eccentricity values near zero represent a circle-like orbit around the Sun. Higher values imply a more elliptically shaped orbit. Obliquity describes the axial tilt

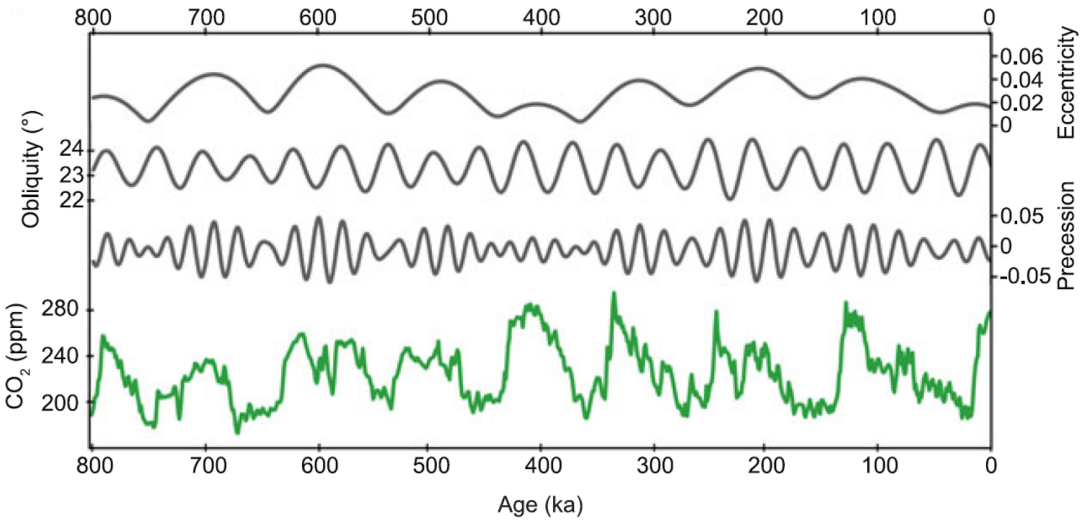

Figure 2.1: Orbital parameters and atmospheric CO_2 concentration from Antarctic ice cores over the past 800 thousand years (Ludwig et al. 2019; Fig. 4 a).

of the Earth and Precession means the rotation of this axis (Berger 1978). On the other hand, greenhouse gases play a crucial role in the climate system. In Fig. 2.1, the CO_2 concentration from Antarctic ice cores are depicted.

The most recent glacial cycle began at the same time as the Palaeolithic Age and right after the Last Interglacial at around 115 ka BP. The Last Interglacial was a warmer period that corresponds to high CO_2 concentrations and to a relative sea level highstand (Kukla et al. 2002). This stands in contrast to the period that will be investigated further in this thesis. The LGM is noticeable in the figure by the low CO_2 values at about 20 ka BP. It is defined as the "most recent interval when global ice sheets reached their maximum integrated ice volume during the last glaciation" (Mix et al. 2001) and can thus be detected through for example a relative sea level lowstand. It was found that the sea level was 127.5 to 135 m lower during the LGM than today (c.f. Clark et al. 2009). Not all of the ice sheets that covered the Earth during this period reached their maximum at the same time. Therefore, the timing of the globally defined LGM does not agree certainly with the local LGM (c.f. Hughes et al. 2013). However, for the Laurentide Ice Sheet (LIS) in North America and for the Fennoscandian Ice Sheet (FIS) that covered large parts of Europe, this is the case. This suggests the near-equilibrium of these ice sheets with the climate during the LGM that is dated from 26.5 to 19 ka BP (c.f. Clark et al. 2009).

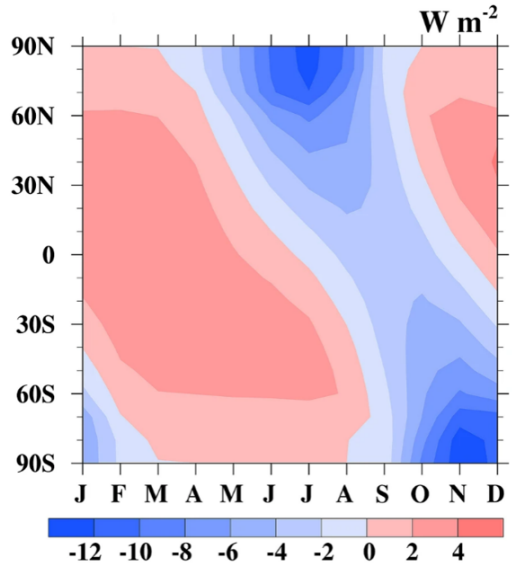

Figure 2.2: Differences of incoming solar radiation at the top of the atmosphere between LGM and PI conditions for each month of the year (Cao et al. 2019; Fig. 5 a).

The LGM is characterised by glacial boundary conditions and orbital parameters and thus solar insolation that is similar to today. Nonetheless, it is assumed that changes in the insolation provoked the first growth of the ice sheets. The summer energy was decreasing while the winter energy was increasing (c.f. Fig. 2.2). The differences were not very large, but changed the seasonal cycle (c.f. Cao et al. 2019). The huge ice sheets that covered large parts of the Northern Hemisphere were an important boundary condition, since their high albedo lead to increasing reflection and affected the radiation budget thereby. Additionally, the ice sheets modified the orography and influenced the large-scale atmospheric circulation. Since more H_2O was bound in the ice sheets, the sea level

was lowered consequently. That, in turn, affected the land-sea configuration as more land was exposed to the atmosphere. For example, France and Great Britain were connected at that time. Both sea surface temperatures (SSTs) and deep ocean temperatures were lower (c.f. Clark et al. 2009), which lead to less evaporation from the ocean and to an increased concentration of atmospheric gases in the oceans, since their solubility increases with decreasing temperatures. Most of the relevant greenhouse gases were at a historic minimum with less than half of today's atmospheric concentrations (c.f. Annan and Hargreaves 2013; Bartlein et al. 2011; Monnin et al. 2001 and Fig. 2.1). Tab. 3.1 in Chap. 3 gives an overview of the different values. Firstly, the low concentration of carbon dioxide influences the global surface temperature. The greenhouse gas effect is reduced in a way that it is consistent with a net radiative forcing decrease of 2.8 W/m² (c.f. Cao et al. 2019). Secondly, it has an impact on the vegetation distribution, which can in turn be seen as another boundary condition for the climate of the LGM. Growth of C4 plants was favoured over C3 plants, because photosynthesis of the latter is more sensitive to the CO_2 concentration in the atmosphere (c.f. Prentice and Harrison 2009). In the non-glaciated regions of Northern Europe, this lead to steppe and tundra vegetation such as open shrublands and grassland and in Southern Europe, semidesert steppe and steppe with embedded forests dominated the landscape (Florineth and Schlüchter 2000; Pinto and Ludwig 2020). The terrestrial ecosystems were less productive (Bartlein et al. 2011) and there was more open vegetation that resulted in easily erodible soils (Prospero et al. 2002; Ray and Adams 2001).

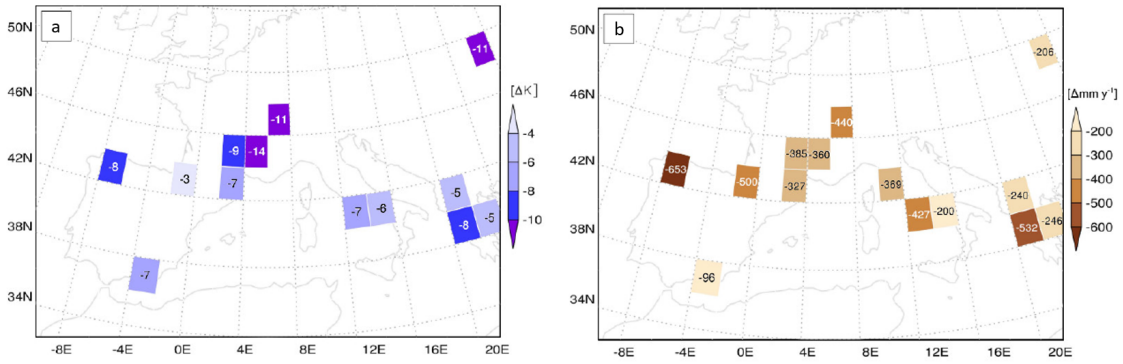

Figure 2.3: Pollen-based reconstruction of changes of temperature *(a)* and precipitation *(b)* for the LGM and present-day conditions (Ludwig et al. 2017; Fig. 4 a and c).

All these boundary conditions and forcings lead to a climate on Earth that was substantially different from today. In general, it was colder and drier during the LGM. In global and annual mean, Annan and Hargreaves (2013) found a cooling of $4.0 \pm 0.8\,°C$ for the surface air temperature. In Fig. 2.3, European temperature and precipitation differences for LGM minus PI conditions based on proxy data (Bartlein et al. 2011) are depicted. The differences in Europe are greater than in global mean with a 14 °C cooling in Central Europe. Additionally, the meridional temperature gradient was greater during the LGM. This is in agreement with polar amplified cooling because of the ice sheets in the north (c.f. Löfverström et al. 2014). Due to the glacial conditions, the hydrological cycle was weakened, leading to less precipitable water in the atmosphere and hence decreased precipitation by 200 to more than 600 mm/year in Europe (c.f. Bartlein et al. 2011; Pfahl et al. 2015 and Fig. 2.3). According to simulations by Löfverström et al. (2014), winter

precipitation does not reach far inland over Eurasia. Reasons were more extensive sea-ice cover in the North Atlantic as well as the altered land-sea configuration. They constrain the evaporation in addition to the effect of the reduced temperatures and result in drier air masses that move to Europe.
Mid-latitude cyclones transport heat, moisture and momentum from the tropics to the poles. Precipitation occurs along their fronts, especially in winter (c.f. Laîné et al. 2009). Therefore, changes in position and intensity of the storm track influence the precipitation patterns in Europe (c.f. Wang et al. 2018). However, with enhanced wind speeds and more intense cyclones, the above described effects are dominating and the precipitation during the LGM remains reduced.
In consequence of the glacial boundary conditions, the atmospheric circulation varied considerably from present-day conditions. Justino and Peltier (2005) showed that the direct influence of the altered topography with the ice sheets is more important for the atmospheric circulation in winter than any other forcing, such as albedo, greenhouse gases, or orbital forcing. A cold high developed in northeastern Europe as well as in North America over the respective ice shields (c.f. Cao et al. 2019; Justino et al. 2006; Ludwig et al. 2016). The LIS had an estimated height of 3000 to 4500 meter during the LGM (Ullman et al. 2014) and thus acted as a massive mechanical forcing (Löfverström et al. 2016). A planetary wave much larger than today was induced, with a deep trough downstream of the LIS. This lead to a zonalisation of the Atlantic jet stream (c.f. Löfverström et al. 2014). Apart from this altered structure, the jet was enhanced and its position was shifted southward (c.f. Li and Battisti 2008; Merz et al. 2015; Pausata et al. 2011). These changes are also associated with the presence of the LIS. Simulations show that the jet becomes narrower, stronger and more zonal with increasing simulated the LIS height (c.f. Löfverström et al. 2016). Merz et al. (2015) declare the eddy-driven jet as “the most dominant zonal feature in the North Atlantic domain under glaical conditions”. Its core wind speed exceeded 50 m/s. The storm track during the LGM evolved accordingly. In winter, it also was zonally orientated and the related cyclones were more intense. (c.f. Löfverström et al. 2014; Ludwig et al. 2016; Pinto and Ludwig 2020).

2.2 Permafrost and Reconstruction Methods

Based on the permafrost definition, the following section focuses first on the vertical and horizontal structure of permafrost and its corresponding climatic implications and geomorphical features. Since the latter can serve as a proxy for the identification of former permafrost, their development and prerequisites are presented as well as some caveats that should be considered. Subsequently, the permafrost distribution during the LGM in Europe is derived based on these proxies. Finally, some methods to infer permafrost existence from climate model data are introduced.
Permafrost is defined as “Ground (soil or rock and included ice and organic material) that remains at or below 0 °C for at least two consecutive years”(van Everdingen 2005). The definition is solely based on temperature and permafrost is therefore synonymous with perennially cryotic ground. Other than implied by the name, water within permafrost is not necessarily frozen. Due to high pressure and minerals, the freezing point of water may be depressed. Equally, according to its definition, permafrost does not have to be permanent, two consecutive years with ground temperatures at or below 0 °C are sufficient to classify ground as permafrost (c.f. van Everdingen 2005).

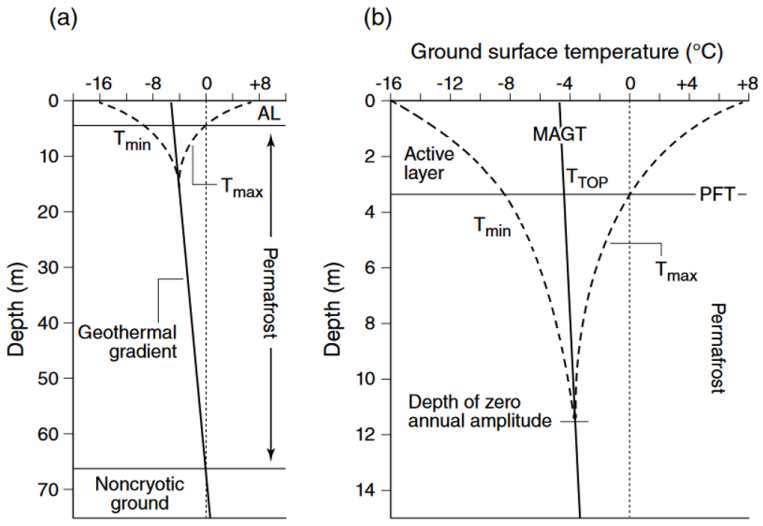

Figure 2.4: Simplified vertical profile of ground temperatures in a permafrost regime. *(a)* shows the full profile and *(b)* displays the upper part of the profile. The abbreviations are as follows: AL for active layer, T_{min}, and T_{max} for minimum and maximum annual temperature, MAGT for mean annual ground temperature, and T_{TOP} for mean temperature of the permafrost table (adapted after Ballantyne 2017; Fig. 4.5).

The vertical structure of permafrost ground can be derived from the vertical profile of the ground temperature. The schematics of a typical profile is depicted in Fig. 2.4. The mean annual ground temperature (MAGT) changes with depth according to a geothermal gradient. The point where the MAGT crosses the 0 °C limit and the ground becomes noncryotic marks the lower boundary of permafrost, which is called the permafrost base.

At these depths, the ground does not experience seasonal variations. The influence of the atmosphere and the surface only reaches to the depth of zero annual amplitude, above which the minimum and maximum annual temperature (T_{min}, and T_{max}, respectively; dashed lines in Fig. 2.4) diverge from each other. Above the depth, where the maximum annual temperature profile crosses 0 °C, the ground freezes and thaws seasonally. From the surface to this depth, the layer is termed the active layer. The thickness of the active layer can vary from a few centimeters to several meters (c.f. e.g. Osterkamp and Burn 2003). The boundary between the active layer and the permafrost layer is named permafrost table (c.f. Ballantyne 2017; van Everdingen 2005).

There is no distinct border between the occurence and absence of permafrost, but rather a gradual transition. The ground can be classified into four zones depending on the amount of actual permafrost (c.f. Ballantyne 2017, Fig. 2.5): continuous permafrost, when more then 90% of the surface is underlain by permafrost, widespread discontinuous permafrost for 50-90% (often abbreviated as discontinuous permafrost), sporadic discontinuous permafrost for 10-50% (often abbreviated as sporadic permafrost) and isolated patches, when less than 10% of the surface is underlain by permafrost (not depicted in Fig. 2.5. However, when the surface layer freezes and thaws seasonally similarly to the active layer, but has no permafrost layer underneath, it is only called seasonal ground freezing (c.f. Ballantyne 2017).

In general, the distribution and thickness of permafrost varies with latitude and altitude. Usually the active layer is relatively thin and permafrost is prevalent in cold climates. As the climatic conditions become less suitable, the active layer becomes thicker and the permafrost more sporadic

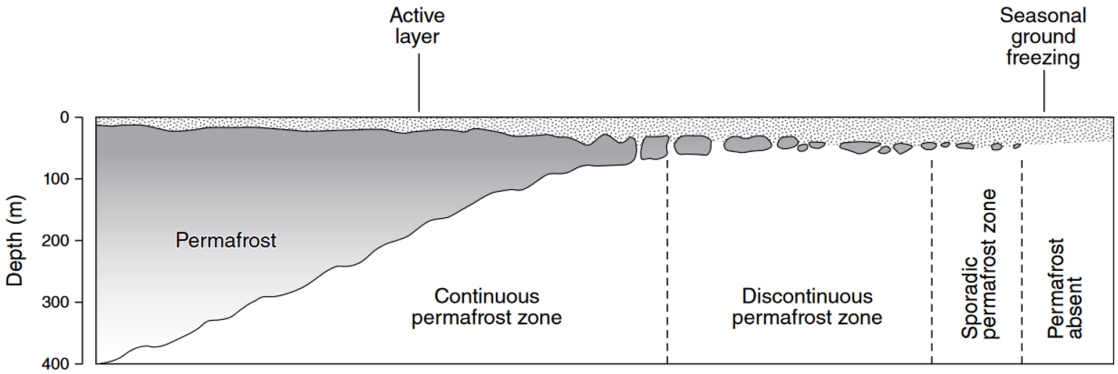

Figure 2.5: Schemtaic horizontal distribution of permafrost occurence and thickness (Ballantyne 2017; Fig. 4.9).

(c.f. Ballantyne 2017; Osterkamp and Burn 2003; Huissteden 2020). Nevertheless, it is not only the climate and temperature regime that determines the permafrost occurence and active layer thickness, but also surface conditions, such as vegetation cover, topography, winter snow cover and soil properties including the soil water content (c.f. Huissteden 2020). For example, snow can act as an isolating layer, buffering the ground from cold winter temperatures and in summer, vegetation can lead to shading (c.f. Osterkamp and Burn 2003).
Permafrost may develop where the MAGT is below 0 °C, so that the energy budet at the surface is negative. Seasonal frost may develop and resist summer thaw, so it can propagate downwards. This permafrost aggradation can continue until the permafrost is in equilibrium with both surface ground temperature and geothermal heat flux (c.f. Ballantyne 2017).
In terms of thermal regime, permafrost can be classified additionally. Equilibrium permafrost is in equilibrium with the present surface temperature and geothermal heat flux. Relict permafrost formed under colder conditions than today and can exist both in areas of today existing permafrost as well as in areas where the ground temperature today would be too high for permafrost formation. And past permafrost is ground with evidences for former permafrost, even though it is completely absent today (French 2008; French and Shur 2010). This work will focus on past permafrost.

Permafrost influences the surrounding environment not only when releasing greenhouse gases while thawing (c.f. Chap. 1). On the one hand, permafrost is able to limit water movement and groundwater storage to the active layer, especially, when the permafrost contains ice. This leads to a generally high moisture content in the active layer during summer (Ballantyne 2017). On the other hand, geomorphic features unique to permafrost areas may develop. Here, only a few of the many different features can be introduced. Most of them, the cryoturbations, have in common that they form under the influence of freezing and thawing processes, which cause deformations of the soil layers (c.f. Harris et al. 2018). Osterkamp and Burn (2003) name three principal geomorphic features that are important in permafrost terrain. First pingos, that are hills containing massive ice in their core (van Everdingen 2005) and polygons on the one side. Pingos develop when a body of unfrozen ground within permafrost (a talik) contains water that freezes from the top downwards. This freezing leads to an expansion and thus increases the pressure on the underlying water. Because the subjacent permafrost is impermeable, the ice is lifted and a mound on the surface can be

formed (c.f. Osterkamp and Burn 2003; van Everdingen 2005). Polygons are networks of troughs and ridges that are often orthogonal in plan and range from five to fifty meters in diameter. Under the troughs, wedge-shaped structures can be found, that consist of ice or sedimenents or both (Ballantyne 2017). They will be described later in detail. These two features both are associated with permafrost aggradation. While thawing of the permafrost, thermokarst terrain develops on the other side. It consists for example of lakes that form when ice in the permafrost melts, or of mounds that develop from former polygons (Osterkamp and Burn 2003; van Everdingen 2005).
Since these geomorphic features are associated with permafrost, they can act as proxies to identify past permafrost(e.g. Vandenberghe et al. 2014; Harris et al. 2018). In the following section, the focus will lie on the networks of wedge-shaped structures. These structures are named ice wedge, sand wedge, or composite wedge, depending on the infill of the wedges. Ice-wedge pseudomorphs are former ice wedges, where ice have been replaced with sediments after melting.
The basis of the wedge development is the thermal contraction cracking of the ground. When air temperatures are very low in winter, the ground cools from the surface downwards and contracts. This contraction is restricted, even stronger in (both sesaonally and perennially) frozen ground. In this case, the tensile stress exerted because of the thermal contraction depends mainly on the rate and magnitude of ground cooling. A slow cooling can be compensated through creeping of the soil (Ballantyne 2017). However, when the tensile stress exceeds the tensile strength of the ground, a thermal contraction crack evolve (c.f. Wolfe et al. 2018 and references therein). The maximum cooling zone is assumed to be the zone of maximum thermal-contraction. As the cooling propagates from the surface downwards, this zone is usually located in the near-surface layers (c.f. Fortier and Allard 2005). Nonetheless, thermal contraction cracking can also propagate upwards: When there is already a weak point in the ground, possibly as a result of a preceding crack, the tensile strength is reduced in the deeper ground and can be overcome more easily (Lachenbruch 1962; Matsuoka et al. 2018).
There is much ongoing research aiming for conditions and thresholds under which thermal contraction cracking is possible to occur (c.f. e.g. Matsuoka et al. 2018; Wolfe et al. 2018). The ground cooling rate is accepted to be an important factor (Fortier and Allard 2005; Lachenbruch 1962; Wolfe et al. 2018) and it was found that the mean annual air temperature (MAAT) should be close to $0\,^{\circ}$C (c.f. Bertran et al. 2014 and references therein). The occurence of thermal contraction cracking is more likely in cold regions with minimum snow cover, because of the isolating effect of snow that can reduce the cooling (Matsuoka et al. 2018). Usually threshold values are derived from observations of active sites over several years. Kokelj et al. (2014) determined a maximum ground surface temperature of $-15\,^{\circ}$C together with a five-day average cooling rate of $0.5\,^{\circ}$C/day prior to the cracking. Others measured the temperature at the top of permafrost or at 1 m depth and the thermal gradient in the active layer (i.e. the temperature difference between surface layer and at 1 meter depth) and derived thresholds for shallow cracking ($T_{100} < -5\,^{\circ}$C, and $\Delta T < -7\,^{\circ}$C/m) and for intensive deep cracking ($T_{100} < -10\,^{\circ}$C, and $\Delta T < -10\,^{\circ}$C/m) (Matsuoka et al. 2018). Values for these variables differ slightly at different sites, which might reflect varying soil compositions (c.f. e.g. Ballantyne 2017; Fortier and Allard 2005; Matsuoka et al. 2018; Murton 2007; Watanabe et al. 2013; Wolfe et al. 2018). In very cold conditions, these thresholds may be met in nearly every winter, so that thermal contraction cracking is equally common (c.f. Matsuoka et al. 2018). Under these conditions, ice or sand wedges may develop. The development

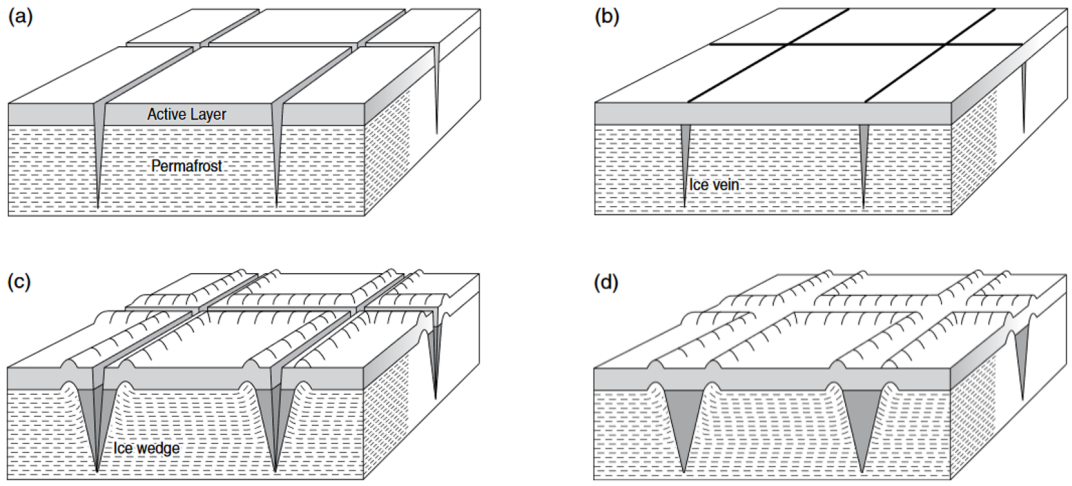

Figure 2.6: Schematic of the different steps of ice wedge development. See text for explanations of the different steps (Figure after Ballantyne 2017; Fig. 6.3).

of ice wedges and the related polygon is schematically depicted in Fig. 2.6. Starting point of the development for both ice and sand wedges is the thermal contraction cracking within permafrost during winter. An open crack may be filled with water in spring supplied from melting snow. In autumn or winter the water freezes building an ice vein (c.f. Fig. 2.6 b). If this process is repeated over many (not necessarily consecutive) years, adjacent ice veins may merge and the cracks widen and deepen. This leads to the typical shape of a wedge. The melting and refreezing of ice in the wedge cause ridges along their edges, because water increases its volume by 9% becoming ice and the soil expands correspondingly (c.f. Ballantyne 2017; Osterkamp and Burn 2003; Matsuoka et al. 2018; Huissteden 2020).

Where snowcover is limited, meltwater is less available. The thermal contraction cracks can develop unimpedent, but may be infilled rather with aeolian sediments. Instead of ice veins, (primary) sand veins develop. The cracking may continue similarly, so that (primary) sand wedges may form over the years. Wedges containing both ice and sediments are called composite wedges. The term *primary* is used sometimes to highlight the main difference between a sand wedge and an ice-wedge pseudomorph. The latter was originally an ice wedge as the name indicates. Over the time and under warmer climatic conditions, the ice within the wedge melted and was replaced by sediments. However, these sediments are only the secondary infill (Ballantyne 2017).

Smaller sand wedges may occur in seasonally frozen ground (Andrieux et al. 2016; Bertran et al. 2014; Wolfe et al. 2018). Most active sand wedges (i.e. wedges that still crack in winter) occur in permafrost areas with limited snow and vegetation cover, and with local sources of aeolian sediments (Ballantyne 2017; Wolfe et al. 2018). Ice wedges usually occur in continuous permafrost terrain. Therefore, ice-wedge pseudomorphs (and sand wedges) are the most important features to identify past permafrost (c.f. Ballantyne 2017; Matsuoka et al. 2018). Yet, the identification of former permafrost from ice-wedge pseudomorphs is not straight forward. It is not always possible to distinguish an ice-wedge pseudomorph from a relict composite wedge or a seasonal soil wedge. Additionally, thermal contraction cracking is found today to occur in a mid-latitude climate with only seasonal frost (Andrieux et al. 2016; Washburn 1963; Wolfe et al. 2018). Therefore, Wolfe

et al. (2018) stated that "caution must be exercised when interpreting this suite of forms and inferring paleoenvironments", especially near the southern limits of former permafrost (c.f. Ballantyne 2017).

These difficulties are probably the reason for an ongoing debate of Late Pleistocene permafrost extent in Europe. Lots of ice-wedge pseudomorphs and sand wedges were discovered in France, that can be associated to the Late Pleistocene and thus to the approximate period of the LGM. They

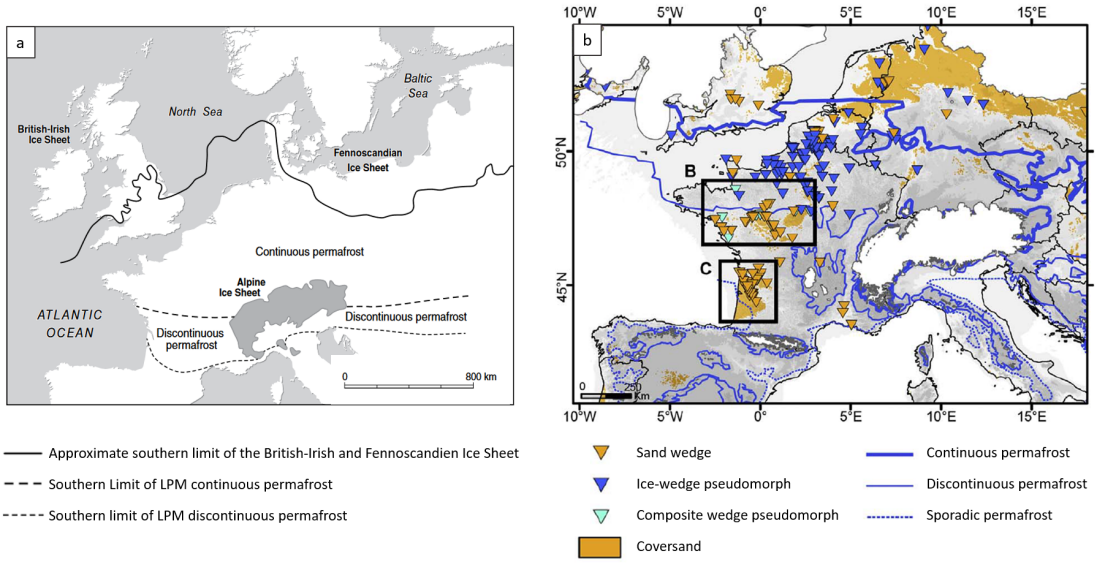

Figure 2.7: Maps of permafrost occurence in Europe during the Late Pleistocene. *(a)* Reconstructed permafrost border after Vandenberghe et al. 2014, figure from Ballantyne (2017); Fig. 16.11. *(b)* Ice-wedge pseudomorph, sand and composite wedge occurence and reconstructed permafrost border after Andrieux et al. (2018) (adapted after their Fig. 1).

are mapped in Fig. 2.7 b. Ice-wedge pseudomorphs (blue triangles in the figure) are widespread in Northern France and do not extent farther south than 47.5° N. Relict sand wedges (orange triangles) are more common between 47.5° N and 45° N with two locations of particularly frequent occurence, one in the Loire Valley (Region B) and the other in Northern Aquitaine (Region C) (Andrieux et al. 2016; Andrieux et al. 2018; Bertran et al. 2014). According to the general assumption that these wedges form within permafrost, the boundaries of maximum extending permafrost were estimated to be in mid-France for continuous and Southern France for discontinuos permafrost (Vandenberghe et al. 2014). They are depicted in Fig. 2.7 a. However, they do not fall precisely to the LGM, but to a time with even colder conditions (at about 31-24 ka), for which Vandenberghe et al. (2014) introduced the term Last Permafrost Maximum (LPM).

These boundaries were generally accepted, until the occurence of sand wedges within seasonally frozen ground as described above got more into focus. The periglacial features in France were analyzed in detail by Bertran et al. (2014), Andrieux et al. (2016), and Andrieux et al. (2018). Based on the almost exclusive presence of sand wedges south of 47.5° N, they inferred that the conditions during the Late Pleistocene did not allow large ice-wedges to grow. Moreover, they found a correlation between the depth (and the width) of the sand wedges and the latitude of their occurence. This lead to the conclusion that the sand wedges developed in the southern limit of the area affected by thermal contraction and thus in deep seasonal ground or sporadic discontinuous

permafrost (Andrieux et al. 2016) and that “France has probably never been affected by continuous permafrost”(Andrieux et al. 2016). The boundaries Andrieux et al. (2018) suggested instead are depicted in Fig. 2.7 b.
Andrieux et al. (2018) mention a study on groundwater recharge of deep aquifers that support their recent permafrost boundaries (Jiraková et al. 2011). It is shown that aquifers in Northeastern France were not recharged between 30 and 19 ka, whereas this is not the case in regions of the Paris Basin and Northern Aquitaine. Permafrost occurence in the regions with continuous recharging is thus even less likely.

Multiple attempts have been made to infer permafrost occurence from climate model data. The concepts vary from rough estimates with many simplifications to sophisticated permafrost models which require a considerable amount of computational capacity. In the following section, some of the approaches will be introduced.
Liu and Jiang (2016b) distinguish direct and indirect methods, where the direct methods use the fact that permafrost is defined solely on the basis of soil temperatures. It is thus possible, to simply take the modeled soil temperature and diagnose permafrost where temperatures are below $0\,^{\circ}\mathrm{C}$. Approaches differ slightly in the considered depth. Slater and Lawrence (2013) propose to take the MAGT at some depth (they use temperatures at 3.5 m depth). Others analyse the temperature at different depths separately and infer permafrost where the mean temperature of the soil layers is at or below $0\,^{\circ}\mathrm{C}$ in any layer (Liu and Jiang 2016a; Liu and Jiang 2016b; Saito et al. 2013).
Indirect approaches are often used when the climate model output does not contain soil temperatures as it was the case before PMIP3 (c.f. Saito et al. 2013). The most simple indirect method is to investigate the aboveground mean annual air temperature (MAAT). Threshold values are derived from study sites with present-day permafrost. Continuous permafrost is inferred for regions with MAAT $< -8\,^{\circ}\mathrm{C}$, and discontinuous permafrost requires MAAT $< -4\,^{\circ}\mathrm{C}$ (c.f. Vandenberghe et al. (2012) and Tab. 2.1). The values deviate slightly for different soil types. In fine grained soils, such as loess, permafrost might develop under less cold conditions than required for coarse-grained sand or gravel (Renssen and Vandenberghe 2003). Furthermore, the effects of snow and vegetation cover on the soil temperature can not be regarded with the air temperature. To allow for these uncertainties, an error bar of $\pm 2\,^{\circ}\mathrm{C}$ for both continuous and discontinuous limiting values is included (Vandenberghe et al. 2012). Among others, this method was used by Liu and Jiang

Table 2.1: Threshold values of the different parameters (MAAT, FI/TI, and SFI) to infer ground freezing conditions after Vandenberghe et al. (2012), Frauenfeld et al. (2007), and Nelson and Outcalt (1987). The abbreviations for the diagnose are as follows: CP for Continuous permafrost, DP for Discontinuous permafrost, SP for Sporadic permafrost, SFG for seasonal frozen ground and N for no freezing or no permafrost.

Diagnose	MAAT	FI/TI	SFI
CP	MAAT = $-8\pm2\,^{\circ}\mathrm{C}$	TI < 0.9FI - 2300	SFI > 0.67
DP	MAAT = $-4\pm2\,^{\circ}\mathrm{C}$	0.9FI - 2300 < TI < 2.4FI - 3300	0.6 < SFI < 0.67
SP			0.5 < SFI < 0.6
SFG		2.4FI - 3300 < TI	
N	MAAT > $0\,^{\circ}\mathrm{C}$	FI = 0	SFI < 0.5

(2016a) to investigate permafrost occurence in China during the Last Glaciation.
Several more sophisticated methods have been developed, all on the basis of surface air temperatures. It is possible to use the Freezing Index (FI) and Thawing Index (TI). These are the cumulative daily air temperatures below or above 0 °C, respectively. Comparison of both indices provide an estimate of permafrost occurence (Frauenfeld et al. 2007; Saito et al. 2013). The exact values are given in Tab. 2.1. Based on these values, Nelson and Outcalt (1987) developed two additional indices. First the Air Frost Number (F), which is defined as

$$\mathrm{F} = \frac{\sqrt{\mathrm{FI}}}{\sqrt{\mathrm{FI}} + \sqrt{\mathrm{TI}}}. \tag{2.1}$$

The Air Frost Number was extended to account for snow cover effects. The resulting Surface Frost Index (SFI) is calculated according to Eq. (2.1), but with an adapted Freezing Index. The absolute values of actual air temperature below 0 °C that have to be summed up for the FI are reduced according to an estimated snow thickness. Both F and SFI are defined between zero and one. The corresponding values for permafrost occurence can be found in Tab. 2.1.
The Surface Frost Number is well established and was used in several studies, with only minor changes of the original method. For example, monthly model output was used instead of summing up daily air temperatures (c.f. Frauenfeld et al. 2007; Liu and Jiang 2016b). Slater and Lawrence (2013) weighted the snow depth for each month to consider snow accumulation effects and Stendel and Christensen (2002) replaced the surface air temperature with the temperature of the deepest soil layer.
Selected approaches will be applied to the climate model data analysed in this study. The results will be compared with the previously introduced proxy-based permafrost extent that is depicted in Fig. 2.7 b.

3 Models and Data

In this study, we use two Global Climate Models (GCMs) as forcing models for the regional simulations: the Max-Planck-Institute Earth System Model (MPI-ESM) and the ECHAM6-FESOM (EC6F) model. The MPI-ESM was developed by the Max-Planck-Institute for Meteorology (MPI-M). It consists of four submodels and the Ocean Atmosphere Sea Ice Soil (OASIS) coupler in its third generation (Jungclaus et al. 2013). The submodels cover different components of the climate system: ECHAM6 (Stevens et al. 2013) represents the atmosphere, MPIOM (Marsland et al. 2003) the ocean, HAMOCC (Ilyina et al. 2013) the biogeochemistry of the ocean, and JSBACH (Reick et al. 2013) represents the terrestial biosphere and thus the lower boundary conditions over land. A schematic depiction can be found in Fig. 3.1. This model has been used in the Coupled

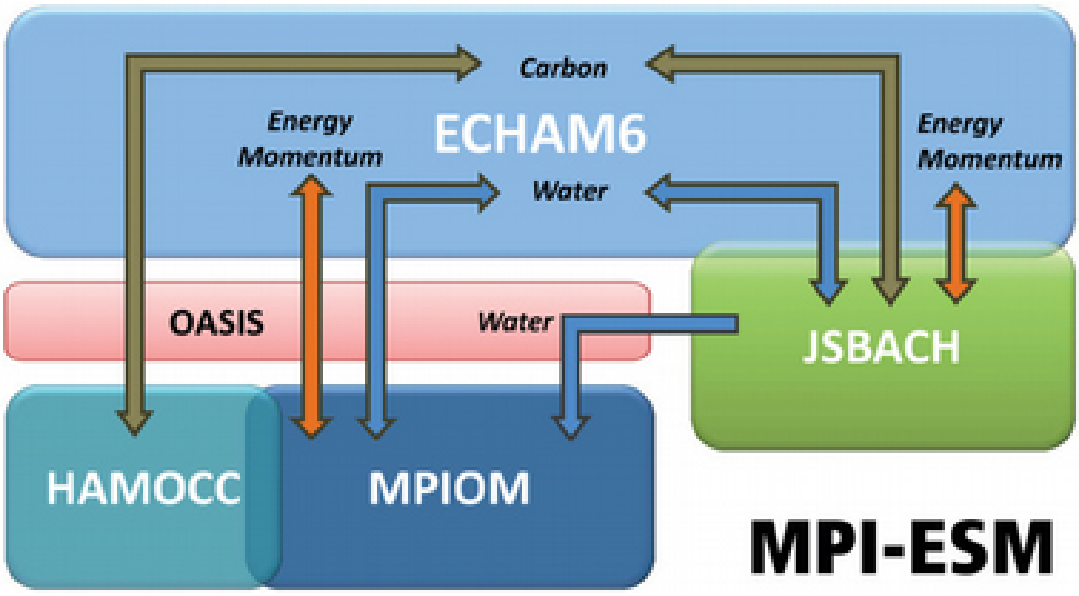

Figure 3.1: Schematic depiction of the different components of the MPI-ESM model (Giorgetta et al. 2013; Fig. 1).

Model Intercomparison Project (CMIP) - Phase 5 (Taylor et al. 2012; Jungclaus et al. 2013) and is currently participating in its sixth phase (Kageyama et al. 2020).
The atmospheric component ECHAM6 is a general circulation model. In the beginning it was used operationally by the European Centre for Medium-Range Weather Forecasts (ECMWF) and was developed further by the MPI-M in Hamburg. Its name is a combination of both contributers, EC + HAM. This model already exists in its sixth generation and is a spectral atmospheric model that combines diabatic processes and large-scale circulations (Stevens et al. 2013). The general circulation model for the ocean solves the primitive equations with the hydrostatic and the Boussinesq assumptions and contains a dynamic and thermodynamic sea ice model (Marsland et al. 2003).
The version of the MPI-ESM used in this study is the MPI-ESM-P, in which the model is adapted

for paleosimulations. These are not only simulations of the LGM, but also of the Mid-Holocene, and the last millenium within the framework of CMIP 5 and the PMIP - Phase 3 (Braconnot et al. 2012). The configuration is almost identical to that of the MPI-ESM at a lower resolution MPI-ESM-LR: The atmospheric model ECHAM6 operates at a resolution of T63 (triangular truncation at wave number 63), L47. This means an approximate resolution of 1.875° on a Gaussian grid with 47 vertical levels, which represent the atmosphere up to 0.01 hPa (Jungclaus et al. 2013). The ocean component runs at a resolution of GR15 (grid resolution of 1.5°), L40. The MPI-ESM-P only deviates from the MPI-ESM-LR regarding vegetation and orbital parameter settings: Instead of a dynamical vegetation and land-use module, the paleo version of this model uses a globally prescribed sequence of vegetation and land-use (c.f. Pongratz et al. 2008) and the orbital parameters are also prescribed rather than calculated within the simulations (c.f. Jungclaus et al. 2013; Giorgetta et al. 2013).

The other global climate model used in this study, is the ECHAM6-FESOM model. It consists of an atmospheric and an ocean model. The atmospheric model is the same as implemented in the MPI-ESM, ECHAM6 in its low resolution as in the MPI-ESM-P model. The land surface model JSBACH is also included and the ocean is represented by the Finite Element Sea ice-Ocean Model (FESOM) in its version 1.4 (Danilov et al. 2004; Wang et al. 2014). They are coupled every six hours via the OASIS3-Model Coupling Toolkit coupler (Valcke 2013). FESOM and its coupling to ECHAM6 was developed at the Alfred Wegener Institute (AWI), Helmholtz Centre for Polar and Marine Research in Bremerhaven, Germany. FESOM is the first ocean general circulation model that uses unstructured meshes, which means, that the grid can contain several different shaped and sized boxes (in the case of FESOM: triangular surface grids (c.f. Rackow et al. 2018)). Thus, the resolution can vary within one simulation (Wang et al. 2014). This is an advantage, because it allows to enhance the horizontal resolution solely in dynamically active regions and to keep a lower resolution elsewhere. In a regular mesh, it would be necessary to increase the resolution globally, which would increase the computational costs considerably (c.f. Sidorenko et al. 2015). All global climate models participating in CMIP 5 are realized in only one resolution at a time. This is an established approach, but according to Rackow et al. (2018), typical biases for these models exist. Reasons may lie in a too coarse resolution in key regions. Although this is the first global model using an unstructured grid for its ocean component, studies state that ECHAM6-FESOM "can be considered a 'state-of-the-art' global coupled climate model" (Rackow et al. 2018) and that it "performs at least as well as some of the most sophisticated climate models participating in the fifth phase of the Coupled Model Intercomparison Project" (Sidorenko et al. 2015). Under the name of AWI-ESM, it currently participates in the CMIP 6/PMIP 4 (Rackow et al. 2018; Semmler et al. 2020).

The forcing simulations of the MPI-ESM model are performed within the framework of PMIP 3. Even though the EC6F model did not take part in this project, the simulations used for the present study are set up accordingly: The relevant steady state time slice experiments with constant forcing for the LGM are defined in the PMIP 3 "21 ka - Last Glacial Maximum" experiment[1] (Braconnot et al. 2012). The boundary conditions and model parameters are set according to best estimates of the conditions during the LGM. For instance, the coastlines are adapted to the lower sea levels,

[1] `http://pmip3.lsce.ipsl.fr/`

and the ice sheets are extended. For this purpose, the ice sheet data ICE-6G (Peltier et al. 2015), Australian National University Ice Model (Lambeck et al. 2002; Lambeck and Chappell 2001), and GLAC-1 (Tarasov and Peltier 2003; Tarasov and Peltier 2002) are blended, since there are uncertainties in each reconstruction which are reduced by using the mean of all three reconstructions (c.f. Braconnot et al. 2012). Moreover, the orbital parameters and the greenhouse gas concentrations are set to values reasonable for the LGM.

Apart from the LGM simulations, Pre-Industrial (PI) control runs are conducted within PMIP 3. These control runs aim to simulate the climate under pre-industrial conditions with a constant forcing. The model output can thus be compared to present-day climate conditions and reanalyses. Moreover, proxy data reflecting past climate conditions is sometimes only available as differences from today, since calibration cannot be ensured. It is therefore important to also compute these differences with the model in order to be able to compare observational and model data.

Comparison of GCM output and proxy data is challenging, for many reasons, besides calibration. The resolutions of global models are relatively coarse, whereas proxy data mostly is on a local scale. There are several ways to overcome this lack of spatial resolution. On a statistical basis, it is possible to upscale the proxy data or to downscale the climate model output. Both methods have to be calibrated with observations, which are available only on short periods. Moreover, one has to assume stationarity, which might not be given (c.f. Ludwig et al. 2019). The other way is the dynamical downscaling of the global climate model output. In order to achieve a higher horizontal and vertical resolution, a climate simulation for a smaller domain is created with a Regional Climate Model. This type of models takes global model output at its boundaries as forcing. It

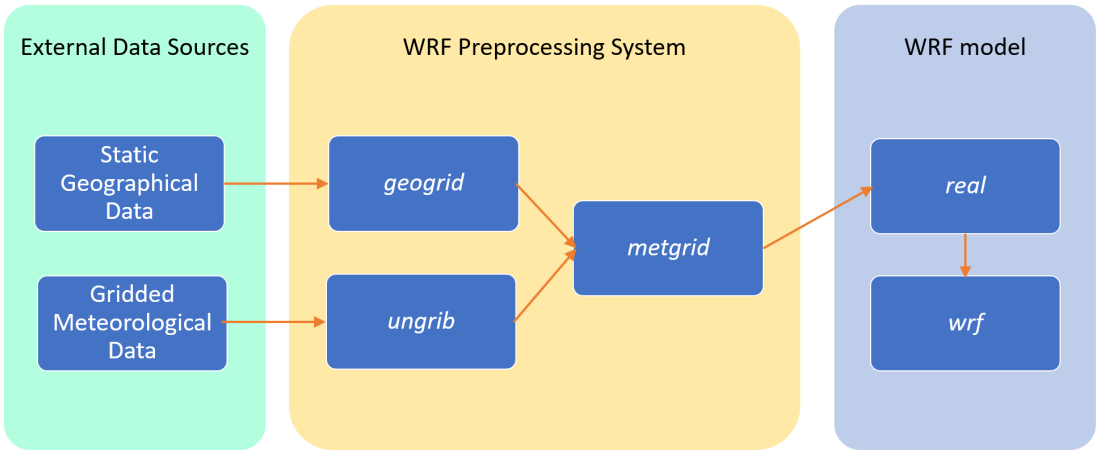

Figure 3.2: Schematic depiction of the WRF model (adapted after Skamarock et al. 2008; Fig. 5.1).

then explicitly resolves physical processes that are relevant on regional or local scales. Thus, less parametrization is necessary compared to GCMs. According to (c.f. Ludwig et al. 2019), "regional climate modeling bridges the gap between the coarse resolution of current global climate models and the regional-to-local scales". Still, model biases usually remain, either from the RCMs itself or introduced from the driving global models.

The Weather Research and Forecast (WRF) model is used in this study for dynamical downscaling of the coarse GCM data. It is a numerical weather prediction model with both operational and

research applications on several different scales, varying from large-eddy to global simulations (Skamarock et al. 2008). It consists of the WRF Preprocessing System and the WRF Software Framework (c.f. Fig. 3.2 for a schematic depiction). The WRF Preprocessing System (WPS) needs external data as input that provide information on the domain (such as domain boundaries, orography and land use) and on the meteorological fields. Both are processed by the programs *geogrid* and *ungrib*, respectively and then merged by the program *metgrid*. The files created by *metgrid* are then parsed to the main WRF model. The program *real* generates the initial and boundary fields, which are then used by the program *wrf*. The latter is the core of the WRF model and contains for example the dynamic solvers and the physics packages (c.f. Skamarock et al. 2008).

Table 3.1: Orbital parameters and trace gas concentrations for the WRF LGM simulations, based on the PMIP3 protocol. Values of pre-industrial (PI) conditions for comparison.

	Eccentricity	Obliquity	Angular Precession	CO_2	N_2O	CH_4
LGM	0.01899	22.949°	114.42	185 ppm	200 ppb	350 ppb
PI	0.01672	23.446°	102.04	280 ppm	270 ppb	760 ppb

In the present study, the WRF model is used in version 4.1.2 and with Polar-WRF extensions. The latter considers sea ice variability provided by the global forcing models. Furthermore, the model is adapted to the LGM conditions. The adaption includes modified coastlines due to a lowered sea level, as well as modified trace gas conditions and orbital parameters. The implemented values are listed in Tab. 3.1. The model domains are depicted in Fig. 3.3. The first domain covers large

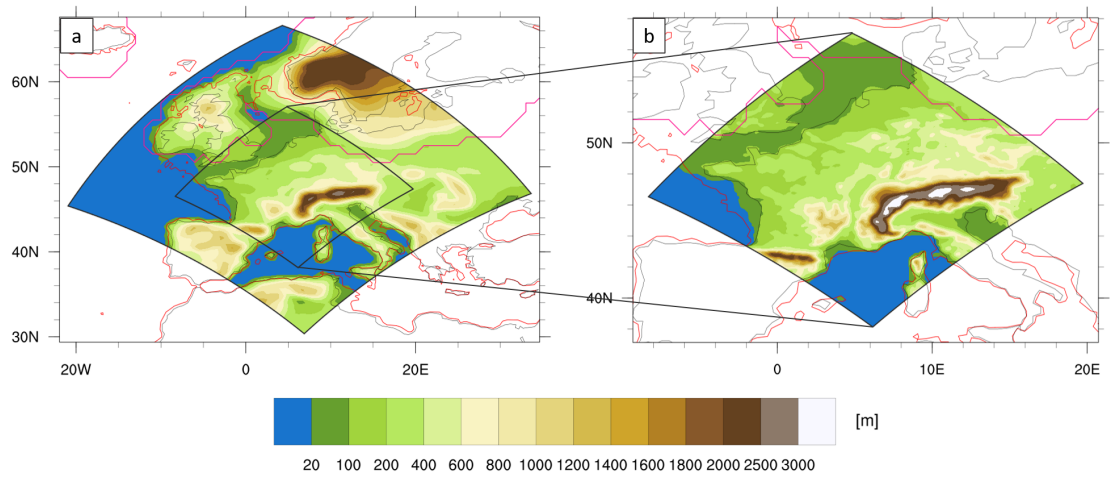

Figure 3.3: WRF model domains with LGM coastlines (red lines) and ice sheet extent (pink lines). *(a)* Domain 1 with 50 km grid spacing, *(b)* Domain 2 with 12.5 km grid spacing.

parts of Europe with a horizontal resolution of 50 km and 35 vertical layers up to 150 hPa. The integration time step is 240 seconds. The second, nested, domain covers parts of the Fennoscandian Ice Sheet (FIS), the Alps, and especially France, with is the region of interest regarding the LGM permafrost border. Its horizontal resolution is 12.5 km and the integration time step is 48 seconds. The full set of chosen phyiscal parametrization schemes and their references are listed in Tab. 3.2. The complete settings can be found in the appended namelists (c.f. Appendix, section B).

Data of the atmospheric boundary conditions (six-hourly updated) and SST and sea ice cover (daily updated) from the global simulations by the MPI-ESM-P and by the EC6F model are used for the dynamical downscaling. With the WRF model, 32 years are simulated with data of each forcing model. The first two years are used as a spin-up and are excluded from further analysis. This way it is ensured, that the atmosphere and soil properties and processes are in equilibrium.

Table 3.2: Physical parametrization schemes used for the regional simulations.

	WRF-namelist option	Scheme and Reference
Micro Physics	mp_physics = 4	WRF Single-moment 5-class Scheme Hong et al. 2004
Radiation	ra_sw_physics = 4 ra_lw_physics = 4	rrtmg scheme Iacono et al. 2008
Surface Layer	sf_sfclay_physics = 1	Revised MM5 Monin-Obukhov scheme Jiménez et al. 2012
Land Surface	sf_surface_physics = 2	unified Noah Land Surface Model Tewari et al. 2004
Planetary Boundary Layer	bl_pbl_physics = 1	Yonsei University Scheme (YSU scheme) Hong et al. 2006
Cumulus Parametrization	cu_physics = 1	Kain-Fritsch Scheme Kain 2004

4 Results

In this chapter the results of this study will be presented in three parts. First, the climate of the global forcing model simulations will be analyzed, followed by their regional counterpart. The third part addresses the reconstruction of permafrost and ground cracking regions based on the simulations analyzed beforehand.

4.1 Climate of the Global Forcing Model Simulations

In the following section, the characteristics of the global climate model simulations introduced in the previous chapter (Chap. 3) will be analyzed. The LGM simulations of the MPI-ESM-P (henceforth MPI) and the ECHAM6-FESOM (henceforth EC6F) act as drivers for regional climate model simulations with WRF. It is important to investigate the climatic mean state and possible biases of the global projections in order to be able to interpret the regional simulations accurately. Not only the LGM simulations of the two global climate models, but also the respective pre-industrial (PI) control runs are considered in this chapter. The simulations are abbreviated as followed: MPI-PI for the MPI simulations under PI conditions, MPI-LGM for the simulations under LGM conditions, and EC6F-PI and EC6F-LGM accordingly.
Although global simulations were performed, only a part of the Northern Hemisphere centered around the North Atlantic is depicted and analyzed with emphasis on Europe. The analysis is focused on the main differences between the LGM and the PI control run within the models as well as on the inter-model comparison for both simulations for the following climate variables: SST, sea ice fraction (SIC), wind speed at 300 hPa and 10 m, total precipitation, and 2 m air temperature in annual and seasonal means.
Beforehand, 30 years of ERA5 reanalysis data for Europe (1980 - 2009) (Copernicus Climate Change Service (C3S) 2017) are used to compare the 2 m air temperature and total precipitation as simulated under PI conditions with the reanalysis data. There is no reanalysis data of pre-industrial times available to compare with, so the values might deviate. Nevertheless, the comparison in Fig. 4.1 and Fig. 4.2 can give an impression whether the simulations reflect the right order of magnitude.
The simulated 2 m air temperature distributions under PI conditions are very similar over Europe and only deviate stronger over the North Atlantic, where the MPI-PI is colder (c.f. Fig. 4.1 b and c). Overall the simulations seem to be consistent with the reanalysis data (c.f. Fig. 4.1 d and e), despite the tendency towards lower temperatures in the simulations. It seems likely that this is already a signal of climate change in the ERA5 data. Temperature deviations are highest in the polar region, which is in accordance with the phenomenon of polar amplification of climate warming (c.f. Screen and Simmonds 2010). Furthermore, the temperature differences over the North Atlantic might arise from a warmer ocean in the ERA5 data and do not necessarily suggest too

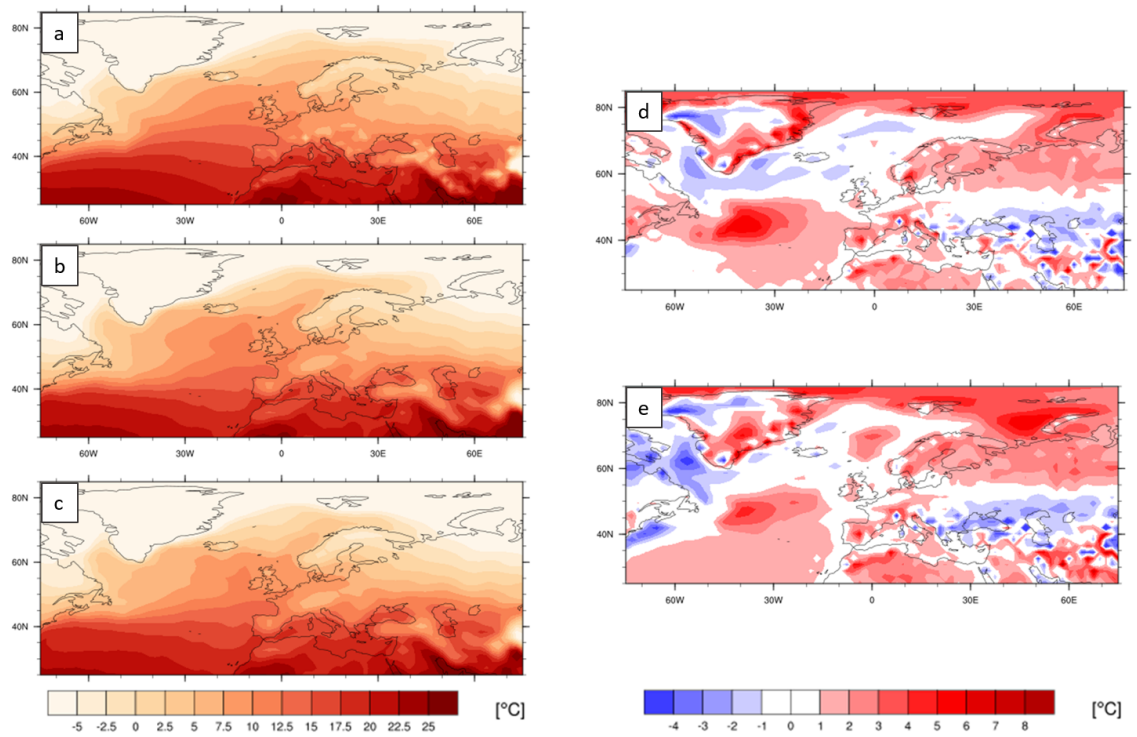

Figure 4.1: Comparison of annual mean 2 m air temperature (in °C). Absolute values of ERA5 reanalysis data *(a)*, MPI-PI simulation *(b)*, and EC6F-PI simulation *(c)*, and differences between ERA5 and MPI-PI *(d)*, as well as between ERA5 and EC6F-PI *(e)*.

cold PI simulations of the models.

There is a high precipitation amount over the North Atlantic in all three data sets. Values in EC6F-PI are in overall agreement with the ERA5 precipitation data, with a slight deviation towards too less precipitation in the simulation. However, the precipitation in the MPI-PI simulation is partly overestimated.

Focusing on Europe, both simulations show four areas of enhanced precipitation, that are in accordance with the reanalysis data: over the Alps, at the northwestern edge of the Iberian Peninsula, over Southern Norway, and over Ireland and Northern Great Britain. Only there, annual mean precipitation exceed values of 2-3 mm/day in the reanalysis data. This is, however, not captured by the global climate models. Even the drier EC6F-PI simulation show slightly more precipitation in annual mean and the MPI-PI precipitation deviates again more from the ERA5 data.

As described in the previous chapter, the two global climate models consist of the same atmospheric and land surface components, but differ in the ocean submodel. Therefore, the analysis is started with the SST distribution. The SSTs are colder under LGM boundary conditions compared to the simulations under PI conditions, as expected (c.f. Fig. 4.3 a and b). For the MPI-ESM model, the differences are especially large in the Eastern Arctic Ocean, but they even change in sign for a region in the North Atlantic. This does not agree with proxy data (c.f. MARGO Project Members 2009) and is a known issue for this and other PMIP3 models (c.f. Wang et al. 2013; Ludwig et al. 2016; Ludwig et al. 2017). The EC6F simulations do not show this warmer pattern of the North Atlantic and the SSTs are colder throughout the region of interest. The largest differences of about $-7\,°C$ can be found in the North Atlantic off the coast of North America. The Arctic Ocean varies only by 1 to 3 °C towards a colder LGM-SSTs.

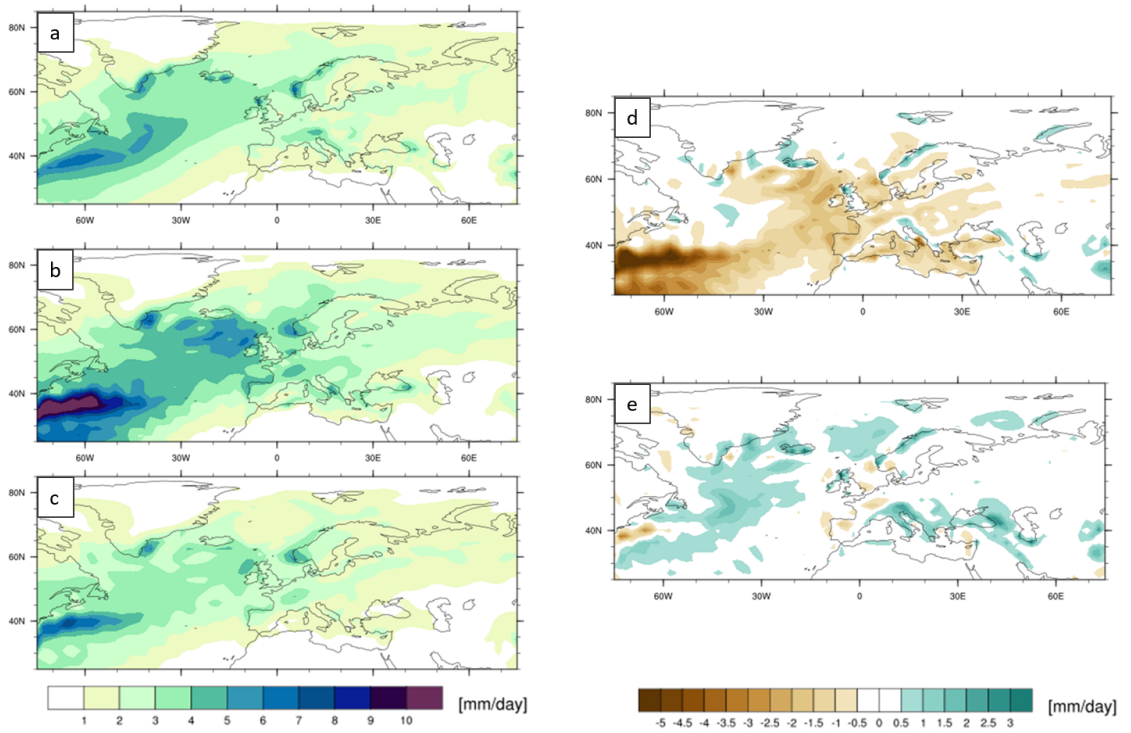

Figure 4.2: Comparison of annual mean precipitation (in mm/day). Absolute values of ERA5 reanalysis data *(a)*, MIP-PI simulation *(b)*, and EC6F-PI simulation *(c)*, and differences between ERA5 and MPI-PI *(d)*, as well as between ERA5 and EC6F-PI *(e)*.

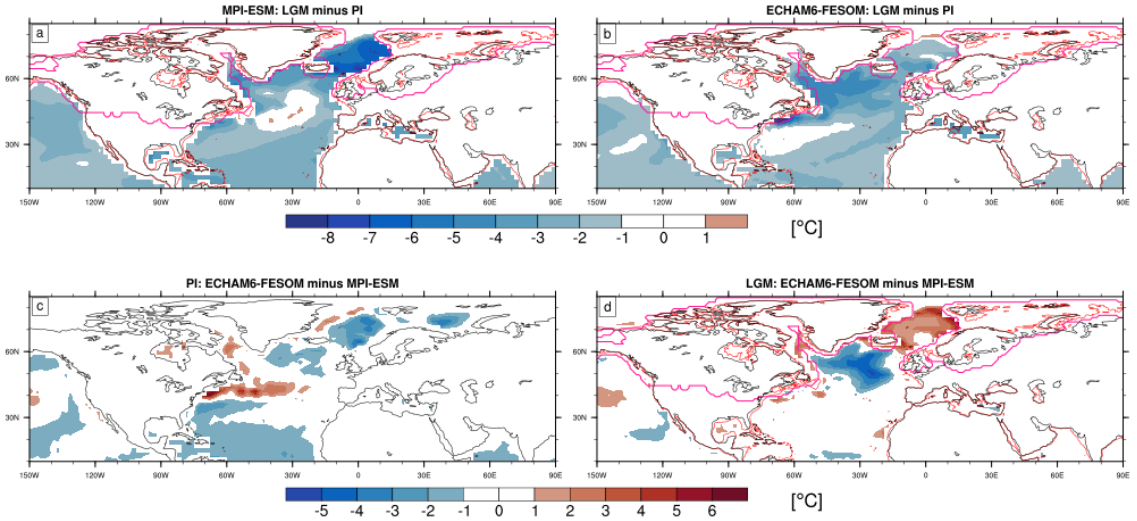

Figure 4.3: Distribution of SSTs in annual mean (in °C). *(a)* Differences of the SST distribution between MPI-LGM minus MPI-PI. *(b)* as *(a)* but for the EC6F model simulations. *(c)* Differences of the SST distribution between EC6F-PI minus MPI-PI. *(d)* as *(c)* but for LGM simulations.

The Gulf Stream in the EC6F-PI simulation is shifted to the north, which explains the differences in the SST distribution off the coast of North America (c.f. Fig. 4.3 c). Apart from that region, the EC6F-PI simulation shows slightly colder SSTs than the MPI-PI simulation (c.f. Fig. 4.3 c). Differences between the two LGM simulations as depicted in Fig. 4.3 d are largest in the Arctic Ocean and in the North Atlantic. In the Arctic Ocean, the SSTs in the EC6F-LGM simulation are considerably higher than in the MPI-LGM simulation. Differences of similar magnitude, but with

opposite sign can be found in the North Atlantic due to the above described warmer pattern of the MPI-LGM simulation. These two patterns are visible in each season, but with different magnitudes: In winter and spring, temperatures of the North Atlantic show largest deviations between MPI-ESM and EC6F, whereas in autumn and especially in summer the EC6Fs' Arctic Ocean is warmer than that of the MPI-ESM simulation (not shown).

Differences in the Arctic Ocean can be explained with the Sea Ice Distribution (c.f. Fig. 4.4). There is more sea ice in the colder climate of the LGM simulations in the North Atlantic than under PI condition. Only in the EC6F simulations there is little less sea ice near Spitsbergen during the LGM than under PI conditions. Apart from smaller differences at the ice sheet edges, the SIC is similar in the PI simulations of the two models (c.f. Fig. 4.4 c). Differences are greater for simulations of the LGM climate (c.f. Fig. 4.4 d). Particularly, the sea ice fraction in the Arctic Ocean is up to 70 % smaller in the EC6F-LGM simulation than in the MPI-LGM simulation. This also holds for each season. Only the structure of the pattern in the North Atlantic varies. This structure of differences in SIC is consistent with the SSTs in the Arctic Ocean, where less sea ice corresponds to higher SSTs.

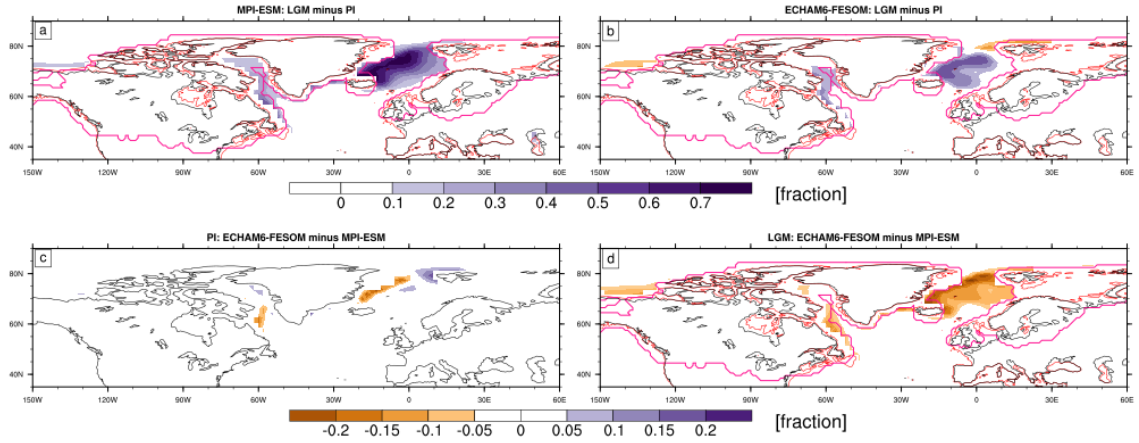

Figure 4.4: Distribution of SIC in annual mean (in fractions). *(a)* Differences of the SIC distribution between MPI-LGM minus MPI-PI. *(b)* as *(a)* but for the EC6F model simulations. *(c)* Differences of the SIC distribution between EC6F-PI minus MPI-PI. *(d)* as *(c)* but for LGM simulations.

Absolute patterns of the Sea Ice Fraction during the LGM show an almost completely frozen Arctic Ocean during winter and spring seasons in the MPI-LGM simulation (c.f. Fig. 4.5 a and c). Summer and autumn do not contain as much sea ice, but the Arctic Ocean is still notably ice-covered. Bringing the EC6F simulations into focus, the ice-free Arctic Ocean in summer and autumn attracts attention (c.f. Fig. 4.5 f and h). During winter and spring, the Arctic Ocean is partly ice-covered but far from being frozen completely.

The analysis of wind speed at 300 hPa gives insights into the jet structure and strength. Both models show a stronger jet with mean annual wind speeds of up to 45 m/s under LGM conditions compared to the simulations under PI conditions (c.f. Fig. 4.6 a and b). Especially over the North Atlantic, south-eastward of the LIS, the wind speed is up to 14 m/s higher in annual mean. North- and southward of the jet, the wind speed is around 2-4 m/s weaker during the LGM. Even though the values of the differences are quite similar for both models, the structure is not: For the MPI-ESM simulations, the jet is narrower and deflected to the north. It reaches Europe at the

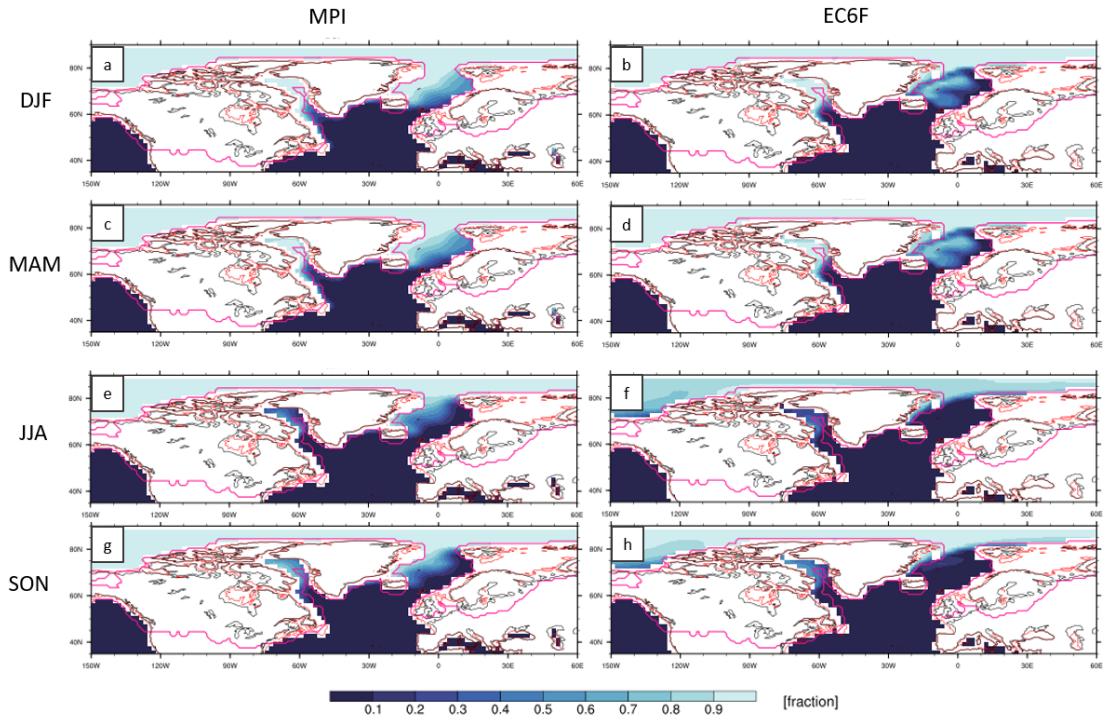

Figure 4.5: Distribution of SIC in seasonal means with LGM boundary conditions. Left column MPI-LGM SIC distribution and right column EC6F-LGM SIC distribution in winter *(a* and *b*, respectively*)*, in spring *(c* and *d*, respectively*)*, in summer *(e* and *f*, respectively*)*, and in autumn *(g* and *h*, respectively*)*.

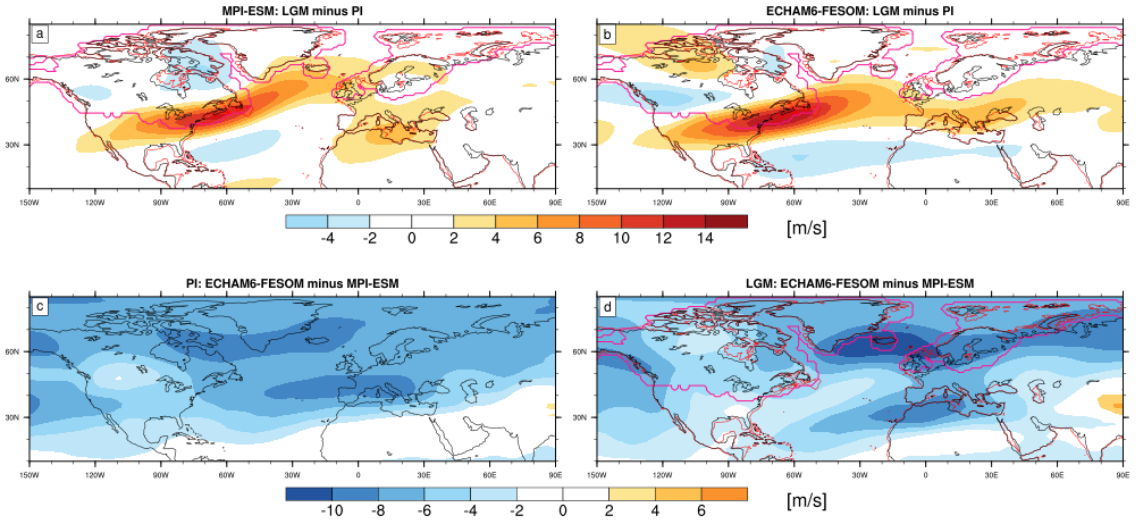

Figure 4.6: Distribution of wind speed in 300 hPa in annual mean (in m/s). *(a)* Differences of the wind speed in 300 hPa between MPI-LGM minus MPI-PI. *(b)* as *(a)* but for the EC6F model simulations. *(c)* Differences of the wind speed in 300 hPa between EC6F-PI minus MPI-PI. *(d)* as *(c)* but for LGM simulations.

latitude of Ireland. Wind speeds over the FIS are similar in the MPI-LGM and the MPI-PI simulations, or slightly higher. The region of weaker wind speeds southward of the jet position is also deflected to the north and ends in front of the Iberian Peninsula and Africa, where again stronger winds can be found in the LGM simulation, especially over the Mediterranean. The structure of the wind speed differences in the EC6F simulations is more zonally. This is true at the jet position,

which approaches Europe at the latitude of the Iberian Peninsula and France and penetrades farther into the continent. The same is true for the slightly lower wind speeds southward, which continue over Africa and the Arabian Pensinsula. Over the FIS, wind speeds are almost similar or slightly lower during the LGM.

Comparing the two models, evidently, the EC6F model simulates weaker winds at 300 hPa than

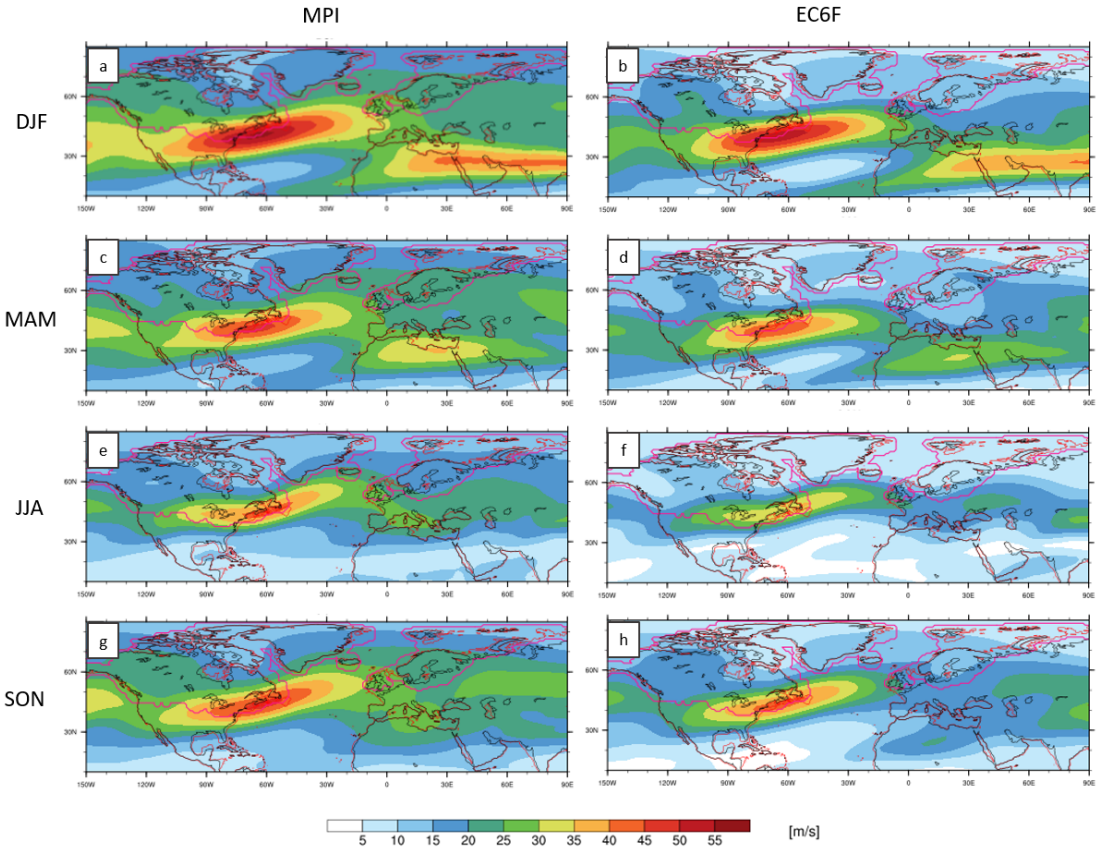

Figure 4.7: Distribution of the wind speed in 300 hPa in seasonal means with LGM boundary conditions. Left column MPI-LGM distribution and right column EC6F-LGM distribution in winter *(a* and *b*, respectively*)*, in spring *(c* and *d*, respectively*)*, in summer *(e* and *f*, respectively*)*, and in autumn *(g* and *h*, respectively*)*.

the MPI-ESM model under both PI and LGM conditions (c.f. Fig. 4.6 c and d). For the PI simulations, there are two regions with weaker wind speeds of up to 10 m/s, one over the North Atlantic off Greenland and Iceland, and one region off the Iberian Peninsula and the northern coastline of the Mediterranean. For the simulations under LGM conditions, the general picture stays the same. However, the differences are greater and the two structures with weaker wind speeds are shifted. The northern structure is centered around Iceland and reaches the FIS. The southern structure is shifted farther south and a little to the west. Strongest deviations are over North Africa.

In both models, the jet stream is strongest in winter. During this season a pronounced subtropical jet can also be observed. The MPI-LGM simulation yields a less condensed jet stream in all seasons (c.f. Fig. 4.7). Almost the whole North Atlantic experiences higher wind speeds of at least 20 m/s and up to 55 m/s. In summer, the jet is weakest in both models and meanders over the North Atlantic and Europe.

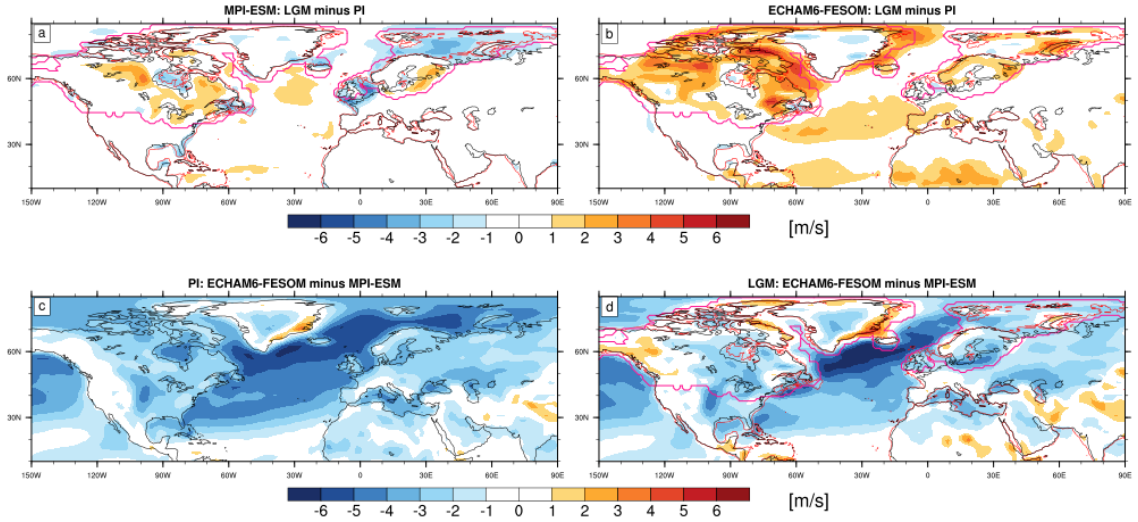

Figure 4.8: Distribution of wind speed in 10 m in annual mean (in m/s). *(a)* Differences of the wind speed in 10 m between MPI-LGM minus MPI-PI. *(b)* as *(a)* but for the EC6F model simulations. *(c)* Differences of the wind speed in 10 m between EC6F-PI minus MPI-PI. *(d)* as *(c)* but for LGM simulations.

The wind speed in 10 m is broadly similar under LGM and PI conditions in the simulations of the MPI-ESM model (c.f. Fig. 4.8 a). The wind speed is slightly higher over the North Atlantic and the Mediterranean as well as over some regions over the LIS and the FIS. At the eastern coast of America and at the ice sheet edges, as well as over today's North Sea, wind speed is lower under LGM conditions. The North Sea did not exist during the LGM, because of a lower sea level. Further, the land was partly covered by the FIS. The lower wind speeds in this region can also be observed in the EC6F simulations, but the differences there are less pronounced. In the EC6F simulations, the surface wind speed is generally higher under LGM than under PI conditions, especially at the northern and eastern ice sheet edges (c.f. Fig. 4.8 b).

In both PI and LGM simulations, the EC6F simulations show weaker surface wind speeds compared to the MPI-ESM simulations over the North Atlantic and most parts of Europe and North America (c.f. Fig. 4.8 c and d). At the eastern coast of Greenland, the wind at 10 m is stronger in the EC6F-LGM simulation in the annual mean, but also in all seasons. This might be linked to the slightly different implemented ice sheet between the two models. In winter, the difference over the North Atlantic is strongest. When looking at the absolute wind speeds for both models that are depicted in Fig. 4.9 the reason for the differences becomes clear. There is an extensive area with

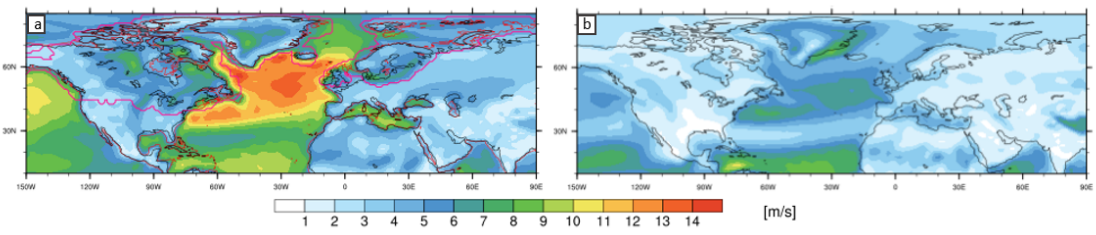

Figure 4.9: Distribution of the wind speed in 10 m in seasonal mean for winter with LGM boundary conditions. *(a)* MPI-LGM simulation and *(b)* EC6F-LGM simulation.

high wind speeds over the North Atlantic in the MPI-LGM simulation, similar to the widespread jet. In contrast, the jet in the EC6F model simulations is more condensed to a latitudinal band corresponding to the structure of the wind speed in 10 m. In both simulations the surface wind speed is reduced over land due to a higher surface roughness.

Not only the wind speed of the surface wind is influenced by the jet, but also its direction. The atmospheric flow can be investigated by a Circulation Weather Type (CWT) approach (Jones et al. 1993) that was first applied to LGM simulations by Ludwig et al. (2016). With this approach, the atmospheric flow is classified into eight different CWTs, namely northeast (NE), east (N), southeast (SE), south (S), southwest (SW), west (W), northwest (NW), north (N), cyclonic (C), and anticyclonic (A). Fig. 4.10 shows the frequency of each weather type for the MPI-LGM and the EC6F-LGM simulation for two arbitrarily chosen locations, one in Northern France (48°N, 5°E) and one near the ice sheet edge (52°N, 10°E). In both global climate model simulations, the

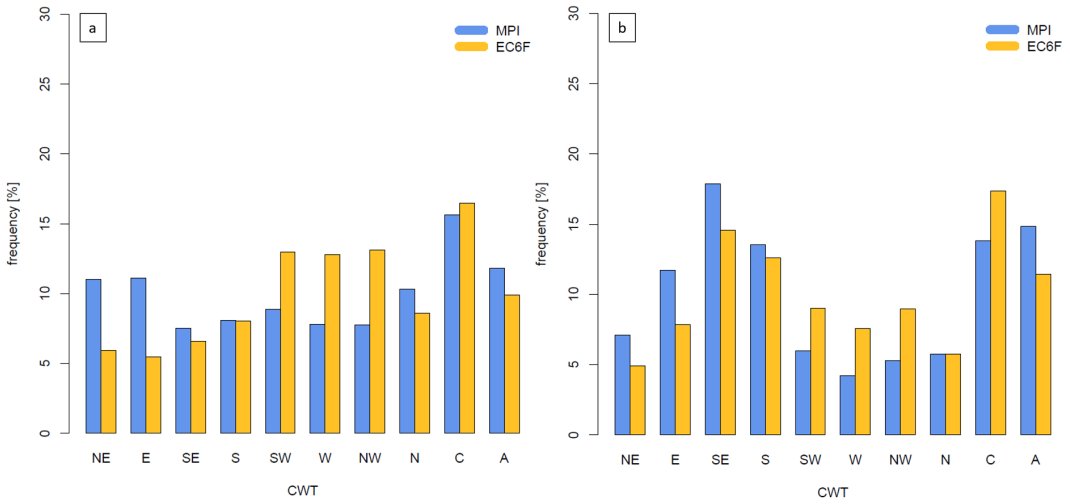

Figure 4.10: CWT frequencies of two different locations, 48°N, 5°E *(a)* and 52°N, 10°E *(b)*, for both the MPI-LGM and the EC6F-LGM simulations (adapted after Ludwig et al. 2016; Credits to Patrick Ludwig).

cyclonic weather type is prevailing, with a higher frequency in the EC6F-LGM simulation. The westerly flow is more dominant in the EC6F-LGM simulation, especially in Northern France. The westerly CWTs occur second most often, implying a stronger influence from the North Atlantic. In the MPI-LGM simulation, the westerly CWTs are less often, but easterly (northeasterly over Northern France; southeasterly near the ice sheet edge) winds are dominant. This suggests a more continental climate influence by the FIS, rather than by the North Atlantic as in EC6F.

These differences in the circulation are also reflected in the precipitation patterns. Overall the climatic conditions were drier under LGM than under PI conditions (c.f. Fig. 4.11 a and b). Despite a region off Greenland and the Southern Iberian Peninsula, the MPI-LGM simulation shows less precipitation over the North Atlantic and Europe, als well as over the regions covered by large ice sheets during the LGM than the MPI-PI simulation does over Europe. This corresponds well with the prevailing northerly and northeasterly weather types simulated by the MPI-ESM. The precipitation distribution simulated by the EC6F is similar or slightly wetter under LGM conditions in America, Southern Europe, and the southern parts of the FIS, but overall drier over the North Atlantic and over most parts of the ice sheets. Nevertheless, these regions are still drier than in the

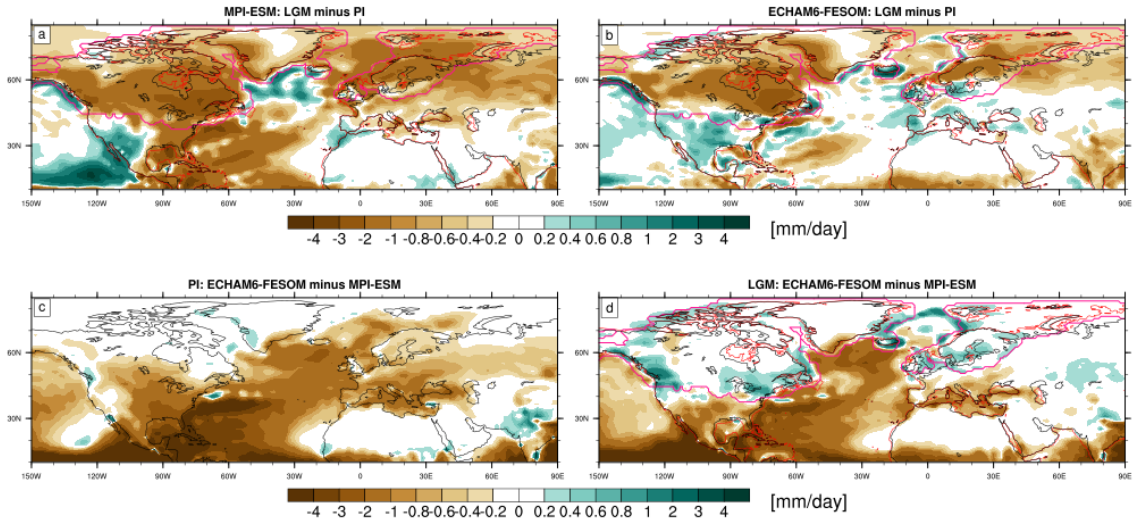

Figure 4.11: Distribution of the total precipitation in annual mean (in m/s). *(a)* Differences of the total precipitation between MPI-LGM minus MPI-PI. *(b)* as *(a)* but for the EC6F model simulations. *(c)* Differences of the total precipitation between EC6F-PI minus MPI-PI. *(d)* as *(c)* but for LGM simulations.

MPI-ESM simulations, when comparing the two model simulations under PI and LGM conditions separately (c.f. Fig. 4.11 c and d). In general, the EC6F simulations are drier, especially over the North Atlantic.

Under LGM conditions, the EC6F model simulations show more precipitation over the ice sheets, but less elsewhere in annual mean (c.f. Fig. 4.11 d). Both models show more precipitation in autumn and winter than in spring and summer. Neglecting the Intertropical Convergence Zone (ITCZ), most of the precipitation in the MPI-LGM simulation is carried out over the North Atlantic (c.f. Fig. 4.12). In autumn and winter, there is also some precipitation over the region of the Mediterranean and the Iberian Peninsula. These patterns are shifted northward in spring and summer. Despite the more cyclonic and westerly atmospheric flow, total precipitation is less in the EC6F-LGM simulation. This result is in accordance with the reduced wind speed in both 300 hPa and in 10 m. Compared to the MPI-LGM simulation, the precipitation patterns are shifted northward, and the Mediterranean almost gets no precipitation.

Comparison with proxy data from Bartlein et al. (2011) demonstrate poor agreement of the simulated LGM minus PI differences with the reconstructed estimates (c.f. Tab. 4.1). The magnitude of the changes is not reached in any location where proxy data is available. Only at two locations, the simulated precipitation differences are within two times the standard error of reconstruction. The MPI-ESM simulations lack to accurately describe the magnitude of differences, but the direction towards less precipitation under LGM conditions is reproduced correctly. For the EC6F simulations, this is not the case. Even though there is less precipitation compared to both MPI-ESM simulations, the precipitation amount increases from PI to LGM conditions in the EC6F model simulations.

Fig. 4.13 shows the surface air tempature differences of the simulations in annual mean. Comparing the PI simulations of the two models, major discrepancies are located in the North Atlantic's Gulf Stream regions off the coast of North America as well es farther north over East Canada and the Hudson Bay towards a warmer EC6F-PI simulation, also in agreement with the SST distribu-

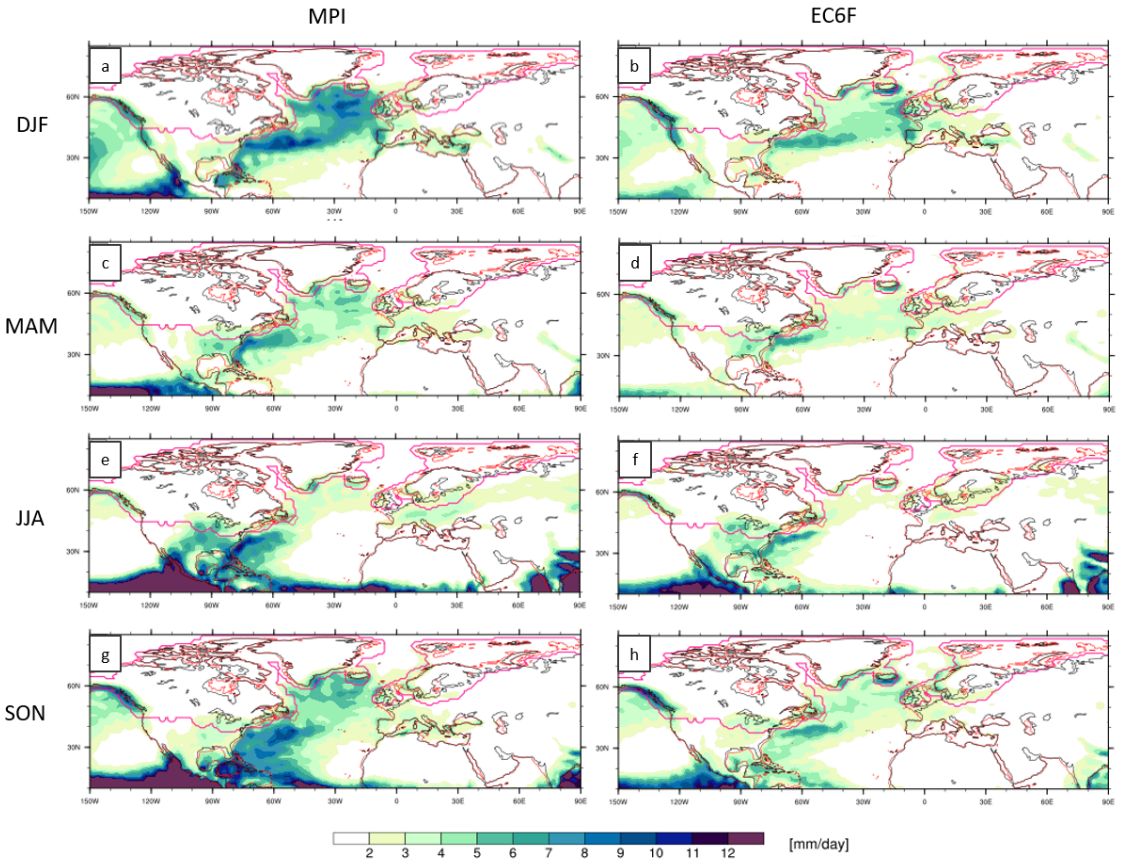

Figure 4.12: Distribution of the total precipitation in seasonal means with LGM boundary conditions. Left column MPI-LGM precipitation distribution and right column EC6F-LGM precipitation distribution in winter *(a* and *b*, respectively*)*, in spring *(c* and *d*, respectively*)*, in summer *(e* and *f*, respectively*)*, and in autumn *(g* and *h*, respectively*)*.

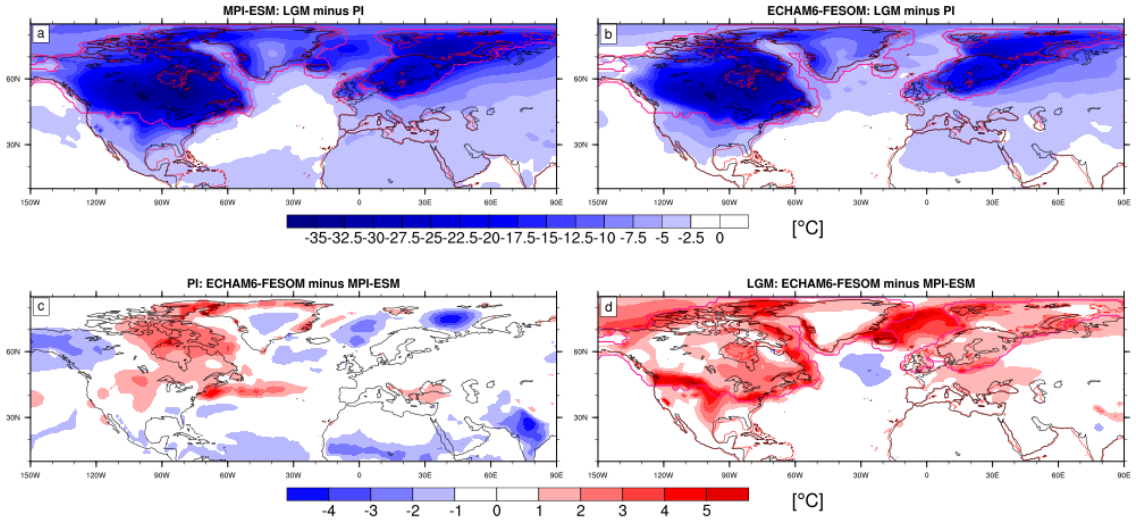

Figure 4.13: Distribution of the 2 m air temperature in annual mean (in m/s). *(a)* Differences of the 2 m air temperature between MPI-LGM minus MPI-PI. *(b)* as *(a)* but for the EC6F model simulations. *(c)* Differences of the 2 m air temperature between EC6F-PI minus MPI-PI. *(d)* as *(c)* but for LGM simulations.

Table 4.1: Proxy and model output data for change of LGM mean annual precipitation (Δ MAP at considered grid points and standard error of the reconstruction (SE MAP) as given by Bartlein et al. (2011). Dark green shading: modeled precipitation change within standard error estimates. Mid-green: modeled precipitation change within 1.5 times standard error of estimates. Light green: modeled precipitation change within 2 times standard error of estimates. Mean precipitation changes are given in bottom row. All precipitation values given in mm/year (Table adapted after Ludwig et al. 2016, their Tab. S5).

		[Bartlein et al., 2011]		MPI-ESM	EC6F
Lat	Lon	Δ MAP	SE MAT	Δ MAP	Δ MAP
43N	7W	-653	178	-2	21
37N	3W	-96	69	11	10
43N	1W	-500	52	-30	0
43N	3E	-327	87	-7	8
45N	3E	-385	113	-18	7
45N	5E	-360	98	-15	17
47N	7E	-440	114	-22	13
43N	11E	-369	98	-3	9
41N	13E	-427	99	-10	6
41N	15E	-200	111	-16	10
39N	21E	-532	175	-12	-12
41N	21E	-240	103	-8	15
39N	23E	-246	87	2	4
49N	27E	-206	46	-11	9
		-356	102	-10	8

tion (c.f. Fig. 4.1 and Fig. 4.13 c). In contrast, lower temperatures in the EC6F-PI simulation can be found over Western Canada and most of the Arctic Ocean except the Gulff Strean regions.
Both models show significant colder temperatures under LGM than under PI conditions almost everywhere in the annual mean (c.f. Fig. 4.13 a and b). Highest deviations can be found in North America and Northern Europe at the LGM positions of the Laurentide and Fennoscandian Ice Sheets. A small area over the North Atlantic is slightly warmer in the MPI-LGM simulation than in the MPI-PI simulation. This is in agreement with the above described SST distribution. Accordingly, the EC6F simulations do not show this feature. Therefore, the 2 m air temperatures in this region are lower in the EC6F-LGM simulation than in the MPI-LGM simulation by up to $-4\,^{\circ}\mathrm{C}$ (c.f. Fig. 4.13 d). Over the continents, temperatures are generally higher in the LGM simulation of the EC6F model. The temperature differences become highest (up to $14\,^{\circ}\mathrm{C}$) over the Western Arctic Ocean and at the ice sheet edges, which can directly be linked to the slightly smaller ice sheet in the EC6F simulation. The differences in the Arctic Oceans are in agreement with the SST distribution and correlates with the sea ice cover in both models.

Seasonally the temperatures vary by up to 50 °C in both model simulations under LGM conditions. Largest variations can be found over the ice sheets, where the air temperature can get very cold. As expected, the air in 2 m is coldest in the polar and icy regions and warmest at the equator. During winter, differences in the Arctic Ocean get highest, whereas the ice sheet edges become more important in summer.

Table 4.2: Proxy and model output data for change of LGM mean annual 2 m air temperature (Δ MAT at considered grid points and standard error of the reconstruction (SE MAT) as given by Bartlein et al. (2011). Dark green shading: modeled temperature change within standard error estimates. Mid-green: modeled temperature change within 1.5 times standard error of estimates. Light green: modeled temperature change within 2 times standard error of estimates. Mean temperature changes are given in bottom row. All temperature values given in °C. (Table adapted after Ludwig et al. 2016, their Tab. S4).

		[Bartlein et al., 2011]		MPI-ESM	EC6-F
Lat	Lon	Δ MAT	SE MAT	Δ MAT	Δ MAT
43N	7W	-8.3	2.7	-3.3	-2.8
37N	3W	-7.1	1.2	-3.7	-3,0
43N	1W	-3.5	1.5	-5.2	-3.4
43N	3E	-6.7	1.8	-5.1	-4.0
45N	3E	-8.9	2.7	-5.6	-3.9
45N	5E	-13.9	2.3	-5.6	-4.0
47N	7E	-11.3	1.6	-6.3	-4.2
41N	13E	-6.6	2.8	-5.5	-4.8
41N	15E	-5.6	2.2	-5.6	-4.7
39N	21E	-8.1	2	-4.9	-4.1
41N	21E	-5.2	2.2	-5.3	-4.4
39N	23E	-5.2	1.7	-4.6	-3.0
49N	27E	-11	1.5	-8.2	-5.9
		-7.8	2.0	-5.3	-4.0

For the 13 locations, where the temperature differences can be compared with proxy data, the agreement for both model simulations is better for the 2 m air temperature than for total precipitation (c.f. Tab. 4.2). Overall the differences of the MPI-ESM simulations are within 1.5 times the standard error of the reconstruction. However, the cooling under LGM conditions is not strong enough at almost all locations. Since the EC6F simulation under LGM boundary conditions is warmer than the MPI-LGM simulation, the temperature distribution deviates more, and is only within two standard errors of the proxy data.

Even though the two global climate models MPI-ESM and EC6F consist of the same atmospheric component, the resulting climate and atmospheric circulation differ largely. The SST distribution might be more realistic for the simulations with the EC6F model, and the structure of the jet lies within CMIP 5 mean for the LGM simulation. When it comes to LGM minus PI comparison

with proxy data by Bartlein et al. (2011), both models underestimate the right magnitudes of the changes. The MPI-ESM simulations, however, show better agreement in terms of the direction of change.

4.2 Climate of the Regional Climate Model Simulations

The mean climatic state of the regional WRF-LGM simulations (c.f. Chap. 3) will be analysed and compared to their global counterparts in this section. The following variables will be taken into account: the 2 m air temperature, snow height and cover, surface wind and total precipitation. After this, the analysis proceeds towards the permafrost investigation by examining the soil temperatures and soil moisture content.

In both the global and the regional LGM simulations, the annual mean 2 m air temperature is considerably higher in the EC6F than in the MPI simulation (c.f. Fig.4.14). With almost 10 °C, differences are largest in the global simulations at distinct locations near the ice sheet margin. These differences are also given in the regional simulations, however, they are slightly smaller.

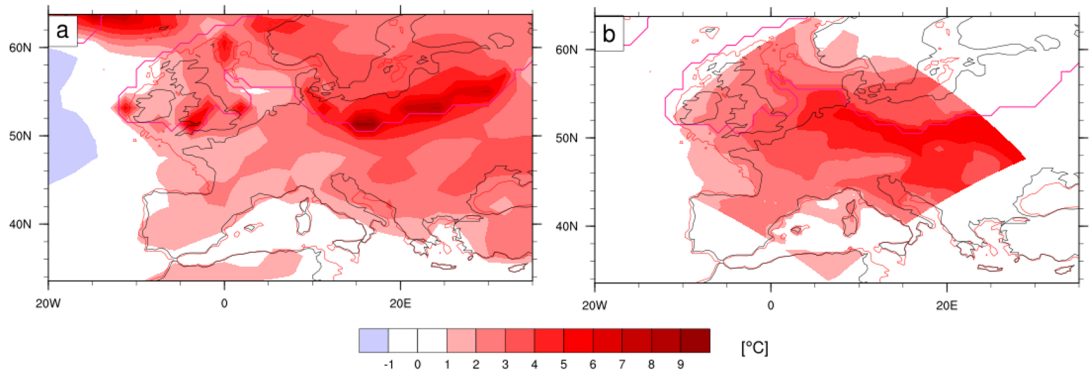

Figure 4.14: Distribution of the 2 m air temperature in annual mean (in °C). *(a)* Differences of the temperature distribution between the global climate model simulations (EC6F-LGM minus MPI-LGM). *(b)* Differences of the temperature distribution between the regional climate model simulations (WRF-AWI minus WRF-MPI).

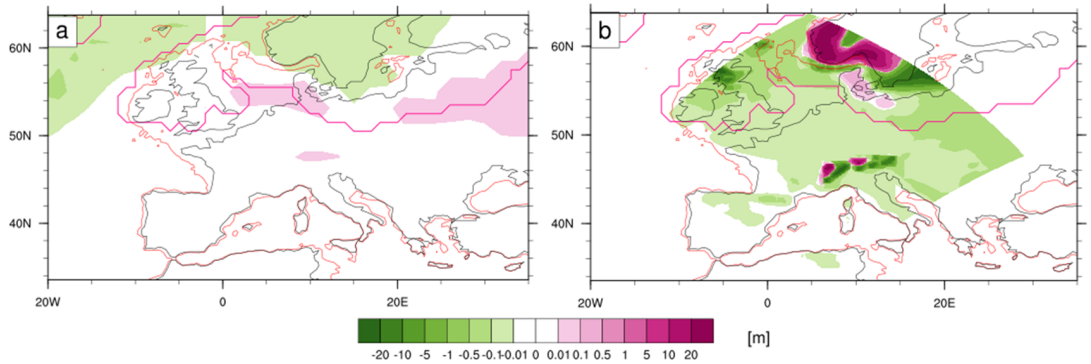

Figure 4.15: Distribution of the snow height in annual mean (in m). *(a)* Differences of the snow height distribution between the global climate model simulations (EC6F-LGM minus MPI-LGM). *(b)* Differences of the snow height distribution between the regional climate model simulations (WRF-AWI minus WRF-MPI).

In Southern and Central Europe, temperature differences from the global simulations are slightly amplified from $1-2\,°C$ to $2-4\,°C$ in the regional simulations. This sign and pattern of the differences is visible in all seasons, but winter air temperatures clearly diverge most, whereas summer air temperatures are relatively close to each other (not shown).
To understand from where these differences arise, the snow height and cover as well as the surface wind will be studied. In the global simulations, there is almost no snow in Europe. Only at the

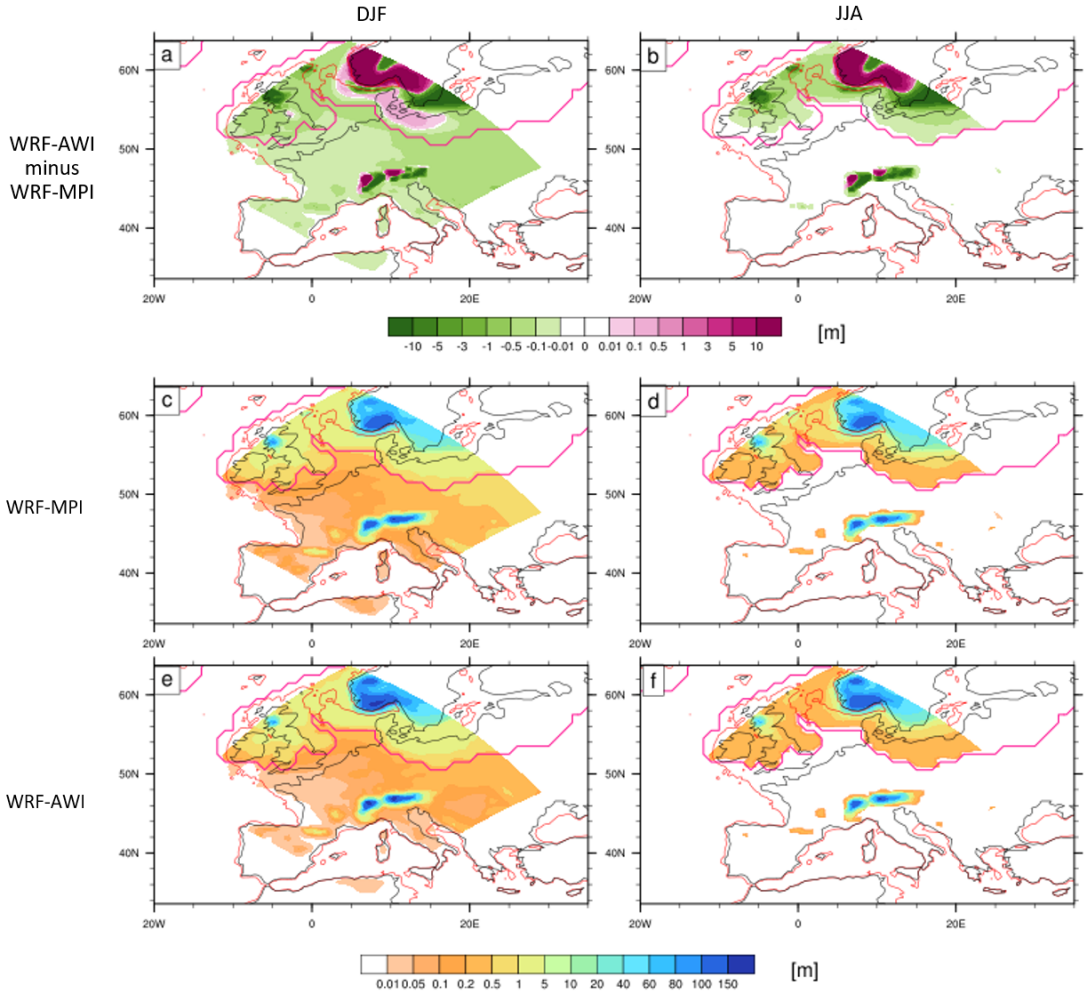

Figure 4.16: Distribution of the snow height in seasonal means for winter (left) and summer (right) (in m). *(a)* Differences of the winter snow height distribution between the regional climate model simulations (WRF-AWI minus (WRF-MPI). *(b)* as *(a)* but for summer snow height. *(c)* Absolute values of the winter snow height distribution in WRF-MPI. *(d)* as *(c)* but for the summer snow height distribution in WRF-MPI. *(e)* and *(f)* as *(c)* and *(d)* but for the WRF-AWI snow height distributions

ice sheet margins, a snow height of a few centimetres occurs in spring and winter. Differences between the two global simulations are accordingly small (c.f. Fig. 4.15 a). This is different in the regional simulations. Except in summer, almost all of the simulated region is snow covered in WRF-MPI, even though only over the FIS and the ice sheet of the Alps a snow height of several metres is reached. WRF-AWI shows markedly higher snow accumulation over the ice sheets with differences of more than 20 m, but less snow cover in Central and Southern Europe. Differences amount to 20% less snow cover in WRF-AWI in annual mean and to 40% in both spring and

winter (c.f. Fig.4.16). In summer, only the ice sheets are snow covered in both simulations and the differences are thus negligible. Since snow cools the atmosphere, more snow coverage in WRF-MPI may partly account for the 2 m air temperature differences.

In Fig. 4.17, the differences between the annual mean surface wind speed (in 10 m) are displayed for the global and regional climate model simulations.

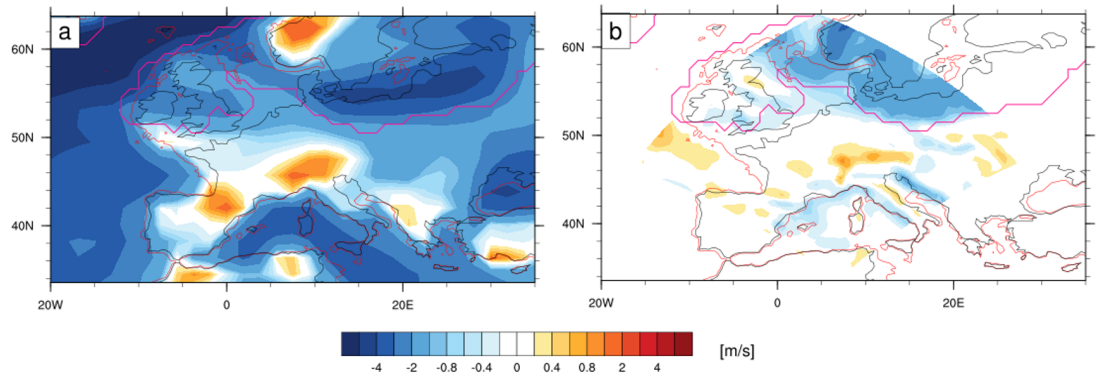

Figure 4.17: Distribution of the surface wind speed in annual mean (in m/s). *(a)* Differences of the wind speed distribution between the global climate model simulations (EC6F-LGM minus MPI-LGM). *(b)* Differences of the wind speed distribution between the regional climate model simulations (WRF-AWI minus WRF-MPI).

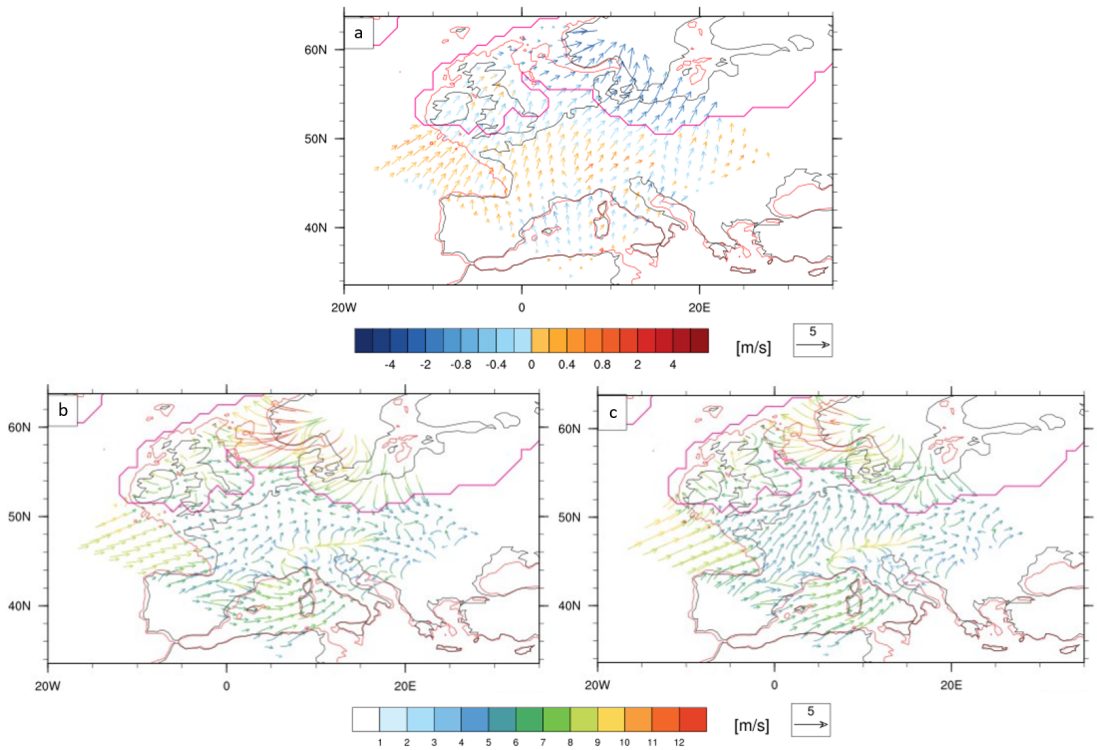

Figure 4.18: Distribution of the wind field in annual mean (vectors according to the depicted reference vector, in m/s). *(a)* Differences of the wind field distribution between the regional climete model simulations (WRF-AWI minus WRF-MPI). Below: absolute wind vectors in annual mean as in the WRF-MPI *(b)* and in the WRF-AWI *(c)* simulation.

Differences in the global simulations are generally larger: Regions with higher orography (FIS, the Alps and the Pyrenees) experience higher wind speeds in the EC6F simulation than in the MPI simulation. Apart from these regions, the wind speed is noticeably higher in the MPI simulation. Differences between the regional simulations are more zonally orientated. Over the northern (the FIS) and southern part of the simulated domain, wind speeds are lower in WRF-AWI. In between, the annual mean wind speeds are similar or, over the North Atlantic and the Alps, higher in WRF-AWI. For the regional simulations, the wind directions are investigated additionally. The absolute annual mean wind field and the associated differences are depicted in Fig. 4.18. Both simulations

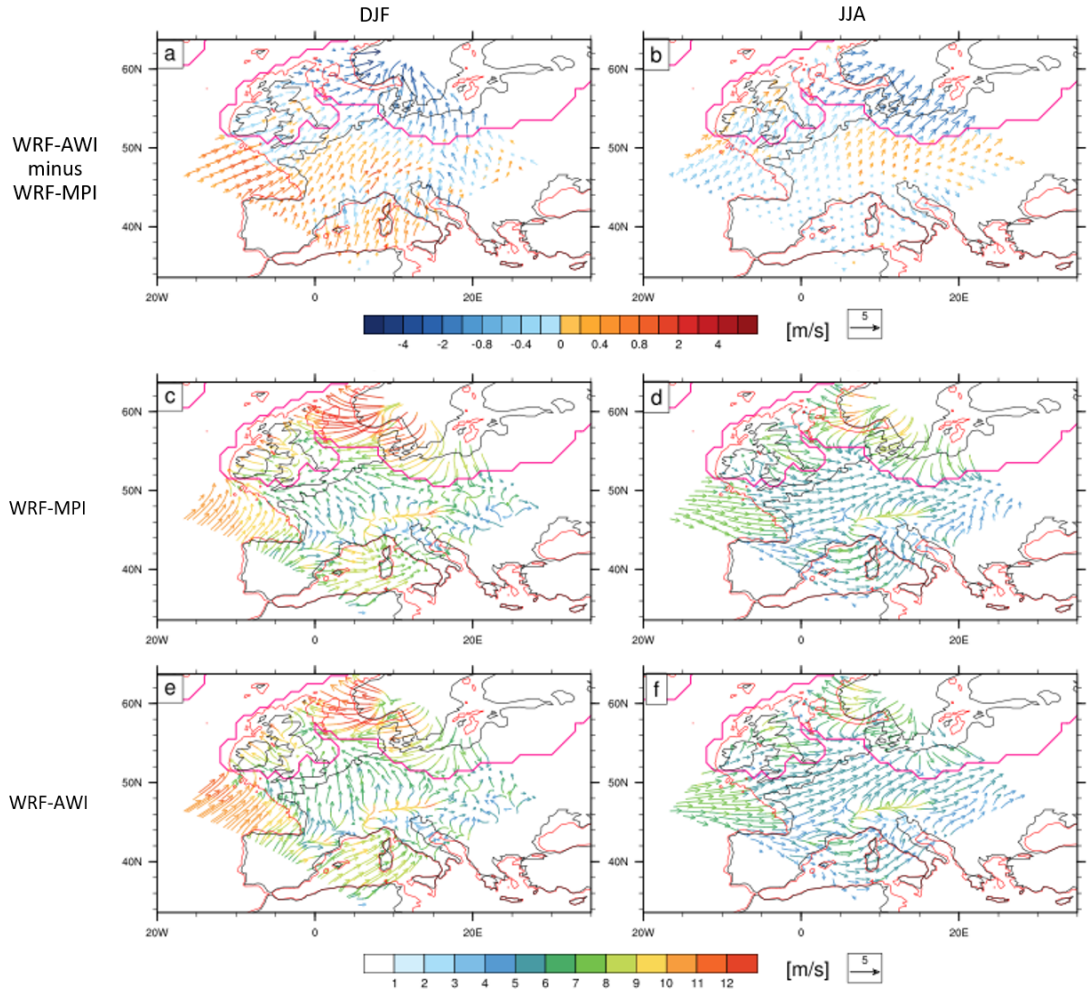

Figure 4.19: Distribution of the wind field in seasonal means for winter (left) and summer (right) (in m). *(a)* Differences of the winter wind field distribution between the regional climate model simulations (WRF-AWI minus (WRF-MPI). *(b)* as *(a)* but for summer wind. *(c)* Absolute values of the winter wind distribution in WRF-MPI. *(d)* as *(c)* but for the summer wind distribution in WRF-MPI. *(e)* and *(f)* as *(c)* and *(d)* but for the WRF-AWI wind distributions.

show strongest winds from the FIS southwards, although this pattern is notably more pronounced in WRF-MPI. In return, winds from the North Atlantic are stronger in WRF-AWI. Especially in winter, the direction of these winds is rather towards the domain centre in WRF-AWI, whereas winds in WRF-MPI point to the northwest outside of the domain (c.f. Fig. 4.19). In sumer, both WRF-MPI and WRF-AWI simulate westerly winds from the North Atlantic. Again, winds from

the FIS are blowing south- and southeastwards, but still the summer wind speeds are throughout weaker than in winter for both simulations.

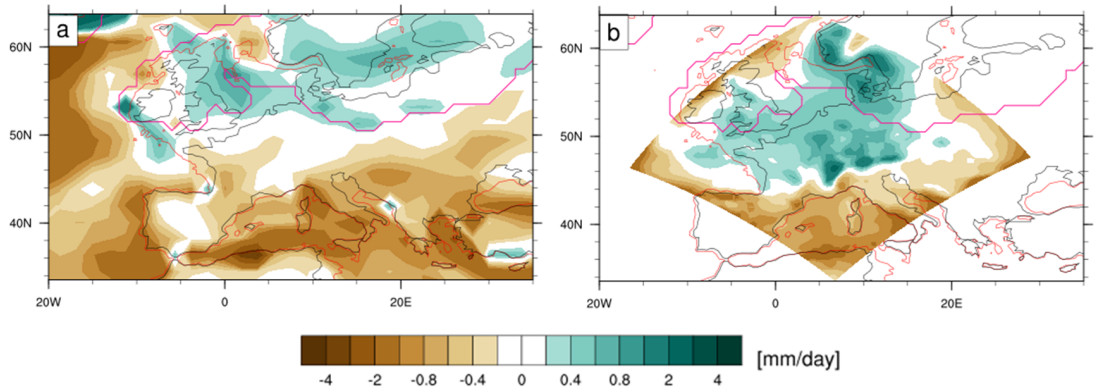

Figure 4.20: Distribution of the total precipitation in annual mean (in mm/day). *(a)* Differences of the precipitation distribution between the global climate model simulations (EC6F-LGM minus MPI-LGM). *(b)* Differences of the precipitation distribution between the regional climate model simulations (WRF-AWI minus WRF-MPI).

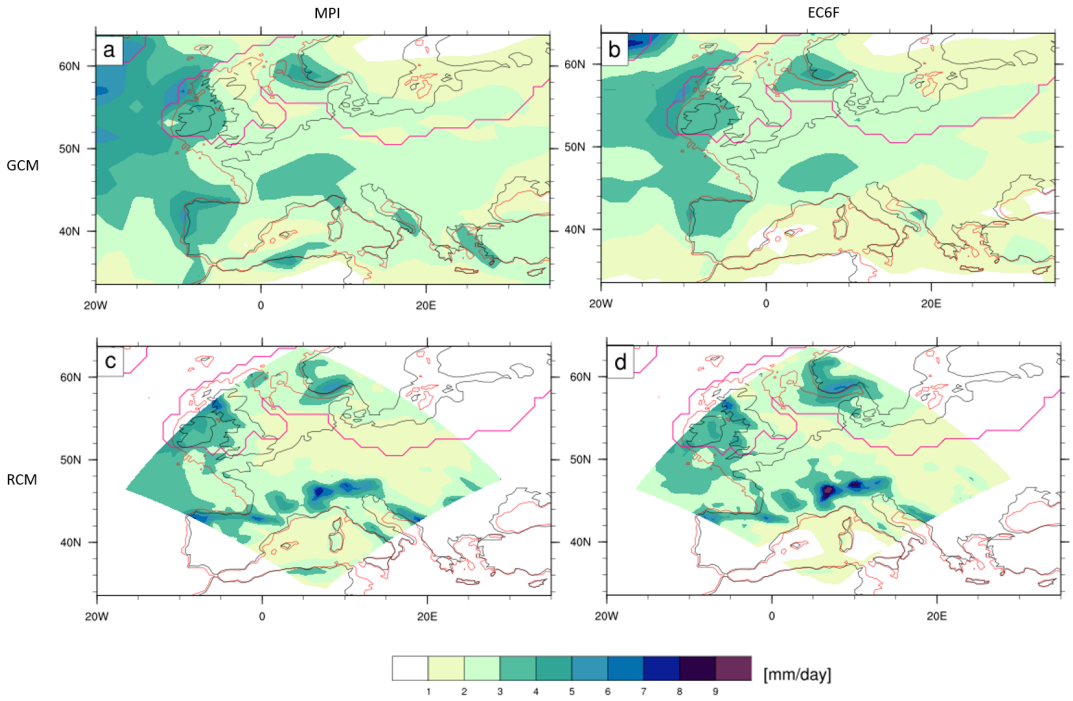

Figure 4.21: Distribution of the total precipitation in annual mean (in mm/day). Absolute values of the precipitation distribution as simulated by the global climate models MPI *(a)* and EC6F *(b)* and for the regional simulations WRF-MPI *(c)* and WRF-AWI *(d)*.

These wind fields are induced by the large-scale circulation in the global forcing simulations. There as well, northerly and easterly components are predominant in the MPI-LGM simulation, whereas southerly and westerly components occur more often in the EC6F-LGM simulation (c.f. Fig. 4.10). This is in accordance with the jet structure in both global simulations (c.f. Fig. 4.6) as already analysed in the previous section (c.f. Chap. 4.1). The MPI jet is deflected to the north, while the jet in the EC6F simulation reaches Southern Europe. As the influence of the ice sheet

is higher in the (global and regional) MPI simulations, their overall significant colder climate is consistent. Moreover, not only the smaller continental influence in the EC6F simulations warms their climate, but the westerly flow from the ice-free North Atlantic accounts for the increased heat and moisture transport. With the improved SSTs in the global EC6F simulation, the cooling of the LGM air temperatures is not as strong as proxies indicate (c.f. Tab. 4.2 and explanations in Chap. 4.1).

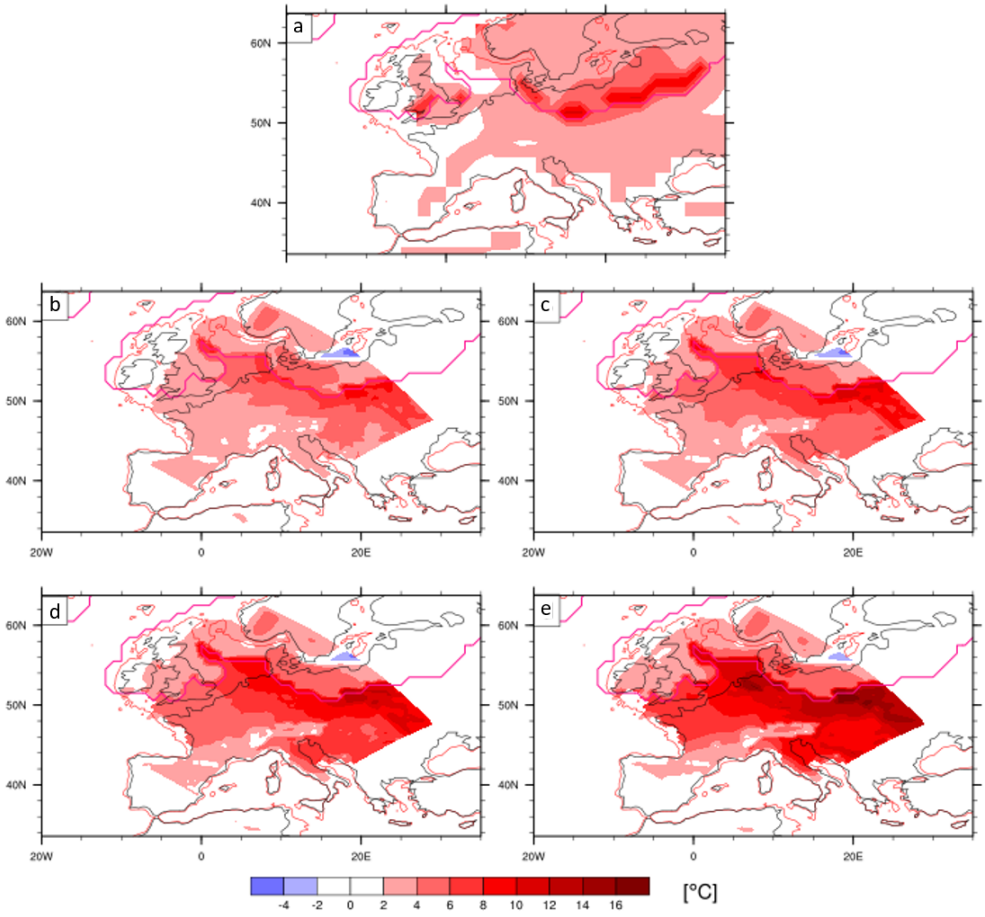

Figure 4.22: Distribution of the soil temperature in annual mean (in °C). *(a)* Differences of the soil temperature distribution in layer 3 (representative depth: 78 cm) between the global climate model simulations (EC6F minus MPI). *b) - e)* Differences of the soil temperature distribution between the regional climate model simulations (WRF-AWI minus WRF-MPI) in layer 1 with a representative depth of 5 cm *(b)*, in layer 2 with a representative depth of 25 cm *(c)*, in layer 3 with a representative depth of 70 cm *(d)*, and in layer 4 with a representative depth of 150 cm *(e)*.

Along with stronger winds from the North Atlantic, more moisture is transported and thus more precipitation is simulated over Europe in the WRF-AWI simulations (c.f. Fig. 4.20). This is not reflected by the global simulations, where precipitation patterns are relatively similar in Europe. In Southern and Central Europe, there is less precipitation in the global EC6F simulation than in the MPI simulation. Only over the ice sheets, precipitation in EC6F is enhanced. Highest precipitation amounts, however, are either orographically induced as for precipitation over the Alps and over the FIS or they are associated with the moisture availability of the North Atlantic (c.f. Fig. 4.21). These patterns are visible in the global simulations, but they are less accurate than in the regional simulations and the precipitation over the North Atlantic clearly dominates the distribution.

The structure of the soil is different in the global and regional models: In the global simulations, there are five soil layers implemented, reaching from 3 cm to almost 7 m. The regional simulations have four layers from a mid-layer depth of 5 cm to 150 cm. In the respective third layers, the most similar depth is represented, with 78 cm in the global and 70 cm in the regional simulations (c.f. Chap. 3). Here, the soil temperature and soil moisture will be examined.
On annual average, the differences between soil temperatures in the EC6F and MPI simulations do not vary much in the different depths. Therefore, only the third layer is depicted in Fig. 4.22 a. The differences amount to $2-4\,^{\circ}$C in Europe towards warmer soils in EC6F. Only at the ice sheet

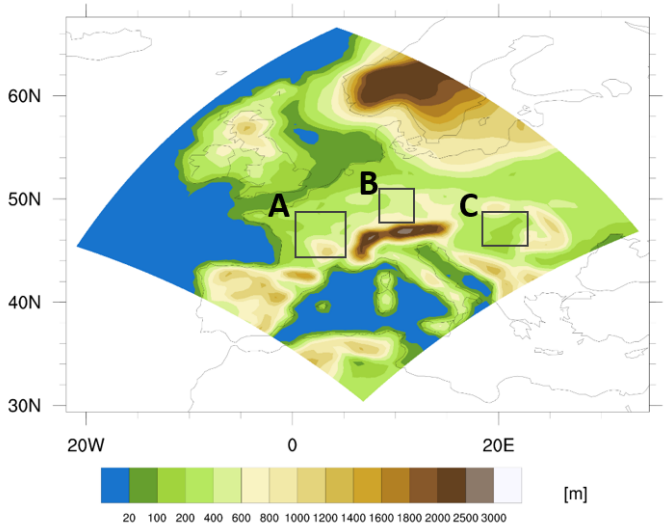

Figure 4.23: Domain 1 of the regional climate model simulations (c.f. Chap. 3), highlighted are three regions (A, B, and C) the following time series of soil temperature and soil moisture are referred to.

margins, these differences become greater. The differences between the two regional climate model simulations are somewhat altered. Again, the WRF-AWI simulation is warmer than the MPI driven simulation. However, the differences become larger with increasing depth. Where the differences in the first layer (representative depth of 5 cm) largely correspond to the distribution in the global simulations and also to the 2 m air temperature distribution due to the large influence of the atmosphere, the soil temperatures in the fourth layer (representative depth of 150 cm) diverge to a more than $15\,^{\circ}$C warmer soil in WRF-AWI.
Field means are calculated to investigate the development of the soil temperatures over time for three regions (c.f. Fig. 4.23). For the time series in Fig. 4.24, the whole 32 simulated years are taken into account, so that the spin-up phase can be regarded as well. The general pathway of the soil temperatures in the different layers are similar over time in all three regions, although region B is throughout colder than region A and C. Temperatures in the WRF-AWI simulation are higher almost everywhere and in neither of the two simulations, a trend over the 32 years is visible. The much smaller gradient into the depth in the WRF-AWI simulation is eye-catching, again in all three regions. In this simulation, temperatures vary only by about $2\,^{\circ}$C within the four layers

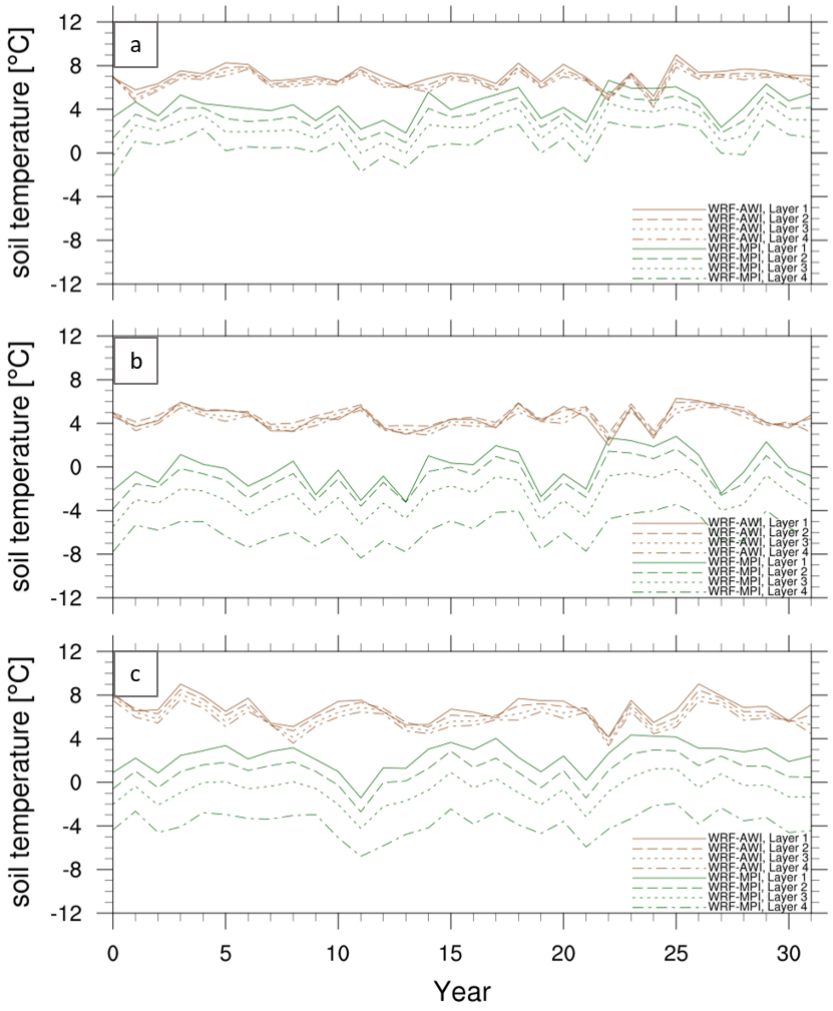

Figure 4.24: Development of the annual mean soil temperature in the regional climate model simulations (WRF-MPI: green, WRF-AWI: red), in region A of Fig. 4.23 *(a)*, region B *(b)*, and region C *(c)*, respectively over the 32 simulated years.

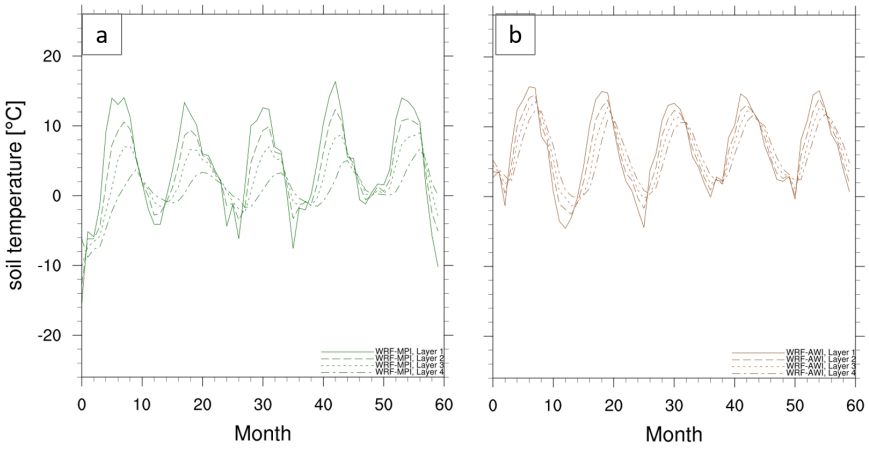

Figure 4.25: Development of the monthly mean soil temperature in the regional climate model simulations in region A over the first five simulated years. *(a)* WRF-MPI simulation, *(b)* WRF-AWI simulation.

and are almost similar at the time of the initialisation. In the WRF-MPI simulation, however, this gradient is much larger and explains thus the large temperature differences between the two simulations in the deepest soil layer. To take a closer look into the initialisation and spin-up phase, the monthly mean soil temperatures of the first five years are depicted (c.f. Fig. 4.25). Apart from the generally colder temperatures in region B, the behaviour of the soil temperatures in all three regions are very similar. Therefore, only the time series for region A is shown. The time series for the WRF-AWI soil temperatures show much less damping for the curves of the deeper layers than those of WRF-MPI. The amplitude for the seasonality in the upper layer is almost as high as in the depth and only a little shifted. The WRF-MPI temperatures show a more expected behaviour: Timing of the maximum temperature in each layer is lower in greater depths and occurs later in the year, since the signal of the atmosphere has to propagate downwards first. These different shapes of the soil temperature can explain the large differences in the deepest soil layer between the two regional simulations.

The annual mean soil moisture distribution differences between the WRF simulations are shown in Fig. 4.26. The upper three soil layers contain more water in the WRF-AWI simulation than in the WRF-MPI simulation. However, the opposite is the case in the fourth layer. This layer is much

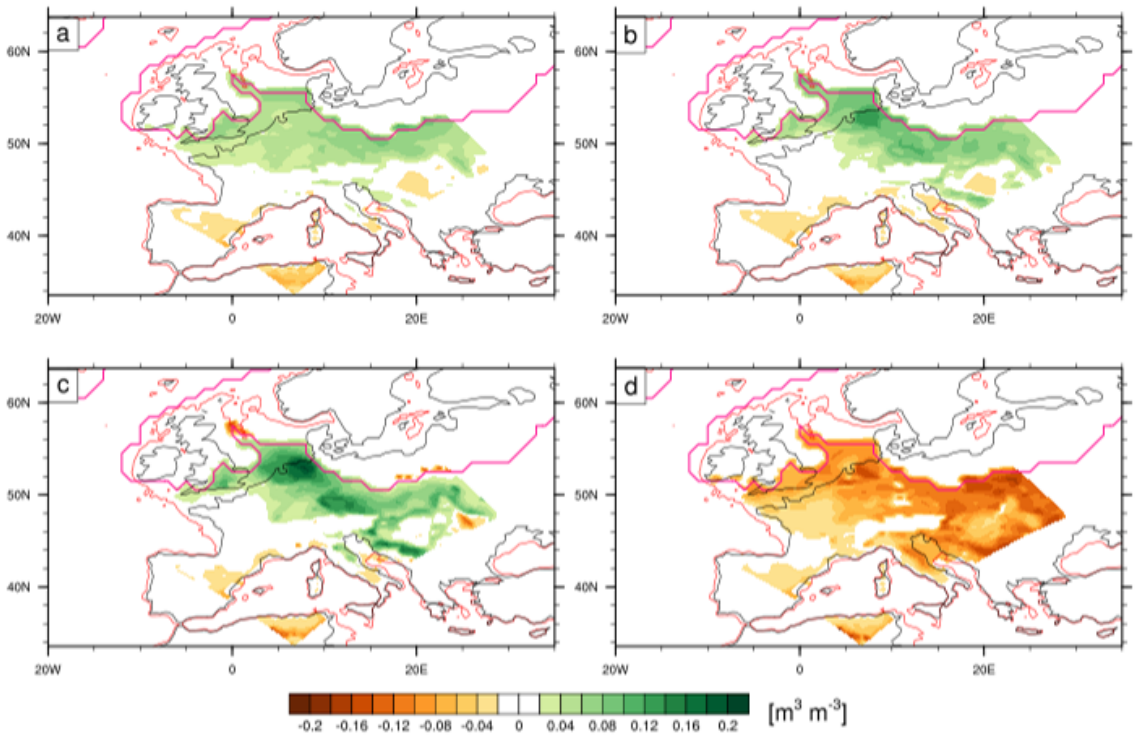

Figure 4.26: Distribution of the soil moisture content in annual mean (in m³/m³). Differences of the soil moisture distribution between the regional climate model simulations (WRF-AWI minus WRF-MPI) in layer 1 with a representative depth of 5 cm *(a)*, in layer 2 with a representative depth of 25 cm *(b)*, in layer 3 with a representative depth of 70 cm *(c)*, and in layer 4 with a representative depth of 150 cm *(d)*.

drier in WRF-AWI, especially in Northern and Eastern Europe south of the ice sheet margin. Time series of the soil moisture (c.f. Fig. 4.27) reveal that these differences arise from the WRF-MPI simulation, where the deepest soil layer contains exceptionally much water in comparison with the other layers and all layers in the WRF-AWI simulation. The soil moisture content rises quickly

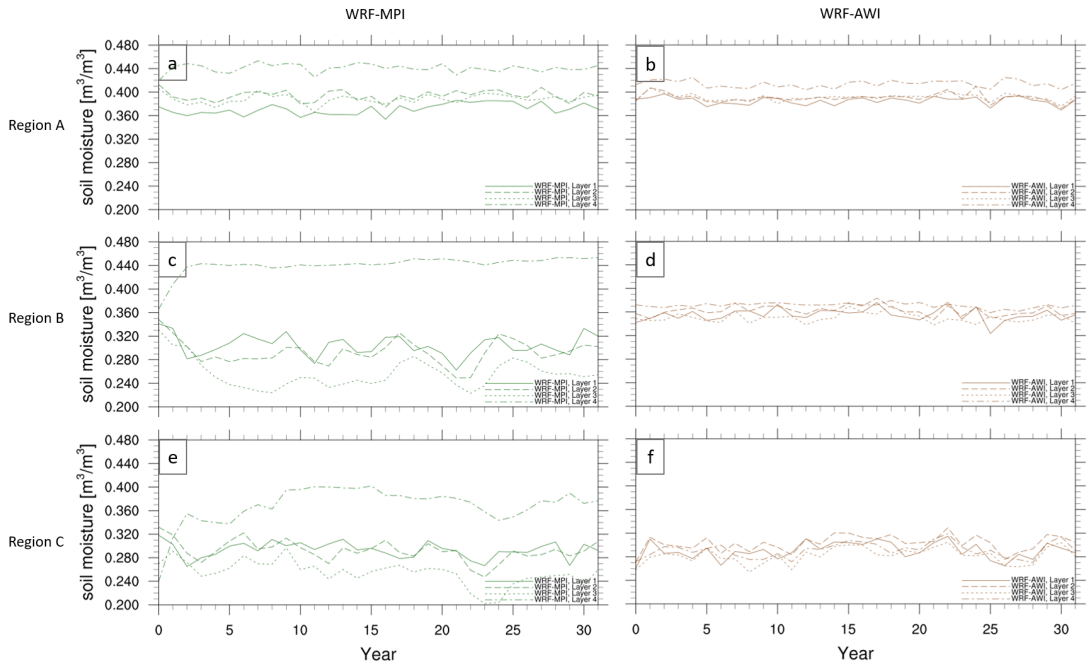

Figure 4.27: Development of the annual mean soil moisture content in the regional climate model simulations (WRF-MPI: green, left, WRF-AWI: red, right), in region A *(a)* and *(b)*, region B *(c)* and *(d)*, and region C *(e)* and *(f)* over the 32 simulated years.

in the first two years (and thus within the spin-up phase). After this rapid rise, changes are only marginal. This is particularly the case in region B, where a saturation of the soil moisture content is reached at the value of around 0.440 m³/m³ after these two years and then stays at this value. Even the monthly mean values of the soil moisture in 150 cm do not vary (c.f. Fig. 4.28).

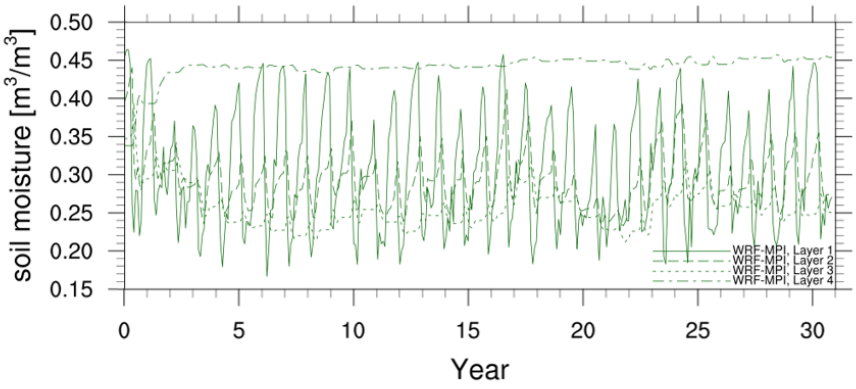

Figure 4.28: Development of the monthly mean soil moisture content in the WRF-MPI simulation in region B over the 32 simulated years.

The soil temperature time series can help to explain this behaviour. While WRF-MPI temperatures in the fourth layer remain markedly below 0 °C throughout the year in region B, they rise close to 0 °C in region C. Soil temperatures in region A, however, are above 0 °C most of the time. This implies that moisture is frozen and therefore bound in the fourth layer in region B, so that no exchange with the above layers occurs. In region C, the moisture is temporarily frozen and therefore partly decoupled from the other layers, whereas in region A, the soil moisture is transferred freely

between the layers.

These considerations directly lead on to the reconstruction of the permafrost extent based on these simulations, which will follow in the next section. Overall, the climate of the regional simulations corresponds to their respective global forcings. The WRF-AWI simulation results in higher temperatures due to a stronger influence from the North Atlantic with prevailing westerly winds. Still, adjustments from the global climate model simulations are found in the regional climate model runs, especially when it comes to the distributions of precipitation and snow height and cover.

4.3 Reconstruction of Permafrost during the Last Glacial Maximum

In this section, the reconstructions of permafrost based on climate model simulations will be presented. Three methods were applied for the reconstructions: MAAT, SFI, and the direct method based on mean annual soil temperatures. An overview of these and other possible methods is given in Chap. 2.2. To account for the recent findings of active sand wedges in seasonal frozen ground in contrast to the common assumption of their precondition of permafrost, criteria for the occurence of sand wedges are tested additionally.

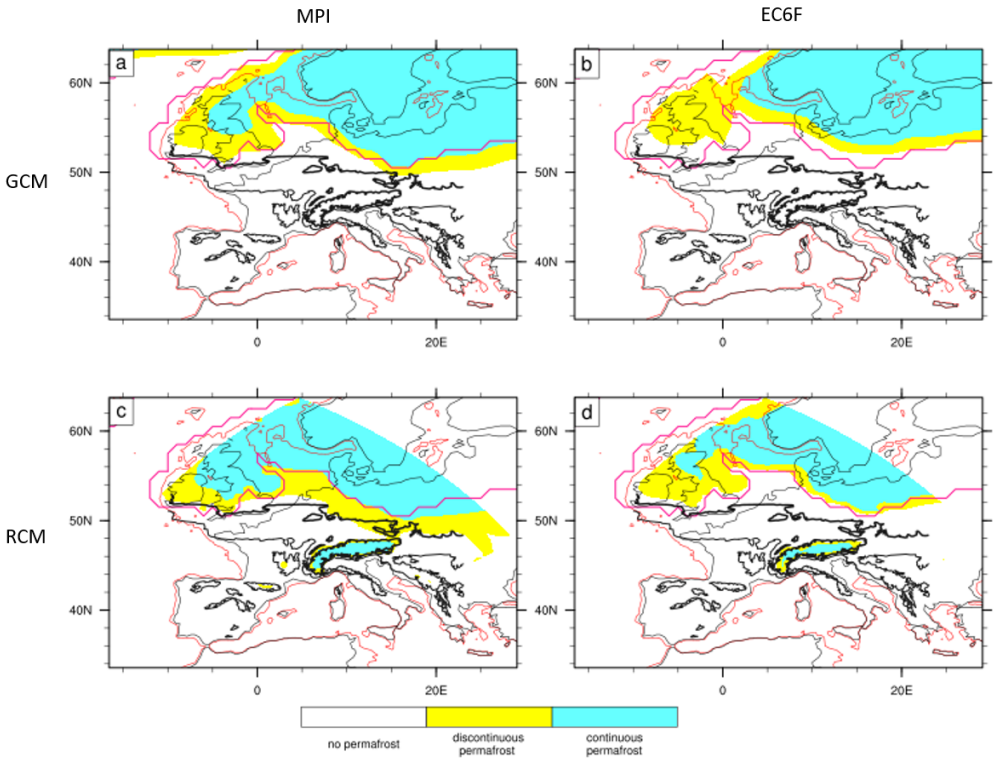

Figure 4.29: Permafrost distribution based on MAAT. *(a)* as in the global MPI simulation, *(b)* as in the global EC6F simulation, and *(c)* and *(d)* as in the respective regional simulations. Proxy-based permafrost extent is denoted by the thick black line for continuous permafrost and the thinner black line for discontinuous permafrost. Red lines denote the LGM coastlines, pink lines mark the ice sheet extent.

First, the most basic method was applied: The long-term mean annual air temperature (MAAT) was calculated for the 30 simulated years. Continuous permafrost is inferred where MAAT is below $-6\,^{\circ}\mathrm{C}$ and discontinuous permafrost for MAAT $\leq -2\,^{\circ}\mathrm{C}$ (c.f. Tab. 2.1). Results for this method are depicted in Fig. 4.29. Essentially, the hereby derived permafrost boundary corresponds to the ice sheet extent during the LGM for both the global and regional simulations. Permafrost in the EC6F and WRF-AWI simulations do not reach that far south and in the WRF-MPI simulation, permafrost is slightly more extented. The regional climate model simulations show some additional permafrost areas which are related to higher orography, especially at the Alps, and in WRF-MPI also at the Pyrenees and the Massif Central. These areas are not resolved in the global forcing simulations. Still, neither of the four simulations show an adequate permafrost extent based on MAAT.

The SFI was calculated based on daily mean values of the soil temperatures in all simulated layers. Results are only shown for the deeper layers (starting from 70 cm depth), since the upper two

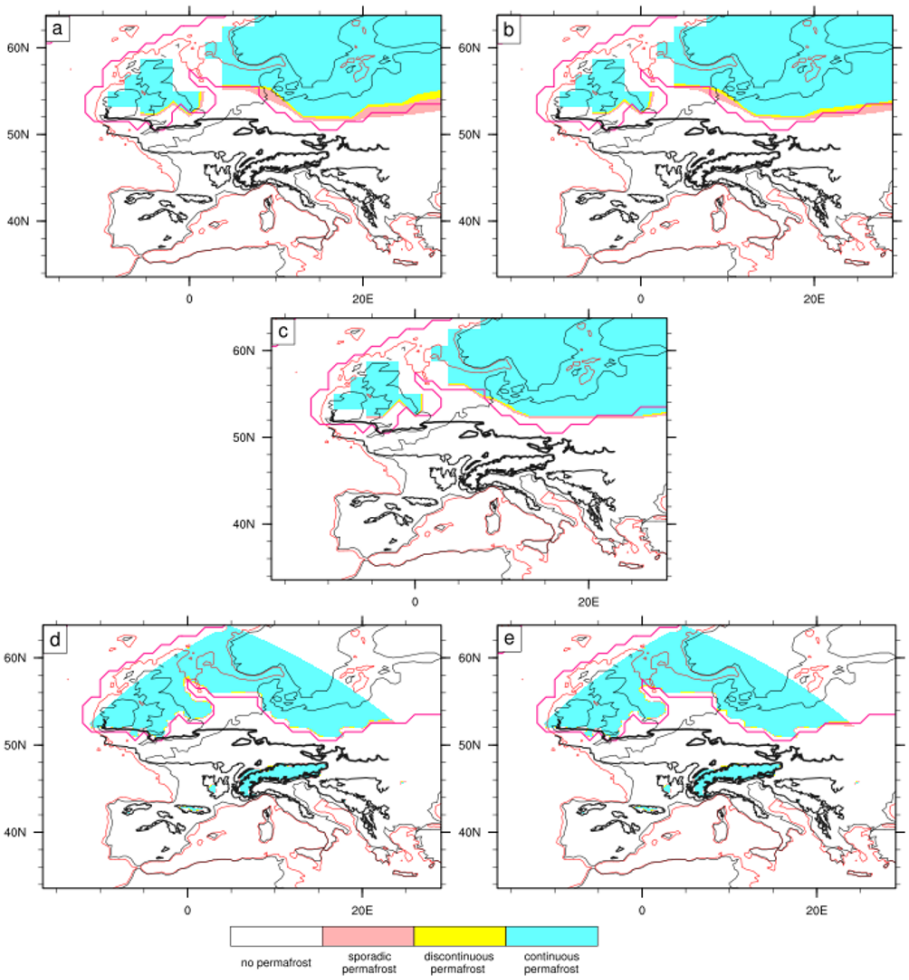

Figure 4.30: Permafrost distribution based on the SFI in the different soil layers. *(a)* Layer 3 of the global EC6F simulation (78 cm depth), *(b)* Layer 4 of the global EC6F simulation (268 cm), *(c)* Layer 5 of the global EC6F simulation (698 cm), *(d)* Layer 3 of the regional WRF-AWI simulation (70 cm) and *(e)* Layer 4 of the regional WRF-AWI simulation (150 cm). Proxy-based permafrost extent is denoted by the thick black line for continuous permafrost and the thinner black line for discontinuous permafrost. Red lines denote the LGM coastlines, pink lines mark the ice sheet extent.

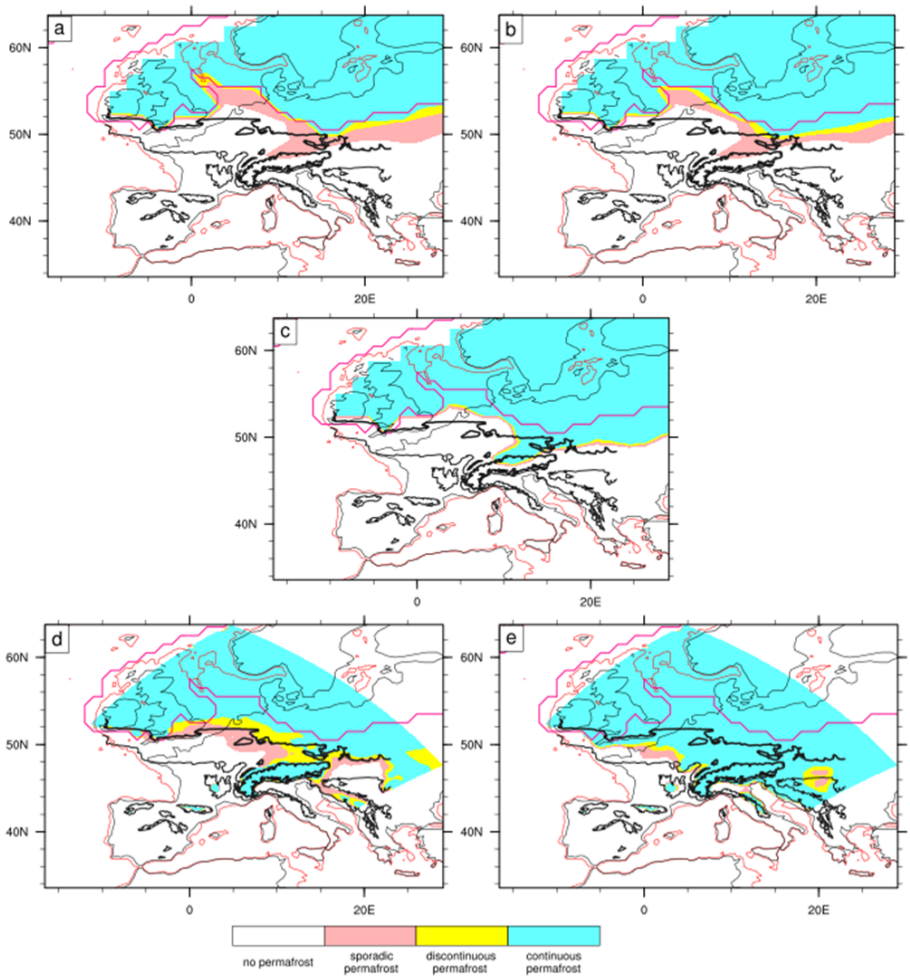

Figure 4.31: Permafrost distribution based on the SFI in the different soil layers as in Fig. 4.30 but for the MPI simulations. *(a)* Layer 3 of the global MPI simulation (78 cm depth), *(b)* Layer 4 of the global MPI simulation (268 cm), *(c)* Layer 5 of the global MPI simulation (698 cm), *(d)* Layer 3 of the regional WRF-MPI simulation (70 cm) and *(e)* Layer 4 of the regional WRF-MPI simulation (150 cm). Proxy-based permafrost extent is denoted by the thick black line for continuous permafrost and the thinner black line for discontinuous permafrost. Red lines denote the LGM coastlines, pink lines mark the ice sheet extent.

layers are possibly part of the active layer and thaw seasonally. The results are shown in Fig. 4.30 for the global and regional EC6F simulations and in Fig. 4.31 for the global and regional MPI simulations. Again, the permafrost extent in the EC6F simulations do not reach farther south than the ice sheet, apart from the Alps in WRF-AWI. A modest increase in the permafrost area is simulated by the global MPI simulation. Here continuous permafrost is still limited to the ice sheet in 78 cm and 268 cm depth, but sporadic permafrost is more widespread. According to this simulation, permafrost is either continuous or absent in the lowermost layer with a representative depth of 698 cm, but none of the other categories is found. The WRF-MPI simulation shows a larger permafrost extent. In Eastern Europe the proxy-based continuous permafrost extent is largely met in the third layer with a representative depth of 70 cm. In Western Europe, it is slightly too far north, which is overcorrected in the lowermost layer with a representative depth of 150 cm. Notable is further, that the conditions for discontinuous and sporadic permafrost are rarely fulfilled in all simulations.

The results of the direct method using long-term mean annual soil temperatures agree with the permafrost extent based on the SFI. It is examplarily depicted for the MPI simulations in Fig. 4.32. With these methods, the different types of permafrost cannot be distinguished. That is why the

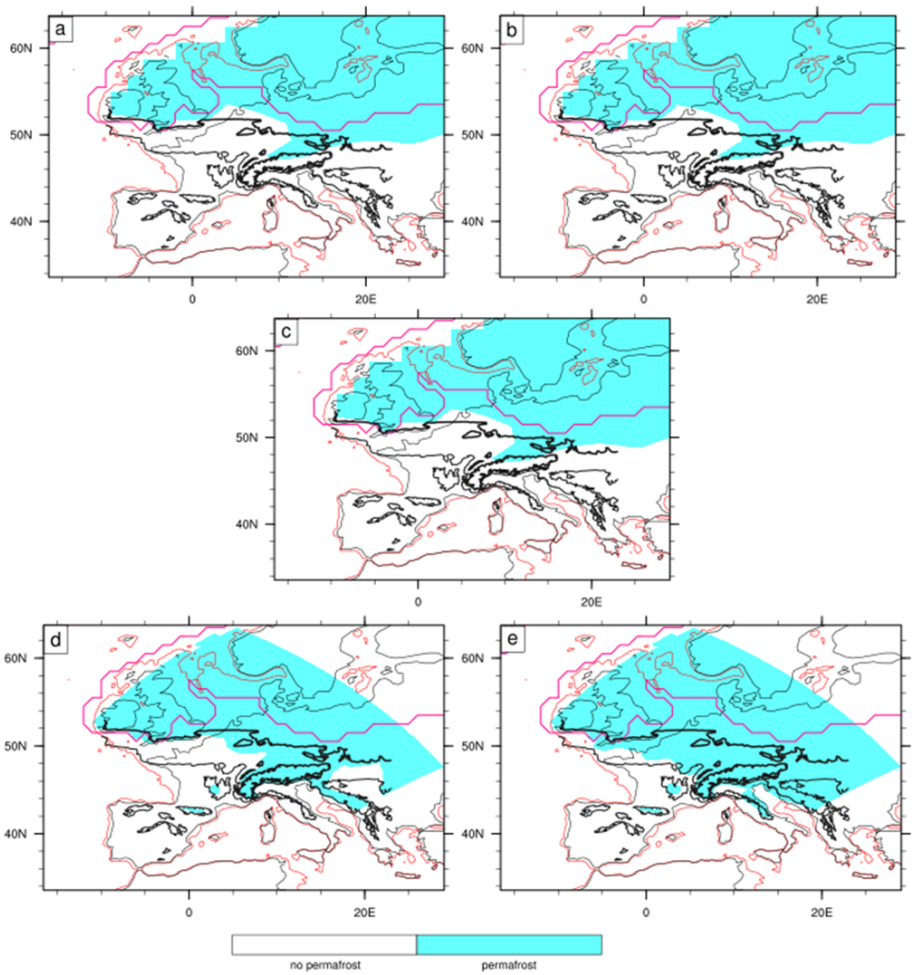

Figure 4.32: Permafrost distribution based on the soil temperatures below 0 °C in the different soil layers for the MPI simulations. *(a)* Layer 3 of the global MPI simulation (78 cm depth), *(b)* Layer 4 of the global MPI simulation (268 cm), *(c)* Layer 5 of the global MPI simulation (698 cm), *(d)* Layer 3 of the regional WRF-MPI simulation (70 cm) and *(e)* Layer 4 of the regional WRF-MPI simulation (150 cm). Proxy-based permafrost extent is denoted by the thick black line for continuous permafrost and the thinner black line for discontinuous permafrost. Red lines denote the LGM coastlines, pink lines mark the ice sheet extent.

permafrost line based on the direct method corresponds to that of the sporadic permafrost based on the SFI.

The proxy-based permafrost extent is used as a reference to compare the model output with. However, it was pointed out in Chap. 2.2 that this reconstruction is fraught with uncertainty as well. Ice and sand wedges usually serve as a proxy for past permafrost, but they may also develop within seasonal frozen ground and not exclusively within permafrost. Several authors derived criteria that have to be fulfilled for thermal contraction cracking to be possible (c.f. Matsuoka et al. 2018; Wolfe et al. 2018), which is a part of the development of ice and sand wedges. After Matsuoka et al. (2018), thermal contraction cracking may occur when the daily mean soil temperature at a depth of 1 m is lower than $-5\,^{\circ}\mathrm{C}$ at the same time when the gradient between the daily mean soil

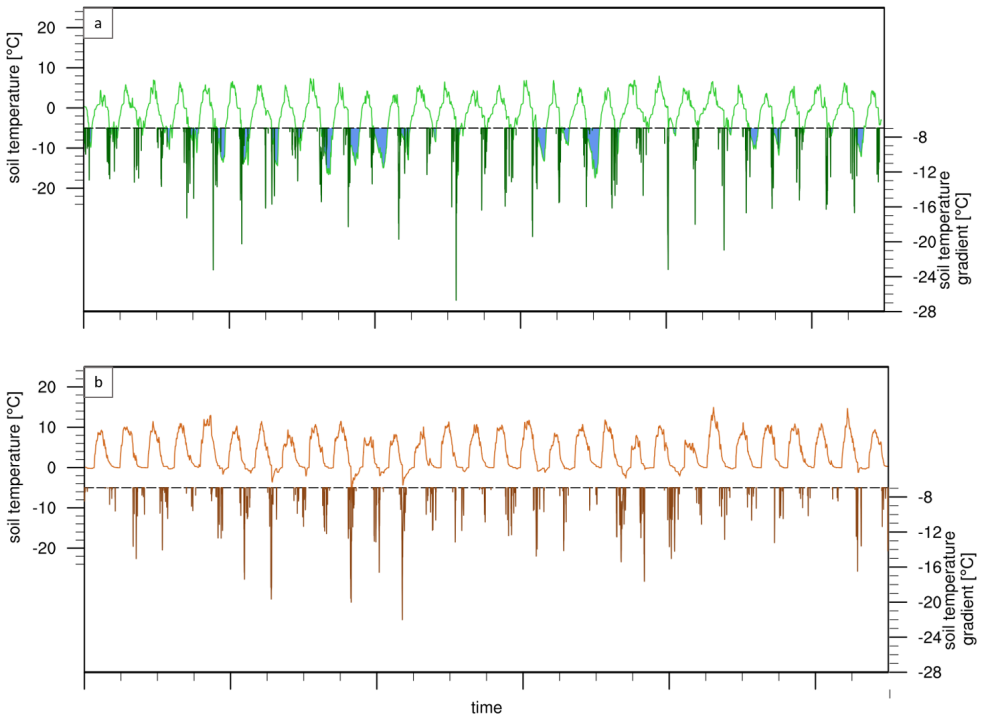

Figure 4.33: Development of the daily mean soil temperatures and soil temperature gradient in region C of Fig. 2.7 b (model grid point 45.1° N, 0.27° E) as simulated in WRF-MPI *(a)* and in WRF-AWI *(b)*. Lighter colors show the development of the soil temperatures in layer 3 (70 cm). When the temperatures fall below −5 °C, the first condition after Matsuoka et al. (2018) is fulfilled, marked with blue shading and the reference line. The soil temperature gradient between the first layer (5 cm depth) and the third layer (darker colors) is only depicted, when condition two after Matsuoka et al. (2018) is fulfilled, with a gradient below −7 °C.

temperature in 0.02 m depth and in 1 m depth is lower than −7 °C. These criteria were applied to the climate model output. Instead of the soil temperature at 1 m, the temperature of the third layer with a depth of 78 cm in the global climate model simulations and 70 cm in the regional simulations was taken into account.

Fig. 4.33 shows an example of how the soil temperature and the gradient develop over time in Northern Aquitaine (region C in Fig. 2.7 b). The two criteria are fulfilled when the curves reach below the depicted reference line. In the WRF-MPI simulation (Fig. 4.33 a), this is the case in several winters, but not in the WRF-AWI simulation.
The number of days per year when thermal contraction cracking based on the Matsuoka criteria (Matsuoka et al. 2018) is counted for each grid cell and translated into heat maps for each simulation. The results are shown in Fig. 4.34. Whereas the permafrost area is much too small in both global simulations, the opposite is the case for possible thermal contraction cracking sites in the global MPI simulation. According to this simulation, thermal contraction cracking would have been possible as far south as the Iberian Peninsula, where no ice or sand wedge pseudomorphs were found. In Northern Europe, the criteria are fulfilled more than 30 times per year. In the global EC6F simulation, the criteria are less often fulfilled. Especially the southern edge of sand wedge occurence is only slightly underestimated.

The criteria are less often fulfilled in both regional simulations than their respective global counterparts. The southern limit for possible contraction cracking is farther north.

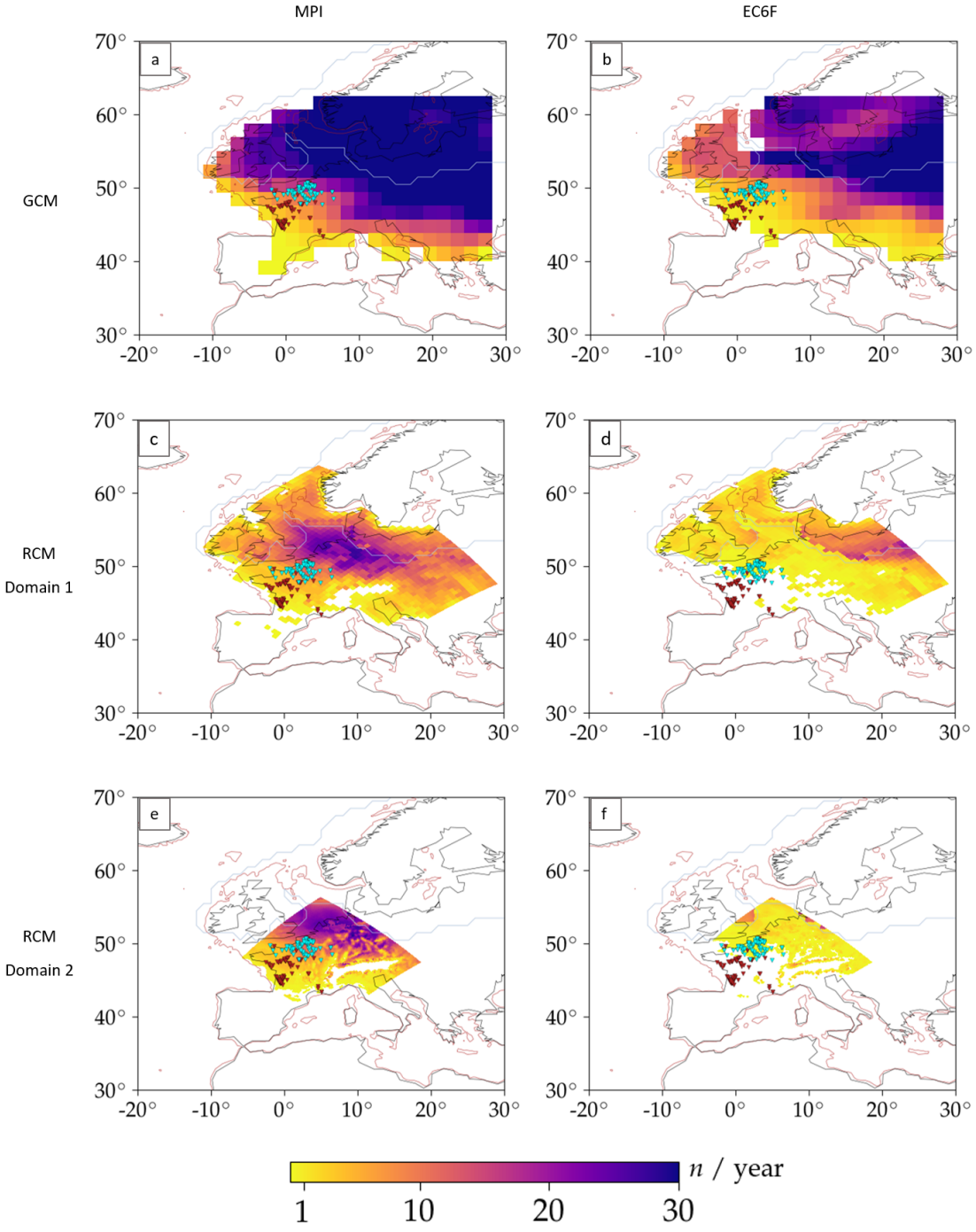

Figure 4.34: Heat maps of the mean number of days per year when the conditions after Matsuoka et al. (2018) are fulfilled for each grid box in the global MPI *(a)* and EC6F simulations *(b)*, and for the first domain of the regional WRF-MPI *(c)* and WRF-AWI *(d)* simulations, as well as for the second domain in WRF-MPI *(e)* and in WRF-AWI *(f)*. Ice-wedge pseudomorphs and sand wedges from Isarin et al. (1998) are highlighted with cyan and red triangles, respectively, only when located in France. Red lines denote the LGM coastlines, gray lines mark the ice sheet extent.

5 Discussion

In the following, the ability of the different methods to reconstruct permafrost and thermal contraction cracking regions from climate model data will be discussed. Afterwards, the results of the different simulations will be put into context.

Both indirect methods to infer permafrost out of climate model data, MAAT and SFI, are derived from conditions at locations with present-day permafrost. The condtions, however, may have been different in the past (e.g. Murton and Kolstrup 2003; Vandenberghe et al. 2014). And even for today, the air temperature varies between permafrost sites, which increases the uncertainty for MAAT (Vandenberghe et al. 2014). Because of the permafrost definition, it seems intuitive to broadly relate the 0 °C annual air temperature isotherm to the permafrost boundary (c.f. Huissteden 2020). Yet, this relationship is more complex. Vegetation or snow cover act as "thermal offsets"(Murton and Kolstrup 2003) that modulate the mean annual ground temperature in comparison to the air temperature and thus its relation to permafrost occurence (c.f. Ballantyne 2017; Huissteden 2020). Additionally, permafrost proxies such as ice-wedge pseudomorphs react stronger to extremes than to climatic averages. To reduce the occurence of the proxies to one parameter like MAAT might therefore be inaccurate (c.f. Ballantyne 2017; Matsuoka et al. 2018). The results of this study support these caveats. In each of the considered simulations, the MAAT-based permafrost boundary corresponds to the ice sheet margin and it is therefore obvious, that MAAT does not indicate a reasonable magnitude of the permafrost extent during the LGM.

This is different when considering the SFI. At least for the MPI simulations, the SFI-based permafrost boundary is located farther south and thus closer to the permafrost extent derived from proxy data. Moreover, the SFI method is supported by the direct method. The boundaries between permafrost occurence and absence as indicated by the SFI fully match the permafrost border derived from the mean annual ground temperature at the respective layers. However, discontinuous and sporadic permafrost is only rarely found with the SFI. These zones are very narrow, which does not reflect the widespread occurence that proxies indicate. Vandenberghe et al. (2014) observed this limitation as well and suggested its origin in the greater temperature gradients during the LGM than today.

Both MAAT and SFI require long-term mean values and it is well established to search for equilibrium permafrost, meaning a permafrost extent that corresponds to the climatic mean state of the studied period. To agree with the permafrost definition, soil temperatures have to be below 0 °C for only two years at a minimum. Furthermore, the proxy-based permafrost extent might reflect very cold but only short periods as mentioned before, that can therefore not be reproduced with methods using long-term mean values.

In addition to the permafrost extent, possible proxy locations were searched in the simulations. Therefore, the criteria for thermal contraction cracking by Matsuoka et al. (2018), derived from fieldwork in Svalbard, were applied to climate model data for the first time. Overall, the results

are promising: Thermal contraction cracking is possible in each simulation. The southernmost cracking locations are farther south than the respective reconstructed permafrost extent. This is to expect, since ground cracking occurs within seasonal frozen ground as well as within permafrost. Nevertheless, the present study can only provide a first impression of this method. Further validations should be performed, testing other regions, time periods in the past and present-day ground cracking sites additionally.

The permafrost reconstructions based on the simulations considered in this study underpin again limitations of the global climate models to represent permafrost during the LGM (c.f. Chap. 1). The global MPI simulation does not reach as far south as to expect from proxy evidence, but especially the global EC6F simulation fail to reproduce the permafrost extent in Europe during the LGM. Temperatures during the LGM are generally warmer in this latter simulation and conditions are more humid, as the influence from the North Atlantic is exerted via strong westerly winds. This is less in agreement with proxy evidence, even though the climate under PI conditions is correctly reproduced (c.f. Chap. 4.1).

The EC6F-driven regional simulation exhibit a similar large-scale circulation and an even warmer version of the LGM. The permafrost extent is equally limited to the ice sheet and there is thus no improvement towards its global counterpart in this regard. Permafrost extent in the WRF-MPI simulation, however, is in much more agreement with the proxy-based permafrost reconstruction. In 70 cm depth, the continuous permafrost boundary is reproduced accurately in Eastern Europe and still close in the west. Since uncertainties arise from both model and proxy side, a perfect match is not expected.

Whereas both global climate model simulations indicate less permafrost than their regional counterpart, the global MPI simulation yields a much larger extent to the south for possible ground cracking. In the global MPI simulation, the criteria after Matsuoka et al. (2018) are fulfilled more than 30 times a year in Northern Europe and at a smaller number even on the Iberian Peninsula, where no ice or sand wedges were found. Also in the warmer EC6F simulation, ground cracking occurs in mid- to Southern France. As for the permafrost extent, also the possible thermal contraction cracking occurence is poorly represented in WRF-AWI. At locations, where ice-wedge pseudomorphs or sand wedges are found, the criteria are not fulfilled during the simulated days. By contrast, the WRF-MPI simulation agrees well with the proxy evidence. Apart from two sand wedges southwest of the Alps, thermal contraction cracking is possible in the simulation, where the features are found. This is improved in the nested domain.

Taking both permafrost and ground cracking locations into account, the MPI simulations, in particular the regional WRF-MPI simulation, are more in agreement with proxy evidences. In the global EC6F simulation, ground cracking locations are reasonably reproduced, but the permafrost does not extent farther south than the ice sheet margin. The regional WRF-AWI simulation indicates no permafrost (except for regions under the ice sheet) and can not explain the ice-wedge pseudomorphs and sand wedges that are found in France. For the global MPI simulation, the permafrost line is too far north, whereas ground cracking is possible too far south in comparison with proxy data. For WRF-MPI, both permafrost extent and possible ground cracking regions are largely in agreement with proxy evidence.

The main difference between the two global models is the applied ocean model, which leads to different LGM climate conditions and differences in the atmospheric flow. In the EC6F simulation the

westerly flow dominates so that moisture and heat is transported from the North Atlantic towards Europe. This large-scale circulation agrees more with the multi-model mean of the CMIP5/PMIP3 models, while the MPI simulation suggests a stronger influence of the ice sheet through prevailing north- and northeasterly winds. It was found that the global MPI simulation agrees better with proxy evidences regarding temperature and precipitation differences under LGM and PI conditions and that the permafrost and ground cracking extent is reproduced reasonably well in the MPI-driven regional simulation. It is thus plausible to assume that the large-scale circulation of the MPI simulations reflect that of the LGM accurately. This is in line with recent studies (e.g. Raible et al. 2020; Schaffernicht et al. 2020). So far only indirect proxy evidences for wind and air pressure exist. One is the loess belt at around 40° N and 60° N in Central Europe that can provide indications. Because of the drier conditions with less vegetation and higher wind speeds, dust and dust storms were more common during the LGM than today (c.f. Chap. 2). This is reflected in many loess deposits in Western and Central Europe, which form the European less belt (e.g. Lehmkuhl et al. 2016). Recent studies on the dust cycle supported the hypothesis that easterly winds induced by a semi-permanent anticyclone over the Fennoscandian Ice Sheet (FIS) dominated the dust transport and thus the formation of the loess belt (e.g. Raible et al. 2020; Schaffernicht et al. 2020; Stevens et al. 2020 and references therein).

The aim of the present study was to investigate the general ability of regional climate models to represent the permafrost distribution in Western Europe during the LGM. With a realistic global forcing, especially regarding the large-scale atmospheric flow, it can be shown that the regional climate model WRF provides an added value compared to the global counterpart. Due to large uncertainties in the permafrost reconstruction from both climate model and proxy side, not only permafrost indices were tested, but also the possibility of ice and sand wedges to develop. Large differences between the permafrost extent and the areas, where sand and ice wedges can develop, were found both in the climate model data as well as in the fields. This demonstrates once more that sand and ice wedges do not exclusively grow within continuous permafrost, but also, as indicated by Andrieux et al. (2018), within seasonal frozen ground, when the winter temperatures are very cold.

6 Conclusion

Permafrost is an important component of the climate system. Thawing of permafrost is associated with the release of greenhouse gases that were previously bound within the frozen soils. Thereby, the greenhouse effect is enhanced which leads to further warming of the climate (c.f. IPCC 2019). This positive feedback mechanism is the main reason, why it is important to gain knowledge about future thawing of permafrost and about the amount of related greenhouse gas emissions.

Current climate model simulations project a large range of uncertainty regarding the decrease of permafrost area, that is only partly related to internal variabilities. The models are calibrated for present-day conditions, under which they are well tested. However, the responses of the models to the same forcings vary by several orders of magnitude (c.f. IPCC 2013; IPCC 2019). It is therefore necessary to evaluate the climate models under a larger range of climate variability, which can be realised by simulating the past and compare the outcomes to proxy evidence. The present study focused on the LGM, a cold and dry period of the last glacial cycle 26.5 to 19 thousand years ago (c.f. Clark et al. 2009). At this time, permafrost was more widespread and reached France in Europe. Studies investigating permafrost during the LGM with global climate models found only a limited ability of the models to represent the permafrost extent (e.g. Kitover et al. 2013; Levavasseur et al. 2011; Ludwig et al. 2017). But there are evidences for improvement when using regional climate model simulations instead (c.f. Ludwig et al. 2017). This was investigated further in the present study.

Therefore, two regional climate model simulations were conducted with the WRF model, using the same set-up but two different global climate model simulations as forcings. Namely, these are the well established MPI-ESM-P (Stevens et al. 2013) and the relatively new global climate model ECHAM6-FESOM developed at the Alfred Wegener Institute (Sidorenko et al. 2015). They share the same atmospheric, land, and biochemistry components, solely the ocean component varies. On the one hand, this leads to different SST patterns towards a colder North Atlantic and a warmer Arctic Ocean in the EC6F simulation. On the other hand, the atmospheric characteristics differ. European 2 m air temperatures are higher in the EC6F simulation. This can be associated with the large-scale atmospheric flow. The jet in the EC6F simulation approaches Europe at the latitude of France and the Iberian Peninsula in line with the prevailing westerly winds that transport heat and moisture towards Europe. The jet in the MPI simulation, in contrast, is more narrow and deflected to the north. North and northeasterly winds are more common, promoting a colder and drier climate in Europe.

These major differences are reflected and slightly greater between the regional climate model simulations. The 2 m air and soil temperatures are warmer in the WRF-AWI simulation, particularly near the ice sheet margin. The different main wind directions correspond to their respective counterpart with easterly and northeasterly winds in the WRF-MPI and westerly winds in the WRF-AWI simulation.

As the climate of these global and regional climate model simulations differ considerably from each other, so do the reconstructions of permafrost and thermal contraction cracking areas. In the global and regional EC6F simulations, permafrost in Europe does not extent farther south than the ice sheet margin, which is not plausible. Possible ground cracking regions agree with proxy evidence in the global EC6F simulation and is again too far north in the regional WRF-AWI simulation. Permafrost in the global MPI simulation reaches only marginally farther south than the ice sheet edge. In contrast, thermal contraction cracking of the ground is possible as far south as the Iberian Peninsula according to this simulation. The WRF-MPI simulation agrees fairly well with proxy evidence regarding both the permafrost extent and the possible ground cracking regions.
From these results, the following main conclusions can be drawn:

- With a reasonable forcing, regional climate models are able to represent ground and atmospheric characteristics under LGM conditions.
- In this case, an added value of the regional climate model simulations over their global counterparts can be found regarding the permafrost extent and possible ground cracking regions, when comparing to proxy evidence.
- The clear result in favour of the regional WRF-MPI simulation suggests that its implemented atmospheric circulation reflects the conditions during the LGM accurately, and it is thus hypothesized that easterly and northeasterly winds are more common during the LGM than today.
- The climate model data are in agreement with the assumption that ice and sand wedge development is not exclusive to regions of continuous permafrost, but may also happen in areas of only seasonally frozen ground.

A Abbreviations

EC6F ECHAM6-FESOM

AWI Alfred Wegener Institute

CMIP Coupled Model Intercomparison Project

CWT Circulation Weather Type

ECMWF European Centre for Medium-Range Weather Forecasts

F Air Frost Number

FESOM Finite Element Sea ice-Ocean Model

FI Freezing Index

FIS Fennoscandian Ice Sheet

GCM Global Climate Model

IPCC Intergovernmental Panel on Climate Change

ITCZ Intertropical Convergence Zone

LGM Last Glacial Maximum

LPM Last Permafrost Maximum

LIS Laurentide Ice Sheet

MAAT mean annual air temperature

MAGT mean annual ground temperature

MPI-ESM Max-Planck-Institute Earth System Model

MPI-M Max-Planck-Institute for Meteorology

OASIS Ocean Atmosphere Sea Ice Soil

PI Pre-Industrial

PMIP Paleoclimate Modelling Intercomparison Project

RCM Regional Climate Model

SFI Surface Frost Number

SIC sea ice fraction

SST sea surface temperature

TI Thawing Index

UNEP United Nations Environment Programme

WPS WRF Preprocessing System

WRF Weather Research and Forecast

WSF WRF Software Framework

B WRF namelist

```
#                           MPI-ESM       EC6F variational settings
&time_control
run_days                  = 0,
run_hours                 = 0,
run_minutes               = 0,
run_seconds               = 0,
start_year                = 1918, 1918,   E6-F: 3900, 3900,
start_month               = 01,   01,
start_day                 = 01,   01,     E6-F: 02,   02,
start_hour                = 00,   00,
start_minute              = 00,   00,
start_second              = 00,   00,
end_year                  = 1949, 1949,   E6-F: 3933, 3933,
end_month                 = 12,   12,     E6-F: 01,   01,
end_day                   = 30,   30,     E6-F: 01,   01,
end_hour                  = 18,   18,     E6-F: 00,   00,
end_minute                = 00,   00,
end_second                = 00,   00,
interval_seconds          = 21600
input_from_file           = .true.,.true.,
history_interval          = 360,  360,
frames_per_outfile        = 1, 1,
restart                   = .false.,
restart_interval_d        = 10,
io_form_history           = 2
io_form_restart           = 2
io_form_input             = 2
io_form_boundary          = 2
debug_level               = 1
io_form_auxinput4         = 2,
auxinput4_inname          = "wrflowinp_d<domain>",
auxinput4_interval        = 360, 360,
output_diagnostics        = 1,
auxhist3_outname          = "wrfclim_d<domain>_<date>",
auxhist3_interval         = 1440,1440,
frames_per_auxhist3       = 1, 1,
```

```
io_form_auxhist3           = 2,
force_use_old_data         = .true.,
/

&domains
time_step                  = 240,
time_step_fract_num        = 0,
time_step_fract_den        = 1,
max_dom                    = 2,
e_we                       = 60,    121,
e_sn                       = 60,    121,
e_vert                     = 35,     35,
p_top_requested            = 15000,
num_metgrid_levels         = 31,           E6-F: 18,
num_metgrid_soil_levels    = 5,
dx                         = 50000.00, 12500.00,
dy                         = 50000.00, 12500.00,
grid_id                    = 1,     2,
parent_id                  = 0,     1,
i_parent_start             = 1,     17,
j_parent_start             = 1,     13,
parent_grid_ratio          = 1,     4,
parent_time_step_ratio     = 1,     5,
feedback                   = 0,
smooth_option              = 0
/

&physics
mp_physics                 = 4,     4,
ra_lw_physics              = 4,     4,
ra_sw_physics              = 4,     4,
radt                       = 30,    30,
sf_sfclay_physics          = 1,     1,
sf_surface_physics         = 2,     2,
bl_pbl_physics             = 1,     1,
bldt                       = 0,     0,
cu_physics                 = 1,     1,
cudt                       = 5,     5,
prec_acc_dt                = 360,   360,
vmax_10m_dt                = 360,   360
num_land_cat               = 24
isfflx                     = 1,
ua_phys                    = .true.,
```

```
ifsnow                              = 1,
icloud                              = 1,
surface_input_source                = 1,
num_soil_layers                     = 4,
sf_urban_physics                    = 0,     0,
sst_update                          = 1,
sst_skin                            = 1,
rdmaxalb                            = .false,
tmn_update                          = 1,
usemonalb                           = .false.,
fractional_seaice                   = 1,
seaice_threshold                    = 0,
/

&fdda
/

&dynamics
w_damping                           = 1,
diff_opt                            = 1,      1,
km_opt                              = 4,      4,
diff_6th_opt                        = 2,      0,
diff_6th_factor                     = 0.12,   0.12,
base_temp                           = 290.
damp_opt                            = 3,
zdamp                               = 5000.,  5000.,
dampcoef                            = 0.2,    0.2,
khdif                               = 0,      0,
kvdif                               = 0,      0,
epssm                               = 0.7,    0.7,
non_hydrostatic                     = .true., .true.,
moist_adv_opt                       = 1,      1,
scalar_adv_opt                      = 1,      1,
tke_adv_opt                         = 1,      1,
use_theta_m                         = 0,
/

&bdy_control
spec_bdy_width                      = 5,
spec_zone                           = 1,
relax_zone                          = 4,
specified                           = .true., .false.,
nested                              = .false., .true.,
```

```
spec_exp                    = 0.33
/

&grib2
/

&namelist_quilt
nio_tasks_per_group         = 0,
nio_groups                  = 1,
/
```

Bibliography

Andrieux, E., M. D. Bateman, and P. Bertran (2018). "The chronology of Late Pleistocene thermal contraction cracking derived from sand wedge OSL dating in central and southern France". In: *Permafrost and Periglacial Processes* 162, pp. 84–100.

Andrieux, E., P. Bertran, and K. Saito (2016). "Spatial analysis of the French Pleistocene permafrost by a GIS database". In: *Permafrost and Periglacial Processes* 27.1, pp. 17–30. DOI: 10.1002/ppp.1856.

Annan, J. D. and J. C. Hargreaves (2013). "A new global reconstruction of temperature changes at the Last Glacial Maximum". In: *Climate of the Past* 9.1, pp. 367–376. DOI: 10.5194/cp-9-367-2013.

Ballantyne, C. K. (2017). *Periglacial Geomorphology*. Wiley.

Bartlein, P. J. et al. (Aug. 2011). "Pollen-based continental climate reconstructions at 6 and 21 ka: a global synthesis". In: *Climate Dynamics* 37.3, pp. 775–802. DOI: 10.1007/s00382-010-0904-1.

Berger, André L. (Dec. 1978). "Long-Term Variations of Daily Insolation and Quaternary Climatic Changes". In: *Journal of the Atmospheric Sciences* 35.12, pp. 2362–2367.

Bertran, P. et al. (2014). "Distribution and chronology of Pleistocene permafrost features in France: Database and first results". In: *Boreas* 43.3, pp. 699–711. DOI: 10.1111/bor.12025.

Braconnot, P. et al. (Mar. 2012). "Evaluation of climate models using palaeoclimate data". In: *Nature Climate Change* 2, pp. 417–424. DOI: 10.1038/NCLIMATE1456.

Cao, J., B. Wang, and J. Liu (2019). "Attribution of the Last Glacial Maximum climate formation". In: *Climate Dynamics* 53, pp. 1661–1679. DOI: 10.1007/s00382-019-04711-6.

Clark, P. U. et al. (2009). "The Last Glacial Maximum". In: *Science* 325.5941, pp. 710–714. DOI: 10.1126/science.1172873.

Cleator, S. F. et al. (2020). "A new multivariable benchmark for Last Glacial Maximum climate simulations". In: *Climate of the Past* 16, pp. 699–712. DOI: 10.5194/cp-16-699-2020.

Copernicus Climate Change Service (C3S) (2017). *ERA5: Fifth generation of ECMWF atmospheric reanalyses of the global climate*.

Danilov, S., Kivman. G., and J. Schröter (2004). "A finite-element ocean model: principles and evaluation". In: *Ocean Modelling* 6.2, pp. 125–150. DOI: https://doi.org/10.1016/S1463-5003(02)00063-X.

Florineth, D. and C. Schlüchter (2000). "Alpine Evidence for Atmospheric Circulation Patterns in Europe during the Last Glacial Maximum". In: *Quaternary Research* 54.3, pp. 295–308. DOI: 10.1006/qres.2000.2169.

Fortier, D. and M. Allard (2005). "Frost-cracking conditions, Bylot Island, eastern Canadian Arctic archipelago". In: *Permafrost and Periglacial Processes* 16.2, pp. 145–161. DOI: 10.1002/ppp.504.

Frauenfeld, O. W., T. Zhang, and J. L. Mccreight (2007). "Northern Hemisphere freezing/thawing index variations over the twentieth century". In: *International Journal of Climatology* 27.1, pp. 47–63. DOI: 10.1002/joc.1372.

French, H. (2008). "Recent contributions to the study of past permafrost". In: *Permafrost and Periglacial processes* 19.2, pp. 179–194.

French, H. and Y. Shur (2010). "The principles of cryostratigraphy". In: *Earth-Science Reviews* 101.3, pp. 190–206. DOI: https://doi.org/10.1016/j.earscirev.2010.04.002.

Giorgetta, M. A. et al. (2013). "Climate and carbon cycle changes from 1850 to 2100 in MPI-ESM simulations for the Coupled Model Intercomparison Project phase 5". In: *Journal of Advances in Modeling Earth Systems* 5.3, pp. 572–597. DOI: 10.1002/jame.20038.

Harris, C. et al. (2009). "Permafrost and climate in Europe: Monitoring and modelling thermal, geomorphological and geotechnical responses". In: *Earth-Science Reviews* 92.3, pp. 117–171. DOI: https://doi.org/10.1016/j.earscirev.2008.12.002.

Harris, S. A. et al. (2018). "Palsa development and associated vegetation in Northern Sweden". In: *Geocryology: Characteristics and Use of Frozen Ground and Permafrost Landforms*. Vol. 9. 5. National Technical Information Service New York, NY, pp. 1–144.

Harrison, S. P. et al. (2015). "Evaluation of CMIP5 palaeo-simulations to improve climate projections". In: *Nature Climate Change* 5, pp. 735–743. DOI: 10.1038/nclimate2649.

Hong, S.-Y., J. Dudhia, and S.-H. Chen (2004). "A Revised Approach to Ice Microphysical Processes for the Bulk Parameterization of Clouds and Precipitation". In: *Monthly Weather Review* 132.1, pp. 103–120. DOI: 10.1175/1520-0493(2004)132<0103:ARATIM>2.0.CO;2.

Hong, S.-Y., Y. Noh, and J. Dudhia (2006). "A New Vertical Diffusion Package with an Explicit Treatment of Entrainment Processes". In: *Monthly Weather Review* 134.9, pp. 2318–2341. DOI: 10.1175/MWR3199.1.

Hughes, P. D., P. L. Gibbard, and J. Ehlers (2013). "Timing of glaciation during the last glacial cycle: evaluating the concept of a global 'Last Glacial Maximum' (LGM)". In: *Earth-Science Reviews* 125, pp. 171–198. DOI: https://doi.org/10.1016/j.earscirev.2013.07.003.

Huissteden, J. van (2020). *Thawing Permafrost*. Springer. DOI: 10.1007/978-3-030-31379-1.

Iacono, M. J. et al. (2008). "Radiative forcing by long-lived greenhouse gases: Calculations with the AER radiative transfer models". In: *Journal of Geophysical Research: Atmospheres* 113.D13. DOI: 10.1029/2008JD009944.

Ilyina, T. et al. (2013). "Global ocean biogeochemistry model HAMOCC: Model architecture and performance as component of the MPI-Earth system model in different CMIP5 experimental realizations". In: *Journal of Advances in Modeling Earth Systems* 5.2, pp. 287–315. DOI: 10.1029/2012MS000178.

IPCC (2013). *Climate Change 2013: The Physical Science Basis. Contribution of Working Group I to the Fifth Assessment Report of the Intergovernmental Panel on Climate Change*. Stocker, T.F., D. Qin, G.-K. Plattner, M. Tignor, S.K. Allen, J. Boschung, A. Nauels, Y. Xia, V. Bex and P.M. Midgley (eds.). Cambridge University Press, Cambridge, United Kingdom and New York, NY, USA.

– (2019). *IPCC Special Report on the Ocean and Cryosphere in a Changing Climate*. Pörtner, H.-O., Roberts, D.C., Masson-Delmotte, V., Zhai, P., Tignor, M., Poloczanska, E., Mintenbeck, K., Alegría, A., Nicolai, M., Okem, A., Petzold, J., Rama, B. and Weyer, N.M. (eds.). In press.

Isarin, R. F. B., H. Renssen, and J. Vandenberghe (1998). "The impact of the North Atlantic Ocean on the Younger Dryas climate in northwestern and central Europe". In: *Journal of Quaternary Science* 13.5, pp. 447–453. DOI: 10.1002/(SICI)1099-1417(1998090)13:5<447::AID-JQS402>3.0.CO;2-B.

Jiménez, P. A. et al. (2012). "A Revised Scheme for the WRF Surface Layer Formulation". In: *Monthly Weather Review* 140.3, pp. 898–918. DOI: 10.1175/MWR-D-11-00056.1.

Jiraková, H. et al. (2011). "Insights into palaeorecharge conditions for European deep aquifers". In: *Hydrology Journal* 19, pp. 1545–1562.

Jones, P. D., M. Hulme, and K. R. Briffa (1993). "A comparison of Lamb circulation types with an objective classification scheme". In: *International Journal of Climatology* 13.6, pp. 655–663. DOI: 10.1002/joc.3370130606.

Jungclaus, J. H. et al. (2013). "Characteristics of the ocean simulations in the Max Planck Institute Ocean Model (MPIOM) the ocean component of the MPI-Earth system model". In: *Journal of Advances in Modeling Earth Systems* 5.2, pp. 422–446. DOI: 10.1002/jame.20023.

Justino, F. and W. R. Peltier (2005). "The glacial North Atlantic Oscillation". In: *Geophysical Research Letters* 32.21. DOI: 10.1029/2005GL023822.

Justino, F. et al. (2006). "An Initial Intercomparison of Atmospheric and Oceanic Climatology for the ICE-5G and ICE-4G Models of LGM Paleotopography". In: *Journal of Climate* 19.1, pp. 3–14. DOI: 10.1175/JCLI3603.1.

Kageyama, M. et al. (2020). "The PMIP4-CMIP6 Last Glacial Maximum experiments: preliminary results and comparison with the PMIP3-CMIP5 simulations". In: *Climate of the Past Discussions* 2020, pp. 1–37. DOI: 10.5194/cp-2019-169. in review.

Kain, J. S. (2004). "The Kain–Fritsch Convective Parameterization: An Update". In: *Journal of Applied Meteorology* 43.1, pp. 170–181. DOI: 10.1175/1520-0450(2004)043<0170:TKCPAU>2.0.CO;2.

Kitover, D. C. et al. (2013). "New Estimates of Permafrost Evolution during the Last 21 k Years in Eurasia using Numerical Modelling". In: *Permafrost and Periglacial Processes* 24.4, pp. 286–303. DOI: 10.1002/ppp.1787.

Kitover, D. C. et al. (2016). "LGM Permafrost Thickness and Extent in the Northern Hemisphere derived from the Earth System Model iLOVECLIM". In: *Permafrost and Periglacial Processes* 27.1, pp. 31–42. DOI: 10.1002/ppp.1861.

Kohfeld, K. E. and S. P. Harrison (2000). "How well can we simulate past climates? Evaluating the models using global palaeoenvironmental datasets". In: *Quaternary Science Reviews* 19.1, pp. 321–346. DOI: https://doi.org/10.1016/S0277-3791(99)00068-2.

Kokelj, S. V. et al. (2014). "Distribution and activity of ice wedges across the forest-tundra transition, western Arctic Canada". In: *Journal of Geophysical Research: Earth Surface* 119.9, pp. 2032–2047. DOI: 10.1002/2014JF003085.

Kukla, G. J. et al. (2002). "Last Interglacial Climates". In: *Quaternary Research* 58.1, pp. 2–13. DOI: https://doi.org/10.1006/qres.2001.2316.

Lachenbruch, A. H. (1962). *Mechanics of the thermal contraction cracks and ice-wedge polygons in permafrost*. Geological Society of America Special Paper 70.

Laîné, A. et al. (2009). “Northern hemisphere storm tracks during the last glacial maximum in the PMIP2 ocean-atmosphere coupled models: energetic study, seasonal cycle, precipitation”. In: *Climate Dynamics* 32, pp. 593–614. DOI: 10.1007/s00382-008-0391-9.

Lambeck, K. and J. Chappell (2001). “Sea Level Change Through the Last Glacial Cycle”. In: *Science* 292.5517, pp. 679–686. DOI: 10.1126/science.1059549.

Lambeck, K., Y. Yokoyama, and T. Purcell (2002). “Into and out of the Last Glacial Maximum: sea-level change during Oxygen Isotope Stages 3 and 2”. In: *Quaternary Science Reviews* 21.1. EPILOG, pp. 343–360. DOI: https://doi.org/10.1016/S0277-3791(01)00071-3.

Lehmkuhl, F. et al. (2016). “Loess-paleosol sequences at the northern European loess belt in Germany: Distribution, geomorphology and stratigraphy”. In: *Quaternary Science Reviews* 153, pp. 11–30. DOI: https://doi.org/10.1016/j.quascirev.2016.10.008.

Levavasseur, G. et al. (2011). “Present and LGM permafrost from climate simulations : contribution of statistical downscaling”. English. In: *Climate of the Past* 7.4, pp. 1225–1246. DOI: 10.5194/cp-7-1225-2011.

Li, C. and D. S. Battisti (2008). “Reduced Atlantic Storminess during Last Glacial Maximum: Evidence from a Coupled Climate Model”. In: *Journal of Climate* 21.14, pp. 3561–3579. DOI: 10.1175/2007JCLI2166.1.

Liu, Y. and D. Jiang (2016a). “Last glacial maximum permafrost in China from CMIP5 simulations”. English. In: *Palaeogeography, Palaeoclimatology, Palaeoecology* 447.C, pp. 12–21. DOI: 10.1016/j.palaeo.2016.01.042.

– (2016b). “Mid-Holocene permafrost: Results from CMIP5 simulations”. In: *Journal of Geophysical Research: Atmospheres* 121.1, pp. 221–240. DOI: 10.1002/2015JD023837.

Löfverström, M. et al. (2014). “Evolution of the large-scale atmospheric circulation in response to changing ice sheets over the last glacial cycle”. In: *Climate of the Past* 10.4, pp. 1453–1471. DOI: 10.5194/cp-10-1453-2014.

Löfverström, M. et al. (2016). “Stationary Wave Reflection as a Mechanism for Zonalizing the Atlantic Winter Jet at the LGM”. In: *Journal of the Atmospheric Sciences* 73.8, pp. 3329–3342. DOI: 10.1175/JAS-D-15-0295.1.

Ludwig, P. et al. (2016). “Regional atmospheric circulation over Europe during the Last Glacial Maximum and its links to precipitation”. In: *Journal of Geophysical Research: Atmospheres* 121.5, pp. 2130–2145. DOI: 10.1002/2015JD024444.

Ludwig, P. et al. (2017). “Impacts of surface boundary conditions on regional climate model simulations of European climate during the Last Glacial Maximum”. In: *Geophysical Research Letters* 44.10, pp. 5086–5095. DOI: 10.1002/2017GL073622.

Ludwig, P. et al. (2019). “Perspectives of regional paleoclimate modeling”. In: *Annals of the New York Academy of Sciences* 1436.1, pp. 54–69. DOI: 10.1111/nyas.13865.

MARGO Project Members (2009). “Constraints on the magnitude and patterns of ocean cooling at the Last Glacial Maximum”. In: *Nature Geoscience* 2, pp. 127–132. DOI: doi:10.1038/ngeo411.

Marsland, S. J. et al. (2003). “The Max-Planck-Institute global ocean/sea ice model with orthogonal curvilinear coordinates”. In: *Ocean Modelling* 5.2, pp. 91–127. DOI: https://doi.org/10.1016/S1463-5003(02)00015-X.

Matsuoka, N., H. H. Christiansen, and T. Watanabe (2018). "Ice-wedge polygon dynamics in Svalbard: Lessons from a decade of automated multi-sensor monitoring". In: *Permafrost and Periglacial Processes* 29.3, pp. 210–227. DOI: 10.1002/ppp.1985.

Merz, N., C. C. Raible, and T. Woollings (2015). "North Atlantic Eddy-Driven Jet in Interglacial and Glacial Winter Climates". In: *Journal of Climate* 28.10, pp. 3977–3997. DOI: 10.1175/JCLI-D-14-00525.1.

Mix, A. C., E. Bard, and R. Schneider (2001). "Environmental processes of the ice age: land, oceans, glaciers (EPILOG)". In: *Quaternary Science Reviews* 20.4, pp. 627–657. DOI: https://doi.org/10.1016/S0277-3791(00)00145-1.

Monnin, E. et al. (2001). "Atmospheric CO2 Concentrations over the Last Glacial Termination". In: *Science* 291.5501, pp. 112–114. DOI: 10.1126/science.291.5501.112.

Murton, J. B. (2007). "Ice wedges and ice wedge casts". In: *Encyclopedia of Quaternary Science*. Ed. by S. A. Elias. Vol. 2. Elsevier, Amsterdam, pp. 2153–2170.

Murton, J. B. and E. Kolstrup (2003). "Ice-wedge casts as indicators of palaeotemperatures: precise proxy or wishful thinking?" In: *Progress in Physical Geography: Earth and Environment* 27.2, pp. 155–170. DOI: 10.1191/0309133303pp365ra.

Nelson, F. E. and S. I. Outcalt (1987). "A Computational Method for Prediction and Regionalization of Permafrost". In: *Arctic and Alpine Research* 19.3, pp. 279–288. DOI: 10.1080/00040851.1987.12002602.

Osterkamp, T. E. and C. R. Burn (2003). "Permafrost". In: *Encyclopedia of Atmospheric Sciences*. Ed. by R. R. Holton, J. Pyle, and J. A. Curry. Academic Press, pp. 1717–1729.

Pausata, F. S. R. et al. (Oct. 2011). "The key role of topography in altering North Atlantic atmospheric circulation during the last glacial period". In: *Climate of the Past* 7. DOI: 10.5194/cp-7-1089-2011.

Peltier, W. R., D. F. Argus, and R. Drummond (2015). "Space geodesy constrains ice age terminal deglaciation: The global ICE-6G_C (VM5a) model". In: *Journal of Geophysical Research: Solid Earth* 120.1, pp. 450–487. DOI: 10.1002/2014JB011176.

Pfahl, S., P. A. O'Gorman, and M. S. Singh (Dec. 2015). "Extratropical Cyclones in Idealized Simulations of Changed Climates". In: *Journal of Climate* 28.23, pp. 9373–9392. DOI: 10.1175/JCLI-D-14-00816.1.

Pinto, J. G. and P. Ludwig (2020). "Extratropical cyclones over the North Atlantic and western Europe during the Last Glacial Maximum and implications for proxy interpretation". In: *Climate of the Past* 16.2, pp. 611–626. DOI: 10.5194/cp-16-611-2020.

Pongratz, J. et al. (2008). "A reconstruction of global agricultural areas and land cover for the last millennium". In: *Global Biogeochemical Cycles* 22.3. DOI: 10.1029/2007GB003153.

Prentice, I. C. and S. P. Harrison (2009). "Ecosystem effects of CO_2 concentration: evidence from past climates". In: *Climate of the Past* 5.3, pp. 297–307. DOI: 10.5194/cp-5-297-2009.

Prospero, J. M. et al. (2002). "Environmental characterization of global sources of atmoshperic soil dust identified with the NIMBUS 7 total ozone mapping spectrometer (TOMS) absorbing aerosol product". In: *Reviews of Geophysics* 40.1. DOI: 10.1029/2000RG000095.

Rackow, T. et al. (2018). "Towards multi-resolution global climate modeling with ECHAM6-FESOM. Part II: climate variability". In: *Climate Dynamics* 50, pp. 2369–2394. DOI: 10.1007/s00382-016-3192-6.

Raible, C. C. et al. (2020). “A review of past changes in extratropical cyclones in the northern hemisphere and what can be learned for the future”. In: *WIREs Climate Change*. DOI: 10.1002/wcc.680.

Ray, N. and Jonathan M. Adams (2001). “A GIS-based vegetation map of the world at the Last Glacial Maximum (25,000-15,000 BP)”. In: *Internet Archaeology* 11.

Reick, C. H. et al. (2013). “Representation of natural and anthropogenic land cover change in MPI-ESM”. In: *Journal of Advances in Modeling Earth Systems* 5.3, pp. 459–482. DOI: 10.1002/jame.20022.

Renssen, H. and J. Vandenberghe (2003). “Investigation of the relationship between permafrost distribution in NW Europe and extensive winter sea-ice cover in the North Atlantic Ocean during the cold phases of the Last Glaciation”. In: *Quaternary Science Reviews* 22.2, pp. 209–223. DOI: https://doi.org/10.1016/S0277-3791(02)00190-7.

Saito, K. et al. (2013). “LGM permafrost distribution: how well can the latest PMIP multi-model ensembles perform reconstruction?” In: *Climate of the Past* 9.4, pp. 1697–1714. DOI: 10.5194/cp-9-1697-2013.

Schaffernicht, E. J., P. Ludwig, and Y. Shao (2020). “Linkage between dust cycle and loess of the Last Glacial Maximum in Europe”. In: *Atmospheric Chemistry and Physics* 20.8, pp. 4969–4986. DOI: 10.5194/acp-20-4969-2020.

Schuur, E. A. G. et al. (2015). “Climate change and the permafrost carbon feedback”. In: *Nature* 520, pp. 171–179. DOI: 10.1038/nature14338.

Screen, J. and I. Simmonds (2010). “The central role of diminishing sea ice in recent Arctic temperature amplification”. In: *Nature* 464, pp. 1334–1337. DOI: 10.1038/nature09051.

Semmler, T. et al. (2020). “Simulations for CMIP6 with the AWI climate model AWI-CM-1-1”. In: *Earth and Space Science Open Archive*, p. 48. DOI: 10.1002/essoar.10501538.1.

Sidorenko, D. et al. (2015). “Towards multi-resolution global climate modeling with ECHAM6–FESOM. Part I: model formulation and mean climate”. In: *Climate Dynamics* 44, pp. 757–780. DOI: 10.1007/s00382-014-2290-6.

Skamarock, W.C. et al. (2008). “A description of the advanced research WRF version 3”. In: *NCAR Tech. Note NCAR/TN-475+STR* 113. DOI: 10.5065/D68S4MVH.

Slater, A. G. and D. M. Lawrence (2013). “Diagnosing Present and Future Permafrost from Climate Models”. In: *Journal of Climate* 26.15, pp. 5608–5623. DOI: 10.1175/JCLI-D-12-00341.1.

Stendel, M. and J. H. Christensen (2002). “Impact of global warming on permafrost conditions in a coupled GCM”. In: *Geophysical Research Letters* 29.13. DOI: 10.1029/2001GL014345.

Stevens, B. et al. (2013). “Atmospheric component of the MPI-M Earth System Model: ECHAM6”. In: *Journal of Advances in Modeling Earth Systems* 5.2, pp. 146–172. DOI: 10.1002/jame.20015.

Stevens, T. et al. (2020). “Abrupt last glacial dust fall over southeast England associated with dynamics of the British-Irish ice sheet”. In: *Quaternary Science Reviews* 250, p. 106641. DOI: https://doi.org/10.1016/j.quascirev.2020.106641.

Tarasov, L. and R. W. Peltier (July 2002). “Greenland glacial history and local geodynamic consequences”. In: *Geophysical Journal International* 150.1, pp. 198–229. DOI: 10.1046/j.1365-246X.2002.01702.x.

Tarasov, L. and W. Peltier R. (2003). “Greenland glacial history, borehole constraints, and Eemian extent”. In: *Journal of Geophysical Research: Solid Earth* 108.B3. DOI: 10.1029/2001JB001731.

Taylor, K. E., R. J. Stouffer, and G. A. Meehl (2012). “An Overview of CMIP5 and the Experiment Design”. In: *Bulletin of the American Meteorological Society* 93.4, pp. 485–498. DOI: 10.1175/BAMS-D-11-00094.1.

Tewari, M. et al. (2004). “Implementation and verification of the unified NOAH land surface model in the WRF model”. In: *20th conference on weather analysis and forecasting/16th conference on numerical weather prediction*, pp. 11–15.

Ullman, D. J. et al. (2014). “Assessing the impact of Laurentide Ice Sheet topography on glacial climate”. In: *Climate of the Past* 10.2, pp. 487–507. DOI: 10.5194/cp-10-487-2014.

UNEP (2019). *Frontiers 2018/19 Emerging Issues of Environmental Concern*. United Nations Environment Programme, Nairobi.

Valcke, S. (2013). “The OASIS3 coupler: a European climate modelling community software”. In: *Geoscientific Model Development* 6.2, pp. 373–388. DOI: 10.5194/gmd-6-373-2013.

van Everdingen, R. O. (2005). *Multi-language glossary of permafrost and related ground-ice terms*.

Vandenberghe, J. et al. (2012). “Eurasian permafrost instability constrained by reduced sea-ice cover”. In: *Quaternary Science Reviews* 34, pp. 16–23. DOI: https://doi.org/10.1016/j.quascirev.2011.12.001.

Vandenberghe, J. et al. (2014). “The Last Permafrost Maximum (LPM) map of the Northern Hemisphere: permafrost extent and mean annual air temperatures, 25–17 ka BP”. In: *Boreas* 43.3, pp. 652–666. DOI: 10.1111/bor.12070.

Wang, N., D. Jiang, and X. Lang (2018). “Northern Westerlies during the Last Glacial Maximum: Results from CMIP5 Simulations”. In: *Journal of Climate* 31.3, pp. 1135–1153. DOI: 10.1175/JCLI-D-17-0314.1.

Wang, Q. et al. (2014). “The Finite Element Sea Ice-Ocean Model (FESOM) v.1.4: formulation of an ocean general circulation model”. In: *Geoscientific Model Development* 7.2, pp. 663–693. DOI: 10.5194/gmd-7-663-2014.

Wang, Tao, Yi Liu, and Wei Huang (2013). “Last Glacial Maximum Sea Surface Temperatures: A Model-Data Comparison”. In: *Atmospheric and Oceanic Science Letters* 6.5, pp. 233–239. DOI: 10.3878/j.issn.1674-2834.13.0019.

Washburn, A. L. (1963). “Frost cracking in a middle latitude climate”. In: *Biul. Peryglac.* 12, pp. 175–189.

Watanabe, T., N. Matsuoka, and H. H. Christiansen (2013). “Ice- and Soil-Wedge Dynamics in the Kapp Linné Area, Svalbard, Investigated by Two- and Three-Dimensional GPR and Ground Thermal and Acceleration Regimes”. In: *Permafrost and Periglacial Processes* 24.1, pp. 39–55. DOI: 10.1002/ppp.1767.

Wolfe, S. A. et al. (2018). “Contemporary sand wedge development in seasonally frozen ground and paleoenvironmental implications”. In: *Geomorphology* 308, pp. 215–229. DOI: https://doi.org/10.1016/j.geomorph.2018.02.015.

Danksagung

An dieser Stelle möchte ich mich bei all jenen bedanken, die mich während meines Studiums und insbesondere während der Zeit der Masterarbeit unterstützt haben.

Zunächst danke ich meinem Referenten Prof. Dr. Joaquim Pinto für die Betreuung meiner Masterarbeit. Die regelmäßigen Diskussionen, ob persönlich oder online, haben mich immer weitergebracht und mir sehr geholfen.

Für die unkomplizierte Übernahme des Koreferats danke ich Dr. Aiko Voigt. Sein konstruktives Feedback hat mir neue Perspektiven der Interpretation meiner Ergebnisse aufgezeigt.

Dr. Patrick Ludwig möchte ich herzlich für die Begleitung durch meine Masterarbeit danken. Durch seine geduldige Einführung in die Regionalklimamodellierung und in die Paleoklimatologie habe ich Themen gefunden, mit denen ich mich auch in Zukunft gerne weiter beschäftigen möchte. Für meine Fragen hat sich Patrick immer auch kurzfristig Zeit genommen und mir gleichzeitig Raum gegeben, eigene Ansätze auszuprobieren.

Meinen Freunden und meiner Familie bin ich dankbar, dass sie mir den Rücken freigehalten und mich auf vielfältige Weise unterstützt haben. Dabei denke ich an hilfreiche Diskussionen und technische Hilfe genauso wie an Päckchen und Postkarten und die Ablenkung von der Masterarbeit bei Telefonaten und Spaziergängen.

Danke!

Erklärung

Ich versichere wahrheitsgemäß, die Arbeit selbständig angefertigt, alle benutzten Hilfsmittel vollständig und genau angegeben und alles kenntlich gemacht zu haben, was aus Arbeiten anderer unverändert oder mit Abänderungen entnommen wurde.

Karlsruhe, den 10.11.2020

Kim Helen Albers